ERDC TR-22-11

US Army Corps of Engineers®
Engineer Research and Development Center

ERDC
ENGINEER RESEARCH & DEVELOPMENT CENTER

Extreme Terrain Research

Simulating Environmental Conditions for Southwest United States Convective Dust Storms Using the Weather Research and Forecasting Model v4.1

Alex R. Gallagher, Sandra L. LeGrand, Taylor S. Hodgdon, and Theodore W. Letcher

August 2022

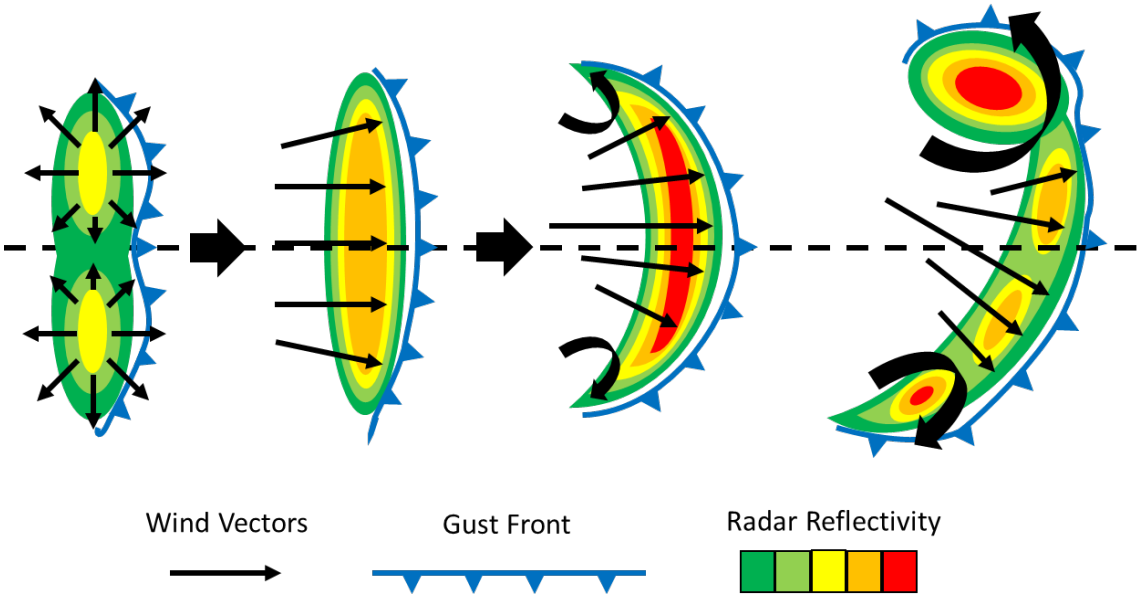

Engineer Research and Development Center

Approved for public release; distribution is unlimited.

The U.S. Army Engineer Research and Development Center (ERDC) solves the nation's toughest engineering and environmental challenges. ERDC develops innovative solutions in civil and military engineering, geospatial sciences, water resources, and environmental sciences for the Army, the Department of Defense, civilian agencies, and our nation's public good. Find out more at www.erdc.usace.army.mil.

To search for other technical reports published by ERDC, visit the ERDC online library at https://erdclibrary.on.worldcat.org/discovery.

ERDC TR-22-11
August 2022

Simulating Environmental Conditions for Southwest United States Convective Dust Storms Using the Weather Research and Forecasting Model v4.1

Alex R. Gallagher, Taylor S. Hodgdon, and Theodore W. Letcher

US Army Engineer Research and Development Center (ERDC)
Cold Regions Research and Engineering Laboratory (CRREL)
72 Lyme Road
Hanover, NH 03755-1290

Sandra L. LeGrand

US Army Engineer Research and Development Center (ERDC)
Geospatial Research Laboratory (GRL)
7701 Telegraph Road
Alexandria, VA 22315-3864

Final Report

Approved for public release; distribution is unlimited.

Prepared for Headquarters, US Army Corps of Engineers
Washington, DC 20314-1000

Under PE 0603734A, Project T15, Extreme Terrain Research, "Forecasting EO/IR Extinction Characteristics for Active and Passive Optical Systems"

Abstract

Dust aerosols can pose a significant detriment to public health, transportation, and tactical operations through reductions in air quality and visibility. Thus, accurate model forecasts of dust emission and transport are essential to decision makers. While a large number of studies have advanced the understanding and predictability of dust storms, the majority of existing literature considers dust production and forcing conditions of the underlying meteorology independently of each other. Our study works towards filling this research gap by inventorying dust-event case studies forced by convective activity in the Desert Southwest United States, simulating select representative case studies using several configurations of the Weather Research and Forecasting (WRF) model, testing the sensitivity of forecasts to essential model parameters, and assessing overall forecast skill using variables essential to dust production and transport.

We found our control configuration captured the initiation, evolution, and storm structure of a variety of convective features admirably well. Peak wind speeds were well represented, but we found that simulated events arrived up to 2 hours earlier or later than observed. Our results show that convective storms are highly sensitive to initialization time and initial conditions that can preemptively dry the atmosphere and suppress the growth of convective storms.

DISCLAIMER: The contents of this report are not to be used for advertising, publication, or promotional purposes. Citation of trade names does not constitute an official endorsement or approval of the use of such commercial products. All product names and trademarks cited are the property of their respective owners. The findings of this report are not to be construed as an official Department of the Army position unless so designated by other authorized documents.

DESTROY THIS REPORT WHEN NO LONGER NEEDED. DO NOT RETURN IT TO THE ORIGINATOR.

Contents

Abstract ii

Figures and Tables v

Preface x

1 Introduction 1

1.1 Background 1
1.2 Objectives 2
1.3 Approach 2

2 Methodology 3

2.1 Supporting datasets 4
2.1.1 Storm Prediction Center Hourly Mesoscale Analysis (SPCHMA) 4
2.1.2 Next Generation Weather Radar (NEXRAD) 5
2.1.3 Automated Surface Observing Stations (ASOS) 6
2.1.4 Remote Automatic Weather Stations (RAWS) 7
2.2 Model configuration 8
2.2.1 Model resolution 10
2.2.2 Initialization and lateral boundary datasets (model forcing data) 11
2.2.3 Planetary-boundary-layer schemes 12
2.2.4 Surface-layer schemes 14
2.2.5 Land surface models 14
2.2.6 Cumulus schemes 15
2.2.7 Cloud microphysics schemes 16
2.2.8 Initialization time (model spin-up) 17
2.3 Model assessment 19
2.4 Case studies 21

3 Results 24

3.1 4 July 2014 case study 25
3.1.1 4 July 2014 event overview 25
3.1.2 4 July 2014 simulation results 28
3.1.3 Model sensitivity analysis 36
3.2 21 August 2014 case study 45
3.2.1 21 August 2014 event overview 45
3.2.2 21 August 2014 simulation results 48
3.3 28 June 2015 case study 58
3.3.1 28 June 2015 event overview 58
3.3.2 28 June 2015 simulation results 61
3.4 1–2 August 2017 case study 69
3.4.1 1–2 August 2017 event overview 69
3.4.2 1–2 August 2017 simulation results 75
3.5 30 July 2018 case study 85

3.5.1 30 July 2018 event overview *85*
3.5.2 30 July 2018 simulation results *88*

4 Discussion **98**

5 Conclusions and Recommendations **102**
5.1 General conclusions 102
5.2 Recommendations 103

References **105**

Appendix A : SPC Storm Report Database Search Algorithm **109**

Appendix B : Full Inventory of Case Studies **116**

Acronyms and Abbreviations **118**

Report Documentation Page **120**

Figures and Tables

Figures

1. Locations of all available ASOS (Automated Surface Observation System; *red squares*) and RAWS (Remote Access Weather Stations; *blue circles*) surface weather stations within the domain of the Desert Southwest United States (DSWUS) that report data during one or all of the selected case studies. 8

2. The three nested domains used by the Weather Research and Forecasting (WRF) model overlaid: map base layer and WRF topography (*color fill*). 9

3. NEXRAD (Next Generation Weather Radar) composite radar reflectivity images at the peak time during each of the five case studies selected: (*A*) 0000 UTC, 4 July 2014; (*B*) 2200 UTC, 21 August 2014; (*C*) 0000 UTC, 28 June 2015; (*D*) 0000 UTC, 1–2 August 2017; and (*E*) 0030 UTC, 30 July 2018. 22

4. Important physiographic features referenced throughout case study analyses. The bottom image is a zoomed-in representation of the area outlined by the *solid red line* in the *top* image. 24

5. SPCHMA (Storm Prediction Center Hourly Mesoscale Analysis) 500 hPa height (*contoured*) and wind (*barbs* and *shaded*) (*panels A* and *B*) and 850 hPa height (*contoured*), wind (*barbs*), and dew point (*shaded*) (*panels C* and *D*) valid at 1200 UTC, 3 July 2014 (*A, C*), and 0000 UTC, 4 July 2014 (*B*, *D*). 26

6. NEXRAD radar composite imagery for the 4 July 2014 case for 1800 UTC, 3 July 2014 (*A*); 2000 UTC, 3 July 2014 (*B*); 2200 UTC, 3 July 2014 (*C*); 0000 UTC, 4 July 2014 (*D*); 0200 UTC, 4 July 2014 (*E*); 0400 UTC, 4 July 2014 (*F*); and 0600 UTC, 4 July 2014 (*G*). 27

7. SPCHMA (*panels A* and *B*) and WRF CTRL d01 forecast (*panels C* and *D*) of 500 hPa height (*contoured*) and wind (*barbs* and *shaded*) valid at 1200 UTC, 3 July 2014 (*A*, *C*), and 0000 UTC, 4 July 2014 (*B*, *D*). 29

8. SPCHMA (*panels A* and *B*) and WRF CTRL d01 forecast (*panels C* and *D*) of 850 hPa height (*contoured black*), wind (*barbs*), and dew point (*shaded*, Celsius) valid at 1200 UTC, 3 July 2014 (*A*, *C*), and 0000 UTC, 4 July 2014 (*B, D*). 30

9. SPCHMA (*panels A* and *B*) and WRF CTRL d02 forecast (*panels C* and *D*) of column-integrated precipitable water (under 400 hPa, *shaded* and *contoured* in inches) valid at 1200 UTC, 3 July 2014 (*A*, *C*), and 0000 UTC, 4 July 2014 (*B*, *D*). Contours are every 0.1 in. 31

10. Observed NEXRAD radar (*panels A–F*) and WRF CTRL d03 simulated 1 km AGL (above ground level) radar (*panels a–f*) for 2000 UTC, 3 July 2014 (*A*, *a*); 2200 UTC, 3 July 2014 (*B*, *b*); 0000 UTC, 4 July 2014 (*C*, *c*); 0200 UTC, 4 July 2014 (*D*, *d*); 0400 UTC, 4 July 2014 (*E*, *e*); and 0600 UTC, 4 July 2014 (*F*, *f*). 32

11. Time series of observed (*black*) and modeled (*red*) surface (10 m) wind speed during the 3 July 2014 dust storm for the network average of all ASOS stations (*A*), KSAD (*B*), KPHX (*C*), KSDL (*D*), and KDVT (*E*). The *gray line* in the network average shows the number of stations used in the network average. The 1 min observations are supplemented by METARs

(Meteorological Aerodrome Reports) at individual stations when needed and are denoted by *dots*. 34

12. Similar to Fig. 11 except for the average of all RAWS stations (*A*), GRAA3 (*B*), BLMA3 (*C*), QHBA3 (*D*), and QSPA3 (*E*) surface (6.1 m) wind speed. *Dots* are used for individual stations since data are reported only once every hour with no specific reporting time. 35

13. Observed NEXRAD radar composite (*J*) and WRF d03 simulated 1 km AGL radar from various WRF configurations at 0000 UTC, 4 July 2014 (peak of the 4 July 2014 event): CTRL configuration (*A*), WSM6 (*B*), NoahMP (*C*), MYJ (*D*), YSU (*E*), 12hrInit (*F*), 3km (*G*), VertRes (*H*), and GFS (*I*). 38

14. Observed and forecasted wind speed from all WRF simulations for ASOS (*A*) and RAWS (*B*) network averages and stations nearest the epicenter of the event, KPHX from ASOS (*C*) and GRAA3 from RAWS (*D*). Additionally, model-forecasted average wind speed mean absolute error (MAE) and bias (*E*) with ASOS verification in the *dots* and RAWS in *diamonds*. 39

15. WRF d03 topography (*shaded*) and RAWS station locations, color coded by the average forecast wind speed bias at each station from the CTRL simulation during the 4 July 2014 dust event (*A*). Average bias of the CTRL forecast vs. the difference between the model elevation and actual observation elevation (model minus observed) for each RAWS station (*B*). Histogram of RAWS station land-use index, 1 = Evergreen Needleleaf Forest, 5 = Mixed Forests, 6 = Closed Shrubland, 7 = Open Shrubland, 10 = Grasslands, and 13 = Urban/Built Up (*C*). 42

16. Time series of observations (*black*), base forecasts (*red*), and surface-roughness-adjusted forecasts (*purple*) of surface wind speed (6.1 m) averaged over the RAWS network. The surface-roughness adjustment uses a static z_0 = 0.5 m for stations with an elevation above 2000 m. 43

17. Histograms of the prescribed surface roughness at RAWS stations by the Noah (*blue bars*) and NoahMP (*red bars*) LSMs at the initialization time (*A*) and 2 hr into the forecast (*B*), binned every 0.1 m. *Purple* shaded areas indicate overlap between the two LSMs. 44

18. SPCHMA of 500 hPa height (*contoured*) and wind (*barbs* and *shaded*) valid at 1200 UTC, 21 August 2014 (*A*); 2100 UTC, 21 August 2014 (*B*); and 0300 UTC, 22 August 2014 (*C*). 46

19. SPCHMA of 850 hPa height (*contoured black*), wind (*barbs*), and dew point (*shaded*, Celsius) valid at 1200 UTC, 21 August 2014 (*A*); 1800 UTC, 21 August 2014 (*B*); 0000 UTC, 22 August 2014 (*C*); and 0600 UTC, 22 August 2014 (*D*). 47

20. NEXRAD radar composite imagery for the 21 August 2014 case for 1600 UTC, 21 August 2014 (*A*); 1800 UTC, 21 August 2014 (*B*); 2000 UTC, 21 August 2014 (*C*); 2200 UTC, 21 August 2014 (*D*); 0000 UTC, 22 August 2014 (*E*); 0200 UTC, 22 August 2014 (*F*); and 0400 UTC, 22 August 2014 (*G*). 48

21. SPCHMA (*panels A–C*) and WRF CTRL d01 forecasts (*panels D–F*) of 500 hPa height (*contoured*) and wind (*barbs* and *shaded*) valid at 1200 UTC, 21 August 2014 (*A*, *D*); 2100 UTC, 21 August 2014 (*B*, *E*); and 0300 UTC, 22 August 2014 (*C*, *F*). 50

22. SPCHMA (*panels A–C*) and WRF CTRL d01 forecasts (*panels D–F*) of 850 hPa height (*contoured black*), wind (*barbs*), and dew point (*shaded*, Celsius) valid at 1200 UTC, 21 August 2014 (*A*, *D*); 1800 UTC, 21 August

2014 (*B*, *E*); and 0000 UTC, 22 August 2014 (*C*, *F*). 51

23. SPCHMA (*panels A–C*) and WRF CTRL d02 forecasts (*panels B–F*) of column-integrated precipitable water (under 400 hPa, *shaded* and *contoured* in inches) valid at 1200 UTC, 21 August 2014 (*A*, *D*); 1800 UTC, 21 August 2014 (*B*, *E*); and 0000 UTC, 22 August 2014 (*C*, *F*). Contours are every 0.1 in. 52

24. Observed NEXRAD radar (*panels A–F*) and WRF CTRL d03 simulated 1 km AGL radar (*panels a–f*) for 1600 UTC, 21 August 2014 (*A*, *a*); 1800 UTC, 21 August 2014 (*B*, *b*); 2000 UTC, 21 August 2014 (*C*, *c*); 2200 UTC, 21 August 2014 (*D* and *d*); 0000 UTC, 22 August 2014 (*E* and *e*); and 0200 UTC, 22 August 2014 (*F* and *f*). 54

25. Time series of observed (*black*) and modeled (*red*) surface (10 m) wind speed during the 21 August 2014 dust storm for the network average of all ASOS stations (*A*), KEED (*B*), KBLH (*C*), KNYL (*D*), and KIPL (*E*). The *gray line* in the network average shows the number of stations used in the network average. The 1 min observations are supplemented by METARS at individual stations when needed and are denoted by *dots*. 56

26. Similar to Fig. 25 except for the average of all RAWS stations (*A*), QUPA3 (*B*), AKPA3 (*C*), CBRA3 (*D*), QCAC3 (*E*) surface (6.1 m) wind speed. *Dots* are used for individual stations since data is reported only once every hour with no specific reporting time. 58

27. SPCHMA of 500 hPa height (*contoured*) and wind (*barbs* and *shaded*) (*panels A* and *B*) and 850 hPa height (*contoured*), wind (*barbs*), and dew point (*shaded*) (*panels C* and *D*) valid at 1200 UTC, 27 June 2015 (*A*, *C*), and 0000 UTC, 28 June 2015 (*B*, *D*). 59

28. NEXRAD radar composite imagery for the 28 June 2015 case for 1800 UTC, 27 June 2015 (*A*); 2000 UTC, 27 June 2015 (*B*); 2200 UTC, 27 June 2015 (*C*); 0000 UTC, 28 June 2015 (*D*); 0200 UTC, 28 June 2015 (*E*); 0400 UTC, 28 June 2015 (*F*); and 0600 UTC, 28 June 2015 (*G*). 61

29. SPCHMA (*panels A* and *B*) and WRF CTRL d01 forecast (*panels C* and *D*) of 500 hPa height (*contoured*) and wind (*barbs* and *shaded*) valid at 1200 UTC, 27 June 2015 (*A*, *C*), and 0000 UTC, 28 June 2015 (*B*, *D*). 62

30. SPCHMA (*panels A* and *B*) and WRF CTRL d01 forecasts (*panels* C and D) of 850 hPa height (*contoured black*), wind (*barbs*), and dew point (*shaded*, Celsius) valid at 1200 UTC, 27 June 2015 (*A*, *C*), and 0000 UTC, 28 June 2015 (*B*, *D*). 63

31. SPCHMA (*panels A* and *B*) and WRF CTRL d02 forecasts (*panels C* and *D*) of column-integrated precipitable water (under 400 hPa, *shaded* and *contoured* in inches) valid at 1200 UTC, 27 June 2015 (*A*, *C*), and 0000 UTC, 28 June 2015 (*B*, *D*). Contours are every 0.1 in. 64

32. Observed NEXRAD radar (*panels A–F*) and WRF CTRL d03 simulated 1 km AGL radar (*panels a–f*) for 2000 UTC, 27 June 2015 (*A*, *a*); 2200 UTC, 27 June 2015 (*B*, *b*); 0000 UTC, 28 June 2015 (*C*, *c*); 0200 UTC, 28 June 2015 (*D*, *d*); 0400 UTC, 28 June 2015 (*E*, *e*); and 0600 UTC, 28 June 2015 *(F*, *f*). 66

33. Time series of observed (*black*) and modeled (*red*) surface (10 m) wind speed during the 28 June 2015 dust storm for network average of all ASOS stations (*A*), KSAD (*B*), KPHX (*C*), KSDL (*D*), and KDVT (*E*). The *gray line* in the network average shows the number of stations used in the network average. The 1 min observations are supplemented by METARS

at individual stations when needed and are denoted by *dots*. 68

34. Time series of observed (*black*) and modeled (*red*) surface (10 m) wind speed during the 28 June 2015 dust storm for network average of all RAWS stations (*A*), QGLA3 (*B*), QSLA3 (*C*), GRAA3 (*D*), and BLMA3 (*E*) surface (6.1 m) wind speed. *Dots* are used for individual stations since data is reported only once every hour with no specific reporting time. 69

35. SPCHPA of 500 hPa height (*contoured*) and wind (*barbs* and *shaded*) valid at 0000 UTC, 31 July 2017 (*A*); 1200 UTC, 31 July 2017 (*B*); 0000 UTC, 1 August 2017 (*C*); 1200 UTC, 1 August 2017 (*D*); 0000 UTC, 2 August 2017 (*E*); 1200 UTC, 2 August 2017 (*F*); and 0000 UTC, 3 August 2017 (*G*)..... 70

36. SPCHMA of 850 hPa height (*contoured black*), wind (*barbs*), and dew point (*shaded*, Celsius) valid at 0000 UTC, 31 July 2017 (*A*); 0600 UTC, 31 July 2017 (*B*); 0000 UTC, 1 August 2017 (*C*); 0000 UTC, 2 August 2017 (*D*); 1500 UTC, 2 August 2017 (*E*); 2100 UTC, 2 August 2017 (*F*); and 0000 UTC, 3 August 2017 (*G*). 73

37. NEXRAD radar composite imagery for the 1–2 August 2017 case for 0200 UTC, 31 July 2017 (*A*); 0430 UTC, 31 July 2017 (*B*); and 0700 UTC, 31 July 2017 (*C*); 2100 UTC, 31 July 2017 (*D*); 0000 UTC, 1 August 2017 (*E*); 0300 UTC, 1 August 2017 (*F*); 0600 UTC, 1 August 2017 (*G*); 2200 UTC, 1 August 2017 (*H*); 0000 UTC, 2 August 2017 (*I*); 0200 UTC, 2 August 2017 (*J*); and 0400 UTC, 2 August 2017 (*K*); and 2000 UTC, 2 August 2017 (*L*); 0000 UTC, 3 August 2017 (*M*); 0130 UTC, 3 August 2017 (*N*); and 0300 UTC, 3 August 2017 (*O*)..... 74

38. SPCHMA (*panels A–F*) and WRF CTRL d01 forecasts (*panels a–f*) of 500 hPa height (*contoured*) and wind (*barbs* and *shaded*) valid at 1200 UTC, 31 July 2017 (*A*, *a*); 0000 UTC, 1 August 2017 (*B*, *b*); 1200 UTC, 1 August 2017 (*C*, *c*); 0000 UTC, 2 August 2017 (*D*, *d*); 1200 UTC, 2 August 2017 (*E*, *e*); and 0000 UTC, 3 August 2017 (*F*, *f*). 76

39. SPCHMA (*panels A–F*) and WRF CTRL d01 forecasts (*panels a–f*) of 850 hPa height (*contoured black*), wind (*barbs*), and dew point (*shaded*, Celsius) valid at 0600 UTC, 31 July 2017 (*A*, *a*); 0000 UTC, 1 August 2017 (*B*, *b*); 0000 UTC, 2 August 2017 (*C*, *c*); 1500 UTC, 2 August 2017 (*D*, *d*); 2100 UTC, 2 August 2017 (*E*, *e*); and 0000 UTC, 3 August 2017 (*F*, *f*)..... 78

40. SPCHMA (*panels A–F*) and WRF CTRL d02 forecasts (*panels a–f*) of column-integrated precipitable water (under 400 hPa, *shaded* and *contoured* in inches) valid at 0600 UTC, 31 July 2017 (*A*, *a*); 1800 UTC, 31 July 2017 (*B*, *b*); 0600 UTC, 1 August 2017 (*C*, *c*); 1800 UTC, 1 August 2017 (*D*, *d*); 0600 UTC, 2 August 2017 (*E*, *e*); and 1800 UTC, 2 August 2017 (*F* and *f*). Contours are every 0.1 in. 79

41. Observed NEXRAD radar (*panels A–G*) and WRF CTRL d03 simulated 1 km AGL radar (*panels a–g*) for 0700 UTC, 31 July 2017 (*A*, *a*); 0000 UTC, 1 August 2017 (*B*, *b*); 0200 UTC, 1 August 2017 (*C*, *c*); 0000 UTC, 2 August 2017 (*D*, *d*); 0300 UTC, 2 August 2017 (*E*, *e)*; and 0000 UTC, 3 August 2017 (*F*, *f*); and 0300 UTC, 3 August 2017 (*G*, *g*)..... 80

42. Time series of observed (*black*) and modeled (*red*) surface (10 m) wind speed during the 1–2 August 2017 dust storm for the network average of all ASOS stations (*A*), KGCN (*B*), KFLG (*C*), KIGM (*D*), and KEED (*E*). The *gray line* in the network average shows the number of stations used in the network average. The 1 min observations are supplemented by METARS at individual stations when needed and are denoted by *dots*. 82

43. Similar to Fig. 42 except for the average of all RAWS stations (*A*), QGBA3 (*B*), QGDA3 (*C*), GMBA3 (*D*), and QHAA3 (*E*) surface (6.1 m) wind speed. *Dots* are used for individual stations since data is reported only once every hour with no specific reporting time. 84

44. SPCHMA of 500 hPa height (*contoured*) and wind (*barbs* and *shaded*) (*panels A* and *B*) and 850 hPa height (*contoured*), wind (*barbs*), and dew point (*shaded*) (*panels C* and *D*) valid at 1200 UTC, 29 July 2018 (*A*, *C*), and 0000 UTC, 30 July 2018 (*B*, *D*). 86

45. NEXRAD radar composite imagery for the 30 July 2018 case for 1900 UTC, 29 July 2018 (*A*); 2100 UTC, 29 July 2018 (*B*); 2300 UTC, 29 July 2018 (*C*); 0030 UTC, 30 July 2018 (*D*); 0200 UTC, 30 July 2018 (*E*); and 0400 UTC, 30 July 2018 (*F*). 87

46. SPCHMA (*panels A* and *B*) and WRF CTRL d01 forecasts (*panels C* and *D*) of 500 hPa height (*contoured*) and wind (*barbs* and *shaded*) valid at 1200 UTC, 29 July 2018 (*A*, *C*), and 0000 UTC, 30 June 2018 (*B*, *D*). 89

47. SPCHMA (*panels A* and *B*) and WRF CTRL d01 forecasts (*panels C* and *D*) of 850 hPa height (*contoured black*), wind (*barbs*), and dew point (*shaded*, Celsius) valid at 1200 UTC, 29 July 2018 (*A*, *C*), and 0000 UTC, 30 July 2018 (*B*, *D*). 90

48. SPCHMA (*panels A* and *B*) and WRF CTRL d02 forecasts (*panels C* and *D*) of column-integrated precipitable water (under 400 hPa, *shaded* and *contoured* in inches) valid at 1200 UTC, 29 July 2018 (*A*, *C*), and 0000 UTC, 30 July 2018 (*B*, *D*). Contours are every 0.1 in. 91

49. Observed NEXRAD radar (*panels A–F*) and WRF CTRL d03 simulated 1 km AGL radar (*panels a–f*) at 1900 UTC, 29 July 2018 (*A*, *a*); 2100 UTC, 29 July 2018 (*B*, *b*); 2300 UTC, 29 July 2018 (*C*, *c*); 0030 UTC, 30 July 2018 (*D*, *d*); 0200 UTC, 30 July 2018 (*E*, *e*); and 0400 UTC, 30 July 2018 (*F*, *f*) 93

50. Time series of observed (*black*) and modeled (*red*) surface (10 m) wind speed during the 30 July 2018 dust storm for network average of all ASOS stations (*A*), KSAD (*B*), KTUS (*C*), KPHX (*D*), and KDVT (*E*). The *gray line* in the network average shows the number of stations used in the network average. The 1 min observations are supplemented by METARS at individual stations when needed and are denoted by *dots*. 95

51. Similar to Fig. 50 except for the average of all RAWS stations (*A*), QHBA3 (*B*), QHRA3 (*C*), GSCA3 (*D*), and QGLA3 (*E*) surface (6.1 m) wind speed. *Dots* are used for individual stations since data is reported only once every hour with no specific reporting time. 96

Tables

1. Details on measurements of surface wind speed and direction from the ASOS and RAWS networks 7

2. List of variables and options critical to the WRF configuration and justification for their selection. 18

Preface

This study was conducted for Headquarters, US Army Corps of Engineers, under PE 0603734A, Project T15, Extreme Terrain Research, "Forecasting EO/IR Extinction Characteristics for Active and Passive Optical Systems."

The work was performed by the Terrestrial and Cryospheric Sciences Branch of the Research and Engineering Division, US Army Engineer Research and Development Center, Cold Regions Research and Engineering Laboratory (ERDC-CRREL). At the time of publication, Dr. John Weatherly was branch chief, and Dr. Caitlin A. Callaghan was division chief. The acting deputy director of ERDC-CRREL was Mr. Bryan E. Baker, and the director was Dr. Joseph L. Corriveau.

Additional work was performed by the Information Generation and Management Branch of the Geospatial Research Division, ERDC Geospatial Research Laboratory (GRL). At the time of publication, Mr. Michael F. Mailloux was branch chief, and Mr. Jeffrey B. Murphy was division chief. The acting director was Ms. Valerie L. Carney.

The authors acknowledge Ms. Samantha Cook for her assistance generating figures.

COL Christian Patterson was commander of ERDC, and Dr. David W. Pittman was the director.

1 Introduction

1.1 Background

Dust aerosols have the potential to create hazardous air quality conditions that can negatively affect public health; agriculture; transportation; and in particular, aviation (e.g., Middleton 2017; Al-Hemoud et al. 2017; Middleton, Tozer, and Tozer 2019; AlKheder and AlKandari 2020). Reductions in visibility from lofted dust present not only a danger to the public but also an advantage to leverage or a hindrance to manage on a battlefield (e.g., Lyles 2018; Department of the Army 1993, 2019, 2020). Therefore, accurate model forecasts of dust emissions and transport are critical to weather forecasters, military personnel, and emergency managers. The Weather Research and Forecasting (WRF) model with chemistry (WRF-Chem) is a publicly available model used by multiple agencies (including DoD), air quality and energy managers, and aerosol researchers. However, the dust transport models built into the WRF-Chem framework are tuned primarily to produce accurate representations of aerosol radiative effects and concentrations on global spatial and climate temporal scales. Ultimately, this can lead to misleading or unreliable forecasts of visibility and dust concentration for public and military applications in arid and semiarid environments.

An underlying methodology flaw common to many published dust-modeling studies is the lack of a comprehensive evaluation assessing a given forecasting system's ability to simulate the overall meteorological forcing conditions driving the dust events. Researchers tend to focus on how well models characterize aggregate measures of dust transport, such as airborne particulate matter concentrations or aerosol optical depths. When forcing conditions are considered, analyses often focus on individual weather parameters that are known to affect dust transport (e.g., surface-wind time series or precipitation patterns). However, holistic assessments of atmospheric forcing conditions are necessary to ensure skillful simulation of dust-storm structure and evolution, especially if the study aims to evaluate model sensitivity to various algorithms or datasets. Otherwise, effectively discerning whether simulation outcomes (good or bad) are actually due to a specific dust-model aspect or are an artifact of erroneous forcing conditions is difficult at best.

1.2 Objectives

The goal of this study was to assess the ability of the WRF model (i.e., the parent model to WRF-Chem) to simulate a series of convective storms that resulted in dust transport in the Desert Southwest United States (DSWUS). Our motivation for this effort was to establish an inventory of accurately simulated atmospheric forcing conditions to support future research activities aimed at addressing the dust transport model components of WRF-Chem. Creating a baseline of reliable case studies provides a dependable starting point for testing new dust-modeling approaches and reduces the likelihood of atmospheric field errors propagating into the dust simulation results.

Our objectives were as follows:

1. To identify an inventory of convective dust-event case studies to simulate with WRF
2. To establish a control WRF-model configuration that we expected to have reasonable skill in simulating convective dust storms in the DSWUS
3. To test the sensitivity of the case study simulations to alternate physics and other configuration changes (e.g., model grid resolution, initialization datasets, etc.)
4. To validate model output against relevant observations concerning synoptic, surface, and atmospheric boundary-layer conditions
5. To identify the model configuration with the most skill, both overall and for individual cases, to use as a baseline for testing dust-modeling capabilities in future studies

1.3 Approach

This report is organized as follows: section 2, "Methodology," discusses the approach we used to address each of the objectives, specifically our selection process for model configuration and the data, methods, and metrics used for qualitative and quantitative verifications. In section 3, "Results," we present the results of our holistic verification, including case study overviews, validation of model forecasts, and analysis of sensitivity testing. In section 4, "Discussion," we assess our findings comprehensively, determining if and how they address each of our objectives. Lastly, section 5, "Conclusions and Recommendations," summarizes the overall findings of our study and highlights key aspects of our methodology and results. Additionally, we propose opportunities for further study to resolve potential sources of uncertainty in our findings and address new questions uncovered by our work.

2 Methodology

We approached our primary goal of assessing the ability of the WRF model to simulate DSWUS convective dust storms by using a three-part methodology. Our first step was to identify numerous eligible case studies. Using a variety of dust-event case studies allowed us to analyze various convective modes and forcing conditions to assess model performance, which increases confidence in the model's ability to produce skillful forecasts. We started our search using case study events from relevant previously published literature and by searching the Storm Prediction Center's (SPC) severe storm report archive. Once we identified our initial list of potential options, we selected for simulation our final case study event inventory based on the convective mode, geographical location, societal impact, and availability of observational data for verification of each event.

Next, we selected physics parameterizations and other essential model settings for our experimental WRF-model control (CTRL) configuration based on a modified version of the High Resolution Rapid Refresh (HRRR) operational model initially described by Benjamin et al. (2016). We also performed a sensitivity analysis to explore the effects of variations in model physics and configuration on simulated forecast accuracy. Using this CTRL configuration, we conducted qualitative and quantitative assessments of simulation results for each of the selected case studies. Ultimately, we considered a simulated forecast successful if it accurately reproduced the overall synoptic conditions, regional-scale flow patterns, and resulting fine-scale convection that drove the dust event.

Synoptic conditions, typically characterized by the flow pattern of the upper atmosphere, play a key role in the development and progression of weather systems through the positioning of ridges, troughs, and strong winds. Validating these large-scale features was particularly important for our assessment since misrepresentation of the synoptic pattern can markedly change the intensity of the simulated large-scale forcing and drastically alter the resulting convective-scale weather. Moisture and regional wind-pattern assessment in the lower atmosphere were also essential to our methodology as these parameters are critical for convective storm formation, maintenance, and propagation.

For our qualitative verification evaluations, we compared model forecasts to the NOAA Next Generation Weather Radar (NEXRAD) composites (National Weather Service 1991) and the SPC's Hourly Mesoscale Analysis (SPCHMA; Bothwell, Hart, and Thompson 2002). Comparison of NEXRAD composite imagery to model-simulated radar reflectivity enabled us to assess the development, location, intensity, and mode of convective systems. Convective mode, in particular, is critical as storm types can differ widely in spatial pattern, maintenance and intensification mechanisms, and induced surface wind patterns. Conversely, the SPCHMA comparison guided our evaluation of the larger-scale upper-air and synoptic conditions, as well as lower atmospheric and regional patterns.

Weather forcing at the interface between the atmosphere and the land surface is especially important in the dust-lofting process, motivating more quantitative analysis of surface observations. Specifically, we examined simulated surface wind speed and direction time series against archived Automated Surface Observation System (ASOS) and Remote Access Weather Stations (RAWS) observations. We also explored the reasons for any discrepancies in performance metrics between the various data sources.

The remainder of this section further expands on the methodology and datasets we employed in our analysis. In section 2.1, we provide an overview of the datasets used to verify model forecasts. Section 2.2 further elaborates on the details of the CTRL configuration and the alternative configurations used for our sensitivity analysis, while section 2.3 describes our verification methods and the metrics used to determine forecast skill. Lastly, section 2.4 details how we built the inventory of case studies and the criteria we used to select cases for simulation.

Of note, we explored alternate model-configuration settings for only the first case study. Results from the sensitivity test supported further use of our CTRL configuration for the rest of our analyses. WRF simulations referenced in the remainder of the document all used the CTRL model settings unless otherwise specified.

2.1 Supporting datasets

2.1.1 Storm Prediction Center Hourly Mesoscale Analysis (SPCHMA)

The SPC produces the final hourly mesoscale analysis by running three-dimensional meteorological fields from the most recent Rapid Refresh

Model (RAP; Benjamin et al. 2016) initialization period (commonly referred to in numerical modeling as the model analysis) through an objective analysis scheme called surface observation analysis (Bothwell, Hart, and Thompson 2002). For this method, the SPC assimilates surface and upper-air radiosonde observations into the RAP analysis; applies rigorous data quality control and objective analyses; and, if needed, incorporates adjustments by trained forecasters. The final product is an hourly 13 km resolution analysis of standard and severe storm atmospheric fields over the conterminous US (CONUS).

We utilized 500 hPa* (i.e., a 500-hectopascal atmospheric pressure level) SPCHMA data to assess our simulated upper atmosphere and synoptic-scale conditions and 850 hPa SPCHMA data for qualitative validation of our lower-atmospheric and regional moisture patterns. The 850 hPa fields, in particular, represent conditions near the land surface for our area of interest rather well due to the relatively high terrain elevation, strong diurnal heating, and summer season low pressures common in the DSWUS. Use of this product helped us to identify regional steering flows, as well as low-level moisture sources and "hotspots."

Hourly SPCHMA data are available for 18 October 2005 through the present (SPC 2022a). Although SPCHMA products are high-quality datasets, it is essential to remember that the data initially derive from numerical model simulations and serve as a "best guess." Therefore, we used SPCHMA as only a general guide to benefit from its incorporation of available observations and insight from seasoned severe-weather forecasters.

2.1.2 Next Generation Weather Radar (NEXRAD)

We analyzed observed NEXRAD composite imagery (National Weather Service 1991) collected by NOAA and stored by the National Centers for Environmental Information (NCEI; NCEI, "NEXRAD," n.d.) to qualitatively compare and verify the location, structure, and severity of the WRF-simulated convective storms. The radar composite images comprise a blend of radar reflectivity from individual locations with overlapping coverage to generate a cohesive radar map across the CONUS. This mosaic approach has the advantage of filling in blockages from individual radar

* For a full list of the spelled-out forms of the units of measure used in this document, please refer to *U.S. Government Publishing Office Style Manual*, 31st ed. (Washington, DC: U.S Government Publishing Office, 2016), 248–252, https://www.govinfo.gov/content/pkg/GPO-STYLEMANUAL-2016/pdf/GPO-STYLEMANUAL-2016.pdf.

sites with neighboring ones, providing a more complete snapshot of convective activity across the coverage area. Radar reflectivity is reported and assessed in terms of decibels relative to Z (dBZ), a logarithmic equivalent to traditional reflectivity (Z) measured in sextic millimeters per cubic meter (mm^6/m^3).

2.1.3 Automated Surface Observing Stations (ASOS)

The ASOS network is a widely used set of surface observations, often considered the standard for surface measurements in the atmospheric community. This esteem derives from ASOS's adherence to World Meteorological Organization (WMO) standards and their relatively long observational record (most sensors began reporting in the 1990s). Additionally, most ASOS station locations are at airports with large unobstructed fetches. In our area of study, 68 ASOS stations report temperature, humidity, pressure, precipitation, wind speed and direction, and current weather conditions (see Figure 1).

We focused our surface weather analysis on wind speed and direction because of the importance of wind for dust entrainment and its role as an indicator of convective strength and mode. ASOS observations are available in the standard Meteorological Aerodrome Report (METAR) format (e.g., WMO 2018) every hour and in the less conventional 1 min format reported every minute. We utilized 1 min frequency ASOS observation data archived by NCEI (available online through standard file transfer protocol at ftp://ftp.ncdc.noaa.gov/pub/data/asos-onemin/). When the 1 min data were missing or unavailable, we retrieved hourly ASOS METAR data from the NOAA National Centers for Environmental Prediction (NCEP) Meteorological Assimilation Data Ingest System (MADIS; National Weather Service 2018) for verification.

ASOS nominally reports "surface" wind at the WMO standard height of 10 m; however, 16 of the stations in our domain report wind observations collected at nonstandard heights of 7.9 m or 5.8 m. Because the diagnostic surface wind output by the WRF model defaults to 10 m above ground level (AGL; $U_{10\mathrm{m}}$), we performed an additional height adjustment to the simulated wind speeds when verifying winds at these locations. Following the log-wind profile method described by Tennekes (1973), we modified our simulated surface winds by

$$U_h = U_{10\text{m}} \left[\frac{\ln(h/z_0)}{\ln(10/z_0)} \right], \quad (1)$$

where h is the reporting height of the observed wind (U_h) and z_0 is the aerodynamic surface roughness of the model grid cell.

2.1.4 Remote Automatic Weather Stations (RAWS)

Because of the relatively small number of ASOS stations within the area of study and their geographic confinement, we also leveraged additional surface observations from the RAWS network. The RAWS network is run by the US Forest Service and Bureau of Land Management, primarily to monitor potential wildfire conditions. Unlike ASOS, RAWS sites are in remote locations, often in complex and rugged terrain. As such, they do not fully conform to WMO standards owing to space and power restrictions of their locations. Despite this drawback, RAWS data are frequently the only available observations in geographic areas with exceptionally variable or high-elevation topography.

RAWS stations report hourly surface temperature, humidity, pressure, precipitation, and wind speed and direction observations. However, there is no consistent reporting time between stations, unlike ASOS sites, which report at the top of every hour. The two networks also differ in how they measure wind. RAWS sites monitor wind speed using cup anemometers and direction vanes, whereas ASOS sites predominantly measure both attributes with sonic anemometers. Table 1 summarizes the key aspects and differences between the two surface networks.

Table 1. Details on measurements of surface wind speed and direction from the ASOS and RAWS networks.

Surface Wind Network	Anemometer Type	Mounting Height	Comments
ASOS	Sonic	10 m	Reported as a 2 min average every minute in raw format or an hourly average in METAR format (within 10 min of the top of the hour) reported once per hour.
RAWS	Cup and vane	6.1 m	Reported as a 10 min average hourly at nonstandard times (typically at the top of the hour or half hour).

There are 323 RAWS stations within our study area, many located along mountainous slopes or isolated peaks (Figure 1). We retrieved archived RAWS data for our analysis through the same MADIS portal that we used

to procure the ASOS data. Because RAWS stations nominally report surface winds at 6.1 m AGL, we adjusted the associated WRF-simulated wind speed data using equation (1) before conducting our validation effort.

Figure 1. Locations of all available ASOS (Automated Surface Observation System; *red squares*) and RAWS (Remote Access Weather Stations; *blue circles*) surface weather stations within the domain of the Desert Southwest United States (DSWUS) that report data during one or all of the selected case studies.

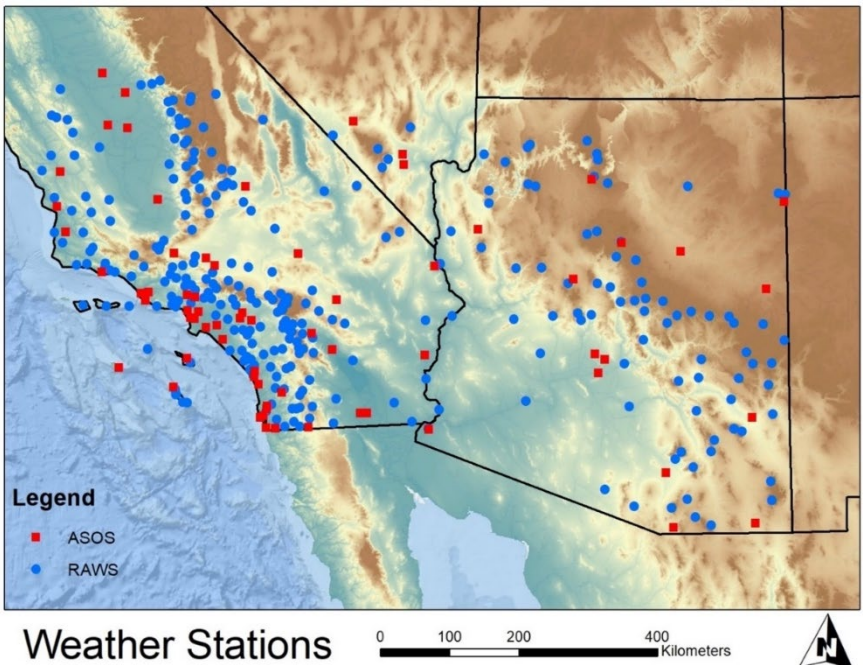

2.2 Model configuration

WRF is an Earth-system modeling framework with several configuration options for atmosphere and land surface processes (Skamarock et al. 2019). For our analysis, we specifically chose to use WRF version 4.1 (NCAR 2019) because this particular release aligned with important error corrections made to some of the more widely used WRF-Chem dust transport modules. To effectively represent DSWUS convective storm conditions, our model configuration must accurately simulate the structure and evolution of complex convective systems, in particular, their surface meteorological effects. We based our CTRL model settings on the configuration used for the HRRR forecast product (an operational WRF-based convection-allowing atmospheric model run by NCEP) and WRF configuration options for downslope wind-pattern simulation explored in studies by Cao and Fovell (e.g., Cao and Fovell 2016, 2018; Fovell and Cao 2017).

While downslope windstorms tend to be dry phenomena (i.e., lacking associated precipitation), their level of surface complexity, required model resolution, and interaction with land surface features are similar to those of convective storms. Lastly, we chose certain parameters based on our previous modeling experience and logistical constraints. Table 2 (on page 18) outlines a full list of model details and justifications for our configuration selections. Also, we thoroughly describe the influence that model parameters could have on the resulting output and further explain our choices for both the CTRL and alternately configured setups in sections 2.2.1–2.2.8.

Figure 2 shows the bounds of our nested model domains telescoping over the DSWUS. The position and size of the outermost domain (d01) and intermediate domain (d02) remained fixed throughout the experiment. Though our innermost domain (d03) size also stayed consistent, we shifted its position between case studies based on the general location of each event.

Figure 2. The three nested domains used by the Weather Research and Forecasting (WRF) model overlaid: map base layer and WRF topography (*color fill*).

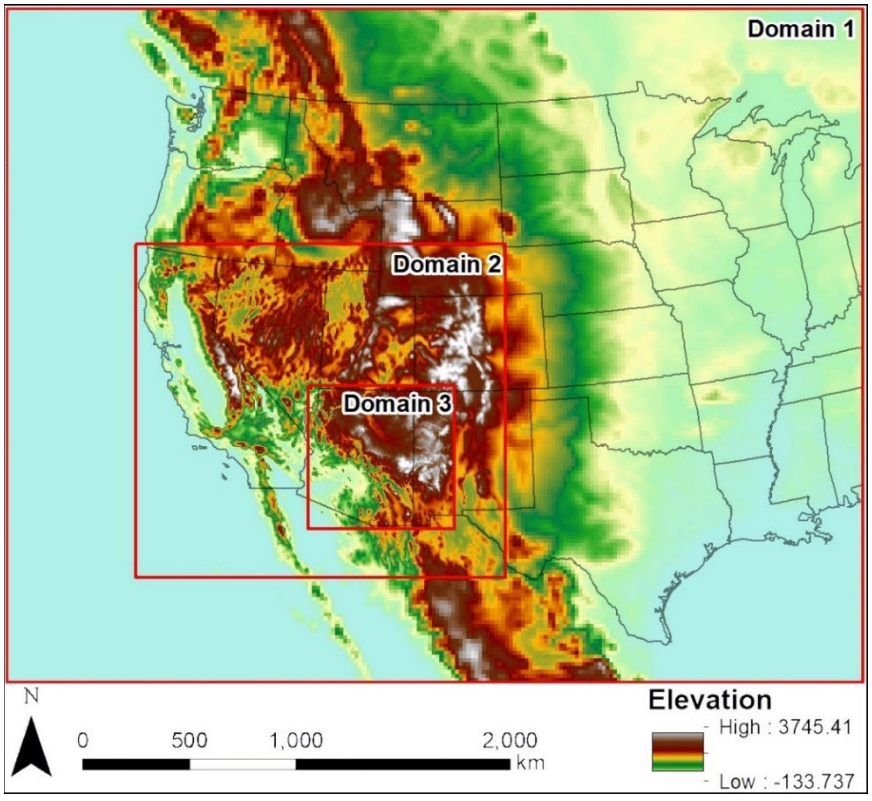

2.2.1 Model resolution

Numerical weather models are often sensitive to model grid resolution, especially when simulating weather phenomena governed by increasingly small-scale features or processes heavily influenced by interactions between the land surface and the atmosphere. A common practice in numerical weather prediction is to use a horizontal grid resolution four times smaller than the smallest-scale phenomenon of interest. Following this approach ensures at least four grid cells represent the small-scale features applicable to the model use case, properly captures any wave-like (or oscillating) patterns, and filters out most artifacts generated from undersampling in the initialization or boundary forcing data. In our selected case studies, the scales of convection ranged from hundreds of kilometers (the width of some mature convective systems, mesoscale beta [20–200 km]) down to about 10 km (width of convective cores and resulting downdrafts, mesoscale gamma [2–20 km]).

Convectively forced dust storms inherently depend on surface conditions since sediment-transport interactions at the land-atmosphere interface drive the dust emission process. Accurate representation of dust production in models can strongly depend on how well the model characterizes surface aspects with potentially high spatial variability over short distances, such as vegetation coverage, soil moisture, aerodynamic surface roughness, and soil composition. Our area of interest, the DSWUS, includes complex large- and small-scale topographic features that markedly influence surface wind patterns (both speed and direction) and convective storm tracks. As a result, we required relatively fine-scale horizontal grid resolution to prevent the WRF preprocessor from artificially smoothing and misrepresenting (or potentially eliminating) important topographic features like steep slopes, valleys, and isolated peaks.

The WRF model uses a telescoping nested domain structure that passes information from larger, lower-resolution parent domains down to smaller, finer-resolution child domains. Our study used three domains, zooming in over the DSWUS, that adopted the developer-recommended parent/child resolution ration of 3:1. Based on the aforementioned four-times-scaling theory, the innermost domain should have a grid spacing of approximately 2.5 km to adequately resolve a convective feature on the order of 10 km (i.e., if 10 km $\approx 4\Delta x$ and Δx is the length of each domain grid square, then $\Delta x \approx 2.5$ km). Therefore, we considered two grid-resolution configurations for our study. Our CTRL configuration used resolutions of

18 km, 6 km, and 2 km for d01, d02, and d03, respectively; and we explored an alternative configuration using grid resolutions of 27 km, 9 km, and 3 km for d01, d02, and d03, respectively.

Additionally, WRF requires sufficient vertical resolution to simulate the intense upward and downward vertical motions associated with convective thunderstorms. The best practices guide for WRF suggests adding at least enough vertical levels so that the vertical spacing between any two levels is less than 1 km (Dudhia and Wang 2014). This practice dictates the use of more vertical levels when processes at incredibly high altitudes (i.e., low pressures), such as stratospheric interactions, are essential to the simulated event because WRF places most of the vertical levels closer to the land surface by default. We elected to use 42 vertical levels (default is 28 vertical levels) with default vertical spacing distribution associated with the WRF v4.1 source code download for our CTRL configuration. We confirmed this spacing adheres to the 1 km or less spacing threshold in the community standards and places 10 vertical levels within 1 km above ground level. However, given the potential sensitivity of simulated convective updrafts and downdrafts to vertical resolution, we also tested an alternative configuration with 65 vertical levels.

2.2.2 Initialization and lateral boundary datasets (model forcing data)

The WRF model requires gridded forcing data, both meteorological and terrestrial, to initialize from and to force its evolution to model the environmental state throughout the forecast period. These "forcing" datasets provide the WRF model with an initial weather pattern to evolve from, the atmospheric state outside of the outermost domain, and the atmospheric conditions moving in and out of the outermost domain (commonly referred to as lateral boundary conditions). We chose to use model analysis fields (i.e., simulation output associated with a model's initialization period) rather than simulated forecasts as forcing data for our simulations. This approach enabled us to leverage the observations assimilated into the forcing model during its spin-up but reduced the likelihood of forecast errors propagating into our simulations as the forcing model evolved from its initial state.

Specifically, we selected model analysis data produced by the operational RAP (Benjamin et al. 2016) to set the initial and lateral boundary conditions for our simulations, primarily because RAP analysis fields also serve as forcing data for the operational HRRR model discussed previously. The

RAP analysis product incorporates real-time surface and upper-air observations from commercial aircraft, balloon data, radar data, surface observations, and satellite data. Archived hourly analysis data are available with 13 km horizontal grid resolution over the CONUS from 1 May 2012 through the present. However, RAP analysis datasets do not contain any soil moisture information, a necessary input to WRF. As such, we supplemented our RAP analysis data with soil moisture fields from the operational North American Model (NAM) analysis product. This product is similar in concept to the RAP analysis; however, the NAM system incorporates a different observation data assimilation scheme and produces analysis fields only four times a day at 0000, 0600, 1200, and 1800 UTC. Archived NAM analysis data with 12 km grid resolution are available for most of North America from 3 March 2004 through the present. Because of the temporal limitations associated with the NAM analysis product, we used the RAP analysis fields from only 0000, 0600, 1200, and 1800 UTC in combination with the NAM analysis soil moisture data to force our WRF simulations.

To test the sensitivity of our forecasts to initial conditions, we also assessed an alternative WRF-model configuration using analysis fields from the operational Global Forecasting System (GFS) as initial and boundary conditions. Similar to the NAM system, GFS analysis fields are produced only four times daily at 0000, 0600, 1200, and 1800 UTC. Unlike RAP and NAM, which are regional models, GFS is a global spectral model with 0.5° grid resolution (approximately 43 km at 38° N latitude near our study area). Archived GFS analysis fields are available from 1 January 2007 through the present. All three of these model analysis datasets are accessible through the NCEI data portal at https://www.ncei.noaa.gov/products/weather-climate-models (NCEI, "Weather and Climate Models," n.d.).

2.2.3 Planetary-boundary-layer schemes

The planetary boundary layer (PBL) is the layer of the atmosphere that directly interacts with the Earth's surface and ranges in depth from meters to several kilometers. Surface radiative effects and aerodynamic drag drive atmospheric behavior within the PBL through turbulent eddies that vary in scale depending on PBL depth and stability. These eddies are responsible for the distribution of heat, moisture, and momentum throughout the PBL and are often on scales that cannot be directly resolved by regional

weather models (including WRF). Instead, regional models rely on turbulence parameterizations embedded in PBL schemes to estimate the net effect of eddies on the atmospheric column.

The primary purpose of PBL-scheme turbulence parameterizations is to estimate tendencies (i.e., time derivatives) of prognostic variables (e.g., wind vector components, moisture, temperature, and other advected elements) due to unresolved turbulent motions. Algorithms designed to represent turbulence always incorporate unknown quantities because they are not closed-form expressions. In other words, the parameterizations comprise a finite number of equations to resolve turbulence then approximate the remaining unknowns. A common practice is to refer to turbulence parameterizations as being a *higher*- or *lower*-order closure based on the number of components they explicitly resolve.

There are two main groupings of PBL schemes differentiated by how they estimate the turbulent kinetic energy (TKE) of eddies: local (prognostic) and nonlocal (diagnostic). In local schemes, equations estimate unknown TKE components using other known parameters associated with the same location in the atmosphere. Conversely, nonlocal schemes diagnose the unknown quantity using known values from multiple locations. Local schemes available for use in WRF, like Mellor-Yamada-Janjić (MYJ) (Janjić 1994) and Mellor-Yamada-Nakanishi-Niino (MYNN) (Nakanishi and Niino 2004), directly predict TKE on model levels, while nonlocal schemes, like Yonsei University (YSU; Hong, Noh, and Dudhia 2006), estimate the depth of the PBL and impose an empirical TKE profile. Because they explicitly calculate interactions between vertical model levels, local schemes are able to resolve smaller-scale eddies but often fail to simulate larger, more vigorous eddies; Conversely, nonlocal schemes better predict deep mixing but can overmix and smooth PBL profiles occasionally.

We selected the local MYNN PBL scheme for our CTRL configuration because it calculates turbulence more explicitly than some of the other local PBL schemes available in WRF (i.e., it is a higher-order closure scheme). MYNN is also less likely to overmix deep, radiatively driven PBLs common to the DSWUS and includes algorithms for capturing deep, large-scale mixing with equations designed to work with local-scheme architecture (Weisman et al. 2008). Additionally, we tested two alternative WRF configurations to analyze the sensitivity of our simulations to our PBL-scheme choice. One configuration used the MYJ PBL scheme, which uses a lower-

order closure approach than MYNN. We also tested the nonlocal YSU PBL scheme, which is widely used by the research community.

2.2.4 Surface-layer schemes

The surface layer (SL) is the layer of the atmosphere in immediate contact with the ground and typically encompasses the lowest 100 m. Aerodynamic drag and surface radiative effects are much stronger in the SL than in the rest of the PBL, justifying a separate model parameterization. The SL scheme also acts as a bridge and buffer between the land surface and PBL, passing relevant information from one to the other. Most SL schemes are developed jointly with a specific PBL scheme, so particular pairings are often preferred by end-users while many others are incompatible.

The MYNN PBL-scheme developers also created a matching MYNN SL scheme as a part of a holistic physics package. As such, we used the MYNN SL scheme for our CTRL configuration. The MYJ PBL scheme is also compatible with the MYNN SL scheme due to MYJ's shared lineage with the MYNN PBL code. Accordingly, we used the MYNN SL in our alternate MYJ PBL configuration. Our CTRL SL-scheme selection, however, is not suitable for use with our alternate YSU PBL-scheme configuration, as YSU is a different class of PBL scheme (nonlocal). As such, we used the Revised Mesoscale Model 5 (MM5) (Fairall et al. 2003) SL scheme, which is based on traditional similarity theory and compatible with the majority of available PBL schemes in WRF, for our YSU PBL configuration.

2.2.5 Land surface models

WRF represents the actual land surface through use of a land surface model (LSM). The LSM takes in atmospheric information; calculates surface fluxes, soil state, vegetative and snowpack effects, and surface roughness; and passes these parameters back to the PBL and SL schemes. While LSMs do not explicitly need to pair with specific PBL or SL schemes, some combinations are not possible.

We selected the Noah LSM (Chen and Dudhia 2001; Ek et al. 2003), a commonly used LSM compatible with most PBL and SL schemes, for our CTRL configuration. We also tested a more advanced LSM adapted from the Noah LSM, called Noah Multiparameterization (NoahMP; Niu et al. 2011), in an alternative configuration. NoahMP operates similarly to the

original Noah LSM but has more advanced physics for canopy interactions, snowpack evolution, surface runoff, and water storage.

2.2.6 Cumulus schemes

Depending on their resolution configuration and the convective mode of the simulated event, models may not be able to explicitly resolve convective cloud-related processes adequately. In these instances, numerical weather models use cumulus (CU) schemes to parameterize the influence that subgrid convective cloud processes have on the atmospheric column. These schemes primarily capture convective heat sources and moisture sinks as simulated water vapor condenses into clouds and precipitates, warming and drying the atmosphere.

The numerous CU schemes available within WRF differ in their triggering mechanism or threshold for convection, as well as their ability to parameterize shallow convection (i.e., cloud tops below 3000 m AGL). Though considerable debate remains on what circumstances warrant the use of a CU scheme, an unofficial guidance is to incorporate a CU scheme if the horizontal grid resolution exceeds 4 km (i.e., above the typical scale on which convective processes occur). As such, we activated a CU parameterization for d01 and d02 but disabled it inside d03 as the domain's grid size was below 4 km in all of our configurations.

We specifically selected our model resolution so that our innermost domain (d03) could explicitly resolve convective clouds on its own. The other two domains (d01 and d02) used the New Simplified Arakawa-Schubert (NewSAS) CU scheme (Han and Pan 2011), a relatively simplistic yet flexible treatment of convection. This CU scheme configuration choice mainly stemmed from our previous experience using NewSAS and several of the other CU schemes available in WRF to simulate convective weather events in an ensemble mode (i.e., using multiple model configurations to indicate a range of possible future states). Because our convective analysis focused on simulation results from d03, in which the CU scheme is turned off due to the domain's sufficiently high resolution, we chose to not conduct any additional CU sensitivity tests for this effort.

2.2.7 Cloud microphysics schemes

While numerical weather models may be able to resolve some cloud processes explicitly, they rely on microphysics (MP) schemes to handle important microscale processes that affect the growth and movement of convective events. MP schemes primarily distribute atmospheric water mass into different hydrometeor classes (e.g., water vapor, cloud droplets, cloud ice, and various forms for precipitation) as the simulation evolves. In addition to hydrometeor type, MP schemes also provide information about the particle-size distribution (PSD) of each hydrometeor group.

The majority of MP schemes available for use in WRF are "bulk" schemes, which use a prescribed curve shape and a series of prognostic equations to characterize hydrometeor PSDs as simulations progress. Generally, the distribution curve is in terms of a number concentration, $N(D)$, where N is the number of particles per unit volume, and D is the particle diameter. The modeling community often describes these schemes according to the number of statistical properties called "moments" they solve. By definition, the nth cumulative moment, M_n, of a PSD equates to

$$M_n = \int_0^\infty D^n N(D) dD. \quad (2)$$

As described by Jones (2014), moments provide information about PSD curve location, spread, symmetry, and peakedness, which MP schemes leverage to diagnose hydrometeor attributes of interest. For example, the zeroth moment, M_0, is simply $N(D)$; the ratio of the first moment, M_1 to M_0, provides the overall mean particle diameter; and the third moment, M_3, is the particle mass mixing ratio. Accordingly, moments enable bulk MP schemes to relate other known hydrometeor characteristics to the shape of the PSD curve.

Typically, bulk MP schemes use calculated total particle mass content (diagnosed from the mass mixing ratio) along with assumptions about bulk density and particle shape to adjust $N(D)$ over time. Some MP schemes also explicitly solve for particle number concentration (i.e., the density of particles for a given size instead of all sizes treated in bulk), which provides an additional degree of freedom for predicting changes to $N(D)$. The modeling community generally refers to a bulk MP scheme that solves a given hydrometeor's mass mixing ratio but prescribes its $N(D)$ as a "single-moment" scheme. Likewise, "double-moment" schemes diagnose both

parameters. Explicitly predicting multiple moments generally improves the overall accuracy of simulated particle fall speeds, cloud structure, and precipitation accumulation; however, doing so requires additional processing. Consequently, fundamental differences between commonly used bulk MP schemes primarily reflect the number of hydrometeor classes and moments calculated within the scheme.

We selected the Thompson MP scheme (Thompson et al. 2008) for our CTRL configuration based on its use in the operational HRRR model. We also assessed an alternate configuration using the WRF Single-Moment 6-Class (WSM6) scheme (Hong et al. 2006) to test the sensitivity of our forecasts to MP selection. Both of these MP schemes incorporate the various hydrometeor species typically found in warm-season convective systems (e.g., water vapor, cloud droplets, rain, cloud ice, and graupel). The Thompson MP scheme, however, is double-moment for cloud ice and rain. WSM6, on the other hand, uses only single-moment calculations.

2.2.8 Initialization time (model spin-up)

Spin-up refers to the early stages of a simulation when the model is adjusting from its initialization state to its own, thermal-dynamically "balanced" state. Generally, appropriate spin-up time allocations depend on the application of interest. For example, mesoscale atmospheric applications (like ours) typically require only a few hours of spin-up time, whereas slowly evolving features like soil moisture state may take several years.

All of our simulations initialized at 0000 UTC on the first day of the case study period. In Mountain Standard Time (MST; local time for Arizona), 0000 UTC equates to 1700 MST the previous day. Our default spin-up period occurred in the evening hours and overnight, allowing plenty of time for the model to adjust and capture the diurnal heating cycle as convection progressed. We also assessed an alternate configuration set to start at 1200 UTC the day before the first day of the case study period (i.e., 12 hr earlier) to see if the additional spin-up time improved simulation outcomes.

Table 2. List of variables and options critical to the WRF configuration and justification for their selection.

Parameter	Option	Configuration Label	Comments
WRF Version	4.1	—	WRF version release associated with the most recent substantial update to the WRF-Chem dust transport algorithms
Time Step	90s	—	Time step appropriate for preserving model stability relative to resolution
CTRL Initialization Time	0000 UTC on the first day of the case study period	CTRL	Initializes model around 1700 MST (local time in Arizona)
Alternate Initialization Time	1200 UTC on day before the first day of the case study period	12hrInit	Initializes model around 0500 MST
CTRL Resolution	d01: 18 km d02: 6 km d03: 2 km	CTRL	Guidance from Cao and Fovell (2016) suggests 2 km grid-spacing is sufficient resolution for wind forecasting in complex terrain
Alternate Resolution	d01: 27 km d02: 9 km d03: 3 km	3km	Slightly coarser, equivalent to HRRR resolution at innermost domain
CTRL Initialization Dataset	RAP + NAM analysis (13 km and 12 km horizontal resolution respectively) (input every 3 hr)	CTRL	Provides relatively high-resolution initialization to reduce spin-up time
Alternate Initialization Dataset	GFS 0.5° analysis + 3 hr forecasts (input every 3 hr)	GFS	Secondary dataset included primarily for sensitivity analysis
CTRL Vertical Levels	42 hybrid terrain-following levels	CTRL	Default WRF v4.1 vertical levels
Alternate Vertical Levels	65 hybrid terrain-following levels	Vertres	Test convective vertical motion sensitivity to vertical resolution
CTRL Planetary Boundary Layer Scheme	MYNN	CTRL	Scheme used in the operational HRRR configuration; paired with the MYNN surface-layer scheme
Alternate Planetary Boundary Layer Scheme 1	MYJ	MYJ	Local scheme included for sensitivity analysis; paired with the MYNN surface-layer scheme
Alternate Planetary Boundary Layer Scheme 2	YSU	YSU	Nonlocal scheme included for sensitivity analysis; paired with the MM5 surface-layer scheme
CTRL Land Surface Model	Noah	Noah	Default WRF v4.1 LSM
Alternate Land Surface Model	NoahMP	NoahMP	Included for sensitivity analysis while remaining similar and comparable to Noah
CTRL Microphysics Scheme	Thompson	CTRL	Microphysics scheme used in the operational HRRR configuration
Alternate Microphysics Scheme	WSM6	WSM6	Single-moment scheme included for sensitivity analysis
Cumulus Scheme	New SAS	—	Used in all simulation but applied to only d01 and d02
Radiation Scheme	Rapid Radiative Transfer Model for Global Climate Models (RRTMG)	—	Applied to all simulations; scheme used in the operational HRRR configuration

2.3 Model assessment

We compared forecasts of 500 hPa heights and winds from d01 for each of our simulations against the associated parameters from the 500 hPa SPCHMA to determine the model's ability to reproduce relevant synoptic forcing conditions. If the position and amplitude of troughs, ridges, large-scale wind circulations, and areas of especially intense wind (e.g., jet streams and jet streaks) matched, we considered our forecasts skillful. When our simulations produced synoptic patterns with troughs or ridges considerably displaced, smoothed, or amplified compared to the SPCHMA product, we designated those forecasts as flawed or unskilled.

We also compared the SPCHMA 850 hPa analysis of height, wind, and dew-point temperature against forecasts of the same variables from d01. Additionally, we examined the 850 hPa SPCHMA precipitable water (PWAT) analyses against simulated PWAT values from d02. PWAT values indicate how much rain would fall if all of the water vapor within the atmospheric column condensed and fell as rain. If the location of the simulated moisture sources, low-level circulation pattern, and gradient in PWAT matched closely between analyses and forecasts, we deemed our simulations to be skilled. Simulations were inadequate if the preconvective environment contained substantially more or less moisture, the model produced displaced or rotated moisture gradients, or atmospheric moisture originated from inappropriate sources due to discrepancies in low-level circulation.

We evaluated the location and timing of convective initiation by comparing the observed NEXRAD imagery and 1 km AGL simulated radar reflectivity within d03. While NEXRAD imagery is a composite of several beam heights, AGL radar coverage in the DSWUW is most reliable around 1 km AGL due to beam blockage of higher heights by topographical features and backscattering closer to the ground from lofted or transient dust and other particles. Because of this, we do not expect comparisons of observed NEXRAD imagery and simulated radar to match perfectly. Despite these flaws, NEXRAD imagery allowed us to validate the structure (i.e., convective mode), intensity, and translation (i.e., forward motion) speed throughout each event. When forecasted convection matched the observed convective structure and attributes, we deemed our simulations skillful. Conversely, we considered our forecasts poor when the model produced other types of convection or failed to simulate an observed change in convective structure.

Regarding convective mode characterization, we classified storm structures as isolated cells, clustered cells, supercells, quasi-linear convective systems (QLCSs), or mesoscale convective systems (MCSs). Isolated cells (sometimes called "popcorn" convection) usually grow and decay within an hour. In contrast, clustered cells create regenerative conditions through updrafts (i.e., rising currents of air) that form along the leading edge of rain-cooled air (i.e., gust fronts). Under clustered cell conditions, individual convective cells usually last 30 to 60 min, but the system as a whole may last for several hours. Supercells are long-lived (1 hr or more), highly organized storms driven by tilting and rotating updrafts. A QLCS (commonly referred to as a squall line) is a line of thunderstorms that forms along or ahead of a cold front, and an MCS is a collection of "merged" thunderstorms that acts as a larger-scale system (usually spanning the length of a state or more).

Because of the importance of surface wind speed to lofting dust, we verified simulated surface wind speed time series from grid cells within d03 against observations from the ASOS and RAWS networks. While we considered all available observations in our validation, we placed more emphasis on stations located nearest individual dust events. Additionally, we compared averaged network-based wind speed time series to time series of simulated surface wind speeds calculated by averaging values from grid cells with locations corresponding to an observation site. This approach allowed us to smooth over spurious errors associated with individual locations and to gain a general sense of overall surface wind forecast skill within the entirety of d03. As noted previously, RAWS observations have no uniform reporting time, so we averaged observations from this network to the top of the closest hour to account for discrepancies in reporting time. Our evaluation considered a forecast skillful if the simulation reproduced the observed wind speed evolution over time with no obvious systematic errors in phase or amplitude for both the network average and individual stations located near areas of convective initiation or peak intensity.

For a more quantitative assessment, we calculated wind speed forecast bias for individual station locations. We also investigated biases averaged in time (average station bias), averaged in space (average forecast-hour bias), and averaged in both (event network average bias). Furthermore, we assessed model fidelity by calculating the absolute value of average bias for each network and individual stations. If simulated average bias magnitudes exceeded the variability of the wind speed (U_v) throughout the event

by an order of magnitude or more, we considered the model to have poor skill. Here, we define wind speed variability as

$$U_v = U_{max} - U_{min}, \quad (3)$$

where U_{max} and U_{min} are the maximum and minimum wind speeds associated with the location of interest over the event duration, respectively. We also designated simulations as unskillful if large (e.g., ±1 m s^{-1}) persistent network average biases occurred throughout the entirety of the event.

2.4 Case studies

To support our model-testing efforts, we first created an inventory of convective dust-storm events to potentially simulate within the DSWUS area. Our initial starting pool consisted of 26 prospective options from previously published studies, including 21 from the paper by Lei and Wang (2014) and 7 from the article by Hyde, Mahalov, and Li (2017), with two cases overlapping. Additionally, Huang et al. (2015) provided an extensive overview of a single case study also discussed briefly in Lei and Wang (2014) and Hyde, Mahalov, and Li (2017), making it a strong candidate for selection. Because of our decision to use the RAP analysis as initial conditions for our WRF model, we considered only those case studies occurring after 1 May 2012 for final selection, reducing our pool of case studies down to 11. Using case studies from existing literature enabled us to expedite much of our analysis as these papers also provide overviews of observed storm structure, weather-system dynamics, and observation data sources.

We also sought out additional case study candidates by searching the archived storm reports from SPC (2022b). We developed and used an algorithm (see Appendix A) to download daily archived storm summaries in plain text format from January 2003 (first full year of archived data) through May 2019 and to search for severe wind reports (i.e., instances where reported winds exceeded 65 kn or 33.44 m s^{-1}) with comments that explicitly mentioned “dust” or “visibility.” By using this search criterion, we guaranteed that any records returned would contain verified lofted dust in a high-wind environment typical of a dust storm. Our query of the SPC database identified 24 potential cases, 21 unique cases and 3 overlapping with those in literature, within the DSWUS region, 14 of which fell within the time window of RAP analysis data availability. Between the two methods, we acquired a total of 24 possible case studies to explore (see Appendix B for a complete list).

Figure 3. NEXRAD (Next Generation Weather Radar) composite radar reflectivity images at the peak time during each of the five case studies selected: (*A*) 0000 UTC, 4 July 2014; (*B*) 2200 UTC, 21 August 2014; (*C*) 0000 UTC, 28 June 2015; (*D*) 0000 UTC, 1–2 August 2017; and (*E*) 0030 UTC, 30 July 2018.

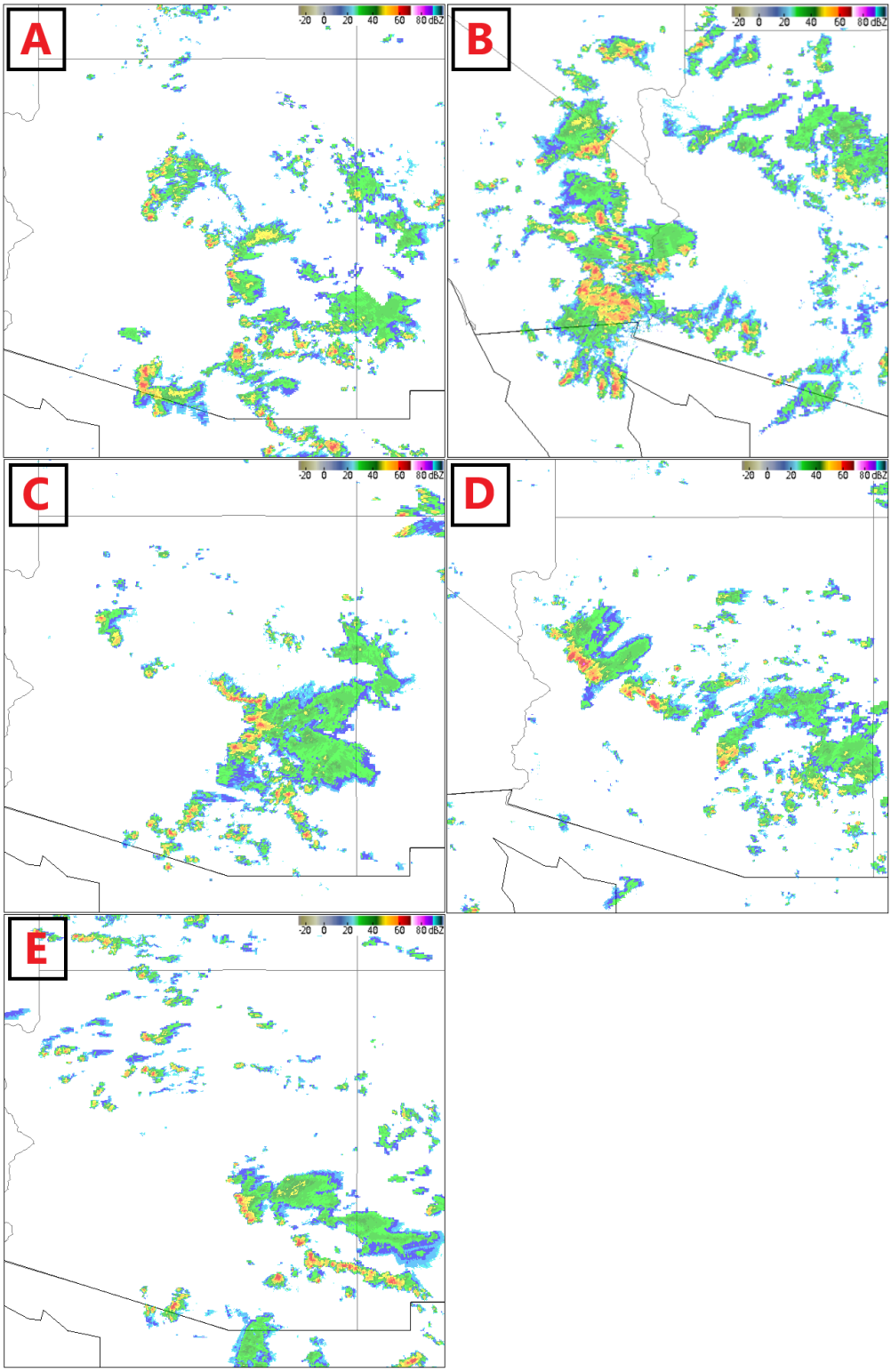

For the sake of time management, we opted to limit the total number of case studies selected for our WRF-model efficacy tests. We considered each case based on its societal effect, type and complexity of convection, synoptic conditions, geographic area, and proximity to observations for verification. To represent a variety of locations, convective types, event durations, and background flow regimes, we chose five distinct case studies from the initial list for further review. Our final five dust events occurred 4 July 2014, 21 August 2014, 28 June 2015, 1–2 August 2017, and 30 July 2018. These case studies exhibit a variety of convective modes, including multiple parallel convective bands, splitting or merging convective lines, and clustered cells developing into an MCS. Figure 3 provides radar images at the times of peak intensity for each event and highlights the individuality of each case. We present a more detailed overview of each case study in the following section.

3 Results

This section provides a detailed meteorological analysis and model evaluation for each case study event. Figure 4 serves as a guide for geographical features referenced throughout the text.

Figure 4. Important physiographic features referenced throughout case study analyses. The bottom image is a zoomed-in representation of the area outlined by the *solid red line* in the *top* image.

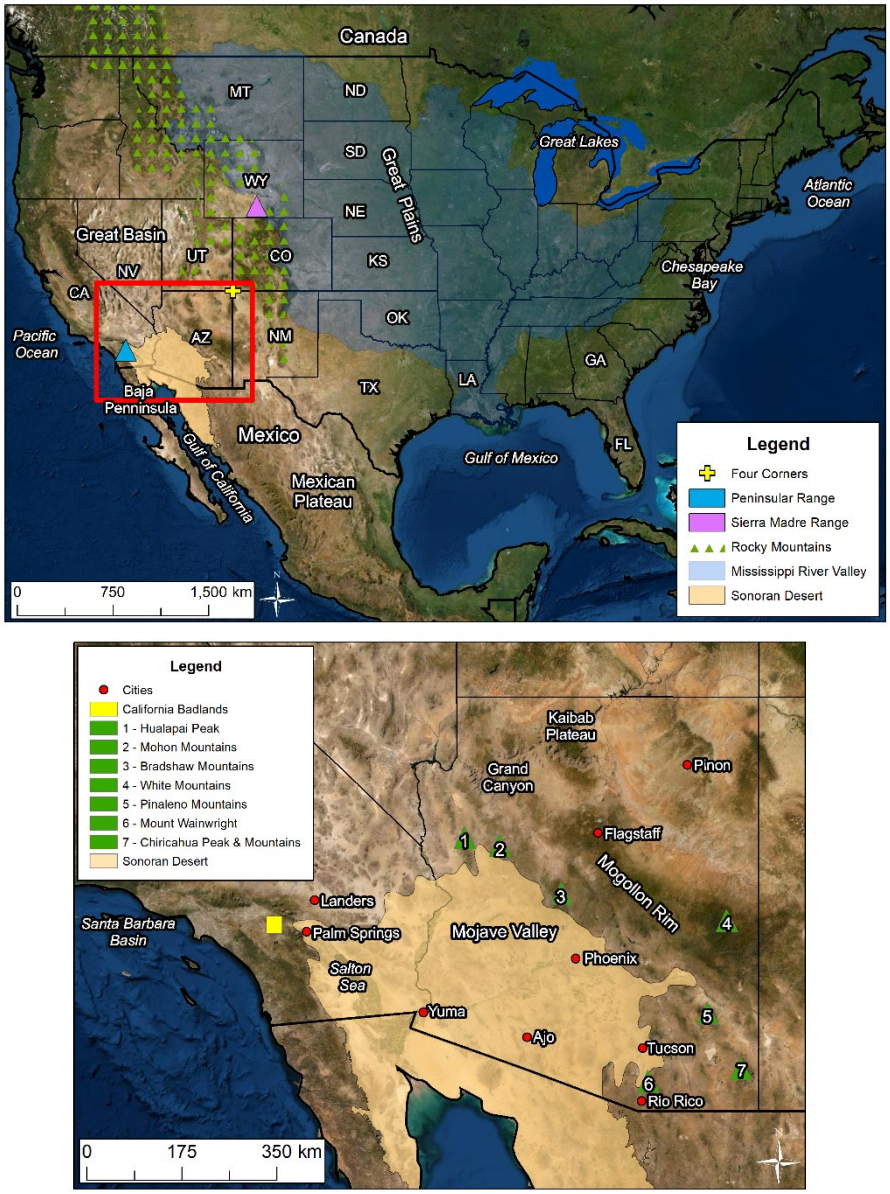

3.1 4 July 2014 case study

3.1.1 4 July 2014 event overview

Our first dust-event case study, which affected much of central and southern Arizona, primarily occurred on 3 July 2014. The event began at 1800 UTC, 3 July; peaked around 0000 UTC, 4 July; and concluded mainly by 1200 UTC, 4 July. The synoptic setup for this case is typical of the summer phase of the North American Monsoon over the DSWUS (e.g., Adams and Comrie 1997), a seasonal wind-shift pattern caused by intense solar heating. Under monsoon conditions, a zone of high pressure sets up over the Four Corners region, drawing winds from the east and southeast aloft. The intense surface heating also causes a trough of low pressure (i.e., a thermal low) to develop over the western DSWUS and the Mexican Plateau. This characteristic pressure pattern transports moisture-laden air masses from the Gulf of California, Gulf of Mexico, and the southern plains into the region, creating ideal conditions for convective weather, especially over mountainous terrain.

Figure 5 shows the SPCHMA 500 hPa analysis on 1200 UTC, 3 July (hereafter considered preconvection), and 0000 UTC, 4 July (hereafter designated as peak-convection). At the preconvection time, a moderately amplified ridge-and-trough wave pattern spanned the majority of the CONUS with a large ridge centered over the Four Corners region and a downstream trough positioned over the Great Lakes region, just east of the Mississippi River Valley. This upper-level flow pattern provided large-scale clockwise wind rotation, overall high pressure, and nearly complete removal from any synoptic-scale forcing that could promote widespread convective activity over the Four Corners region. At the peak-convective time, the 500 hPa pattern changed only slightly. The ridge weakened marginally and gradually progressed east, centering over central Wyoming. However, the overall clockwise rotation of the 500 hPa winds remained fixed over the Four Corners region, providing a continuous flow over Arizona that shifted from east-southeast in the southern region to south-southwest over the western half of the state. These winds also transported upper-level moisture from the Gulf of Mexico over the Four Corners region. Of note, this particular synoptic pattern matches incredibly well with common DSWUS dust forcing conditions described by NOAA (see Dust Storm Pattern 1B in Lader et al. 2016).

Figure 5. SPCHMA (Storm Prediction Center Hourly Mesoscale Analysis) 500 hPa height (*contoured*) and wind (*barbs* and *shaded*) (*panels A* and *B*) and 850 hPa height (*contoured*), wind (*barbs*), and dew point (*shaded*) (*panels C* and *D*) valid at 1200 UTC, 3 July 2014 (*A, C*), and 0000 UTC, 4 July 2014 (*B, D*).

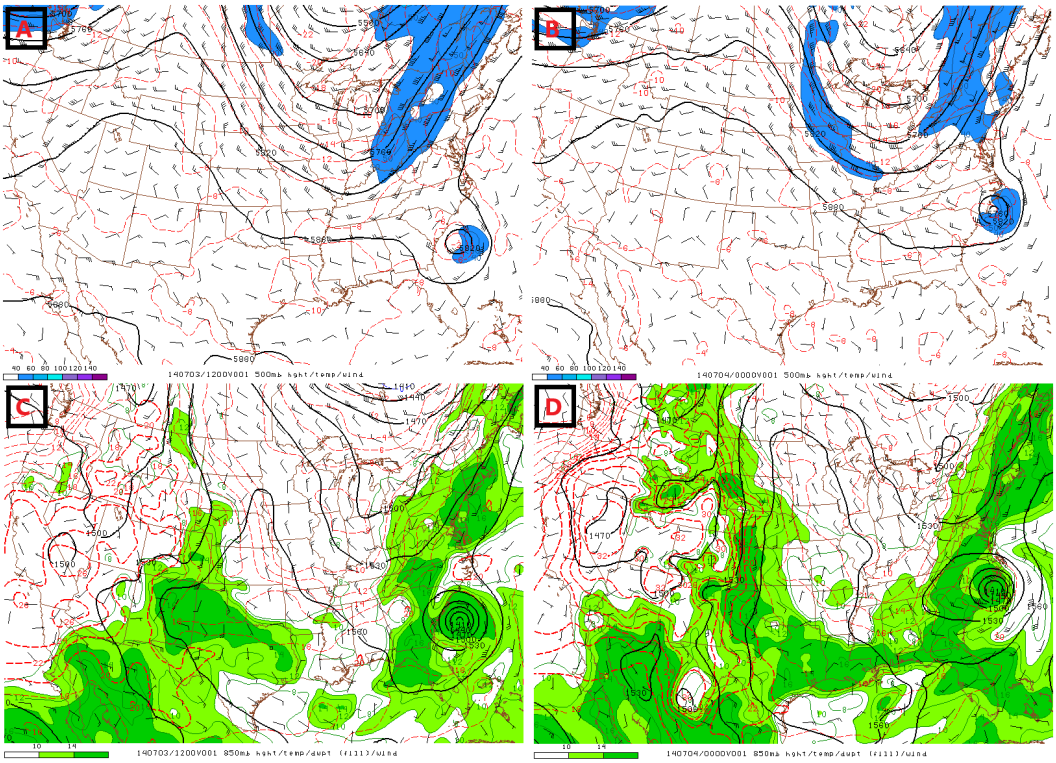

At lower levels of the atmosphere, the SPCHMA 850 hPa analysis, shown in Figure 5, reveals moisture sources in the preconvection environment. At this level, east-southeasterly winds flowed from the Gulf of Mexico across Texas into southern New Mexico and Arizona. Additional moisture, transported in by the south-southwesterly winds from the Gulf of California, extended upward through the western half of Arizona. These two flow patterns together provided ample moisture to sustain intense convective storms throughout the central, southern, and western portions of Arizona (anything southwest of the Mogollon Rim). The preconvection height patterns in Figure 5 indicate an extension of high pressure into northeast Arizona, creating a general pressure gradient across the Mogollon Rim and the White Mountains. Later, during the peak of the event, the 850 hPa pressure gradient becomes less well defined over Arizona, removing the influence of large-scale steering.

Lastly, NEXRAD radars captured the resulting convective storms responsible for dust mobilization and transport. Figure 6 shows the evolution of the NEXRAD radar composite over the state of Arizona.

Figure 6. NEXRAD radar composite imagery for the 4 July 2014 case for 1800 UTC, 3 July 2014 (*A*); 2000 UTC, 3 July 2014 (*B*); 2200 UTC, 3 July 2014 (*C*); 0000 UTC, 4 July 2014 (*D*); 0200 UTC, 4 July 2014 (*E*); 0400 UTC, 4 July 2014 (*F*); and 0600 UTC, 4 July 2014 (*G*).

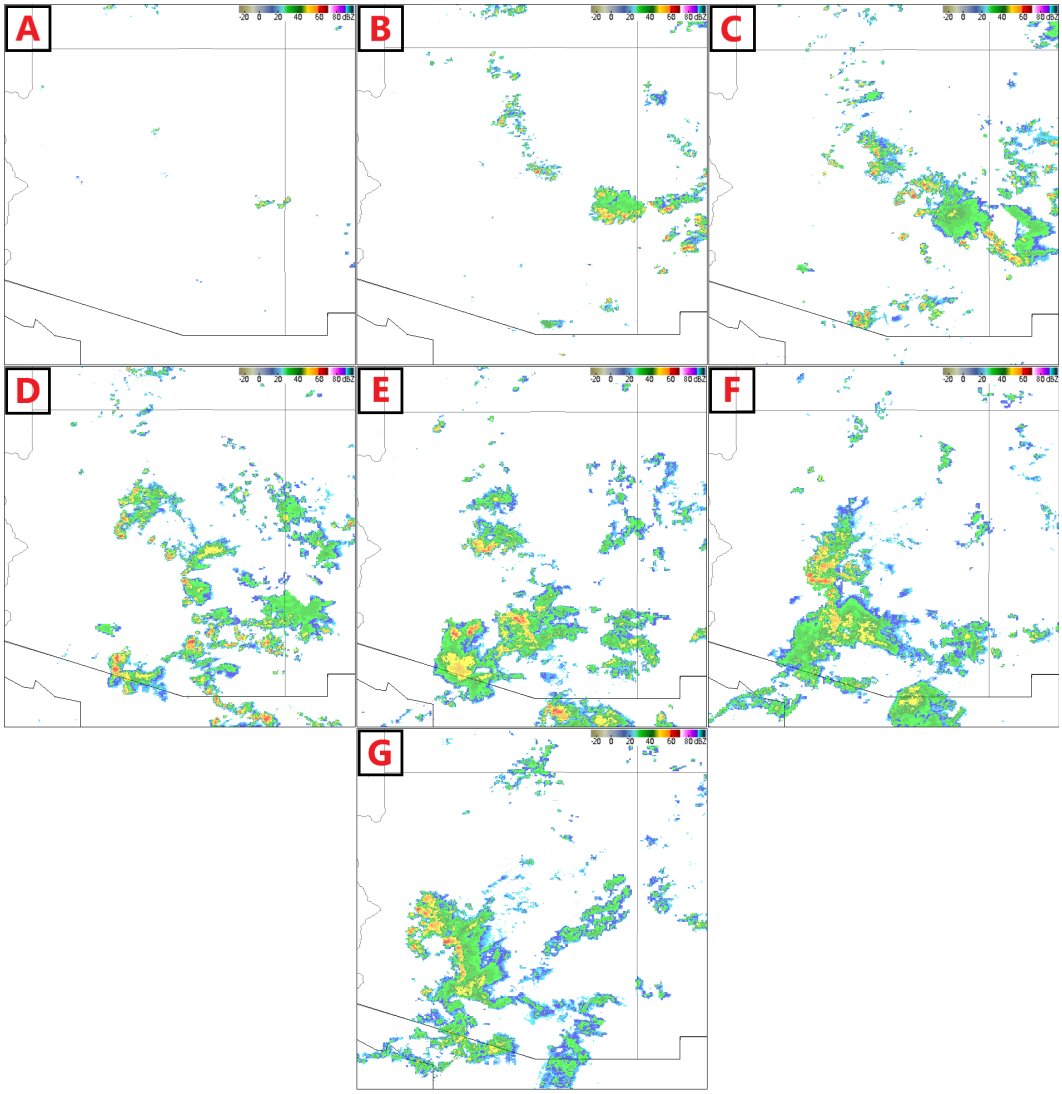

At 1800 UTC, 3 July, convection began to develop over the White Mountains. Additional thunderstorms quickly developed by 2000 UTC, 3 July, popping up in a ring centered over the Four Corners, and began to rotate clockwise with the steering flow. At this time, thunderstorms began to form over the more isolated peaks, like Chiricahua Peak and Mount Wrightson, in southern Arizona; and the initial convection organized into a QLCS moving rapidly down the topography, leaving behind stationary reflectivity values, which likely led to lofted dust. By 2200 UTC, 3 July, the leading edge of the QLCS collapsed; but the surrounding convection intensified, forming a line of broken thunderstorms outlining the edge of the Mogollon Rim. Also, convection near the southern peaks began to organize

into larger groups of cells. At the peak of the event, 0000 UTC, 4 July, convection organized into an extensive north–south line rotating clockwise about its northern end while convection over the White Mountains began to decay as it moved downslope. Convection, initially formed in the southeast corner of Arizona, traveled rapidly ahead of the line and approached the eastern edge of the Sonoran Desert. At 0200 UTC, 4 July, the large convective line collapsed into three clusters of cells, each exhibiting their own behavior. The northernmost cluster began to move south-southwest. Conversely, the central cell just south of Phoenix continued to progress west-northwest, and the southernmost cell on the border of Mexico migrated west and began to decay. The remnants of the line also caught up with the western cluster of convection, which began to converge with the northern and central cell clusters. Finally, by 0400 UTC, the cellular clusters merged into a north–south line, which traversed northwest and reorganized into a QLCS with an orientation parallel to its motion.

3.1.2 4 July 2014 simulation results

Figure 7 shows the SPCHMA and CTRL simulation of the 500 hPa flow pattern. The CTRL captured the upper-level pattern quite well, reproducing the same ridge-and-trough patterns centered over the Four Corners and Great Lakes regions, respectively. The CTRL also forecasted the same pockets of higher wind speeds saddling either side of the ridge axis and the broad, clockwise circulation dominating the Four Corners region. Furthermore, the CTRL was able to predict the slight flattening of the ridge and appearance of shortwave noise upstream of the ridge axis between 1200 UTC, 3 July, and 0000 UTC, 4 July. While the circulation was offset slightly to the southwest in the CTRL forecast compared to the SPCHMA, we still considered the CTRL simulation highly skillful. It reproduced the general synoptic features and placements that created weak large-scale forcing and localized circulations needed for convective activity in the DSWUS.

Figure 7. SPCHMA (*panels A* and *B*) and WRF CTRL d01 forecast (*panels C* and *D*) of 500 hPa height (*contoured*) and wind (*barbs* and *shaded*) valid at 1200 UTC, 3 July 2014 (*A*, *C*), and 0000 UTC, 4 July 2014 (*B*, *D*).

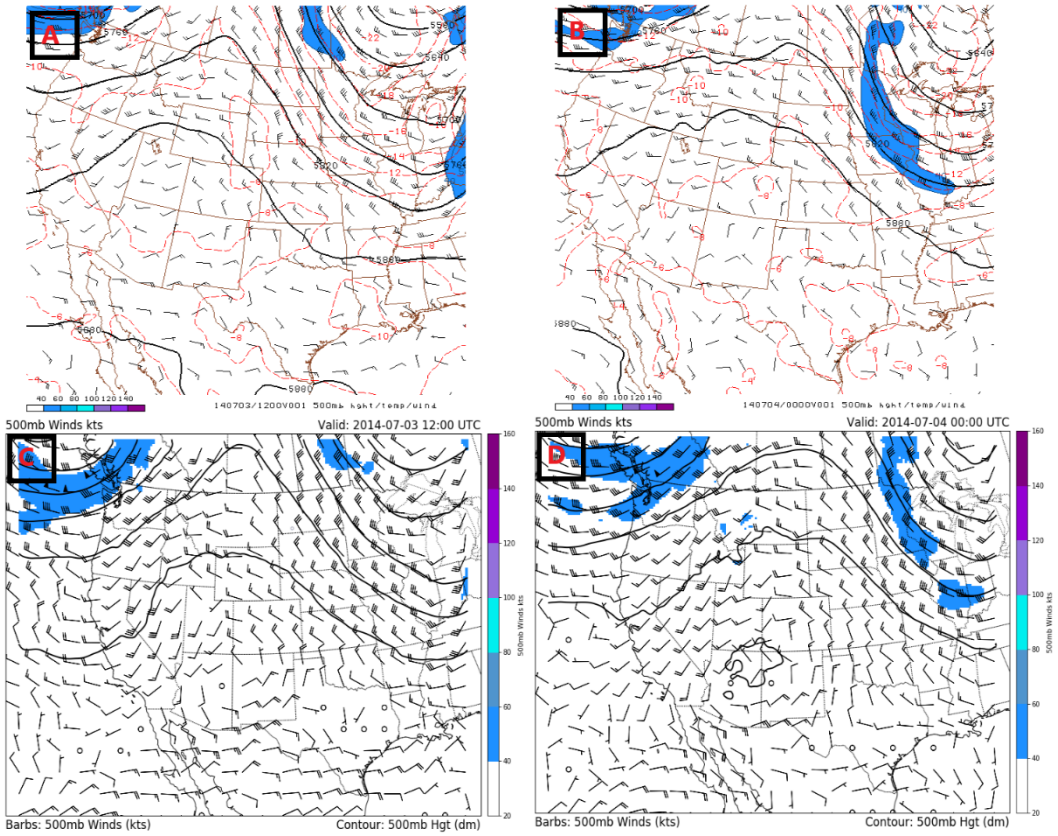

In the lower levels of the atmosphere, the CTRL performed similarly well. Figure 8 compares the SPCHMA and CTRL forecasts for the 850 hPa flow pattern and dew-point temperature. The patterns match well between the two, with both characterized by elongated north–south high pressure and clockwise flow over the central plains and east-southeasterly flow off the Gulf of Mexico. Additionally, the CTRL reproduced the shift of winds over the Gulf of California from weak and disorganized at 1200 UTC, 3 July, to a coherent south-southwesterly flow that brought moisture into southwest Arizona, which lead to realistic atmospheric moisture content forecasts (e.g., Figure 9). The CTRL forecasted 1–1.5 in. of PWAT over the southern half of Arizona.* As the simulation evolved, PWAT increased ahead of peak convection, particularly in the southwest corner of the state, which provided realistic moisture sources and steering flow for developing convection.

* Our report elects to reference precipitable water values in terms of inches of depth rather than the SI standard of kilograms per cubic meter to be consistent with NOAA reporting and products. For reference 1 in. is equivalent to 25 kg/m^3.

Figure 10 compares the evolution and structure of the resulting convective systems through NEXRAD radar composites and the CTRL simulated 1 km AGL reflectivity. Between 1800 UTC and 2200 UTC on 3 July, the observed and simulated radar signatures matched quite well. Convection initiated at 1800 UTC in both the observations and CTRL forecast over the White Mountains, forming a QLCS as convection continued to spawn along the Mogollon Rim. At 2200 UTC, 3 July, the CTRL forecasted a line of convection along the ridge, curving from north to east as isolated cells in the southern region formed convective clusters moving west. At the peak of the event, the forecasted convection structure matched reasonably well with the observed pattern. Both showed a broad curving north–east line of convection extending from Flagstaff to the White Mountains, with weaker convection to the northwest and a more intense southern portion oriented west–east. The CTRL also captured the growing cluster of convective cells in southwest Arizona ahead of the convective line, taking on a more linear north–south orientation.

Figure 8. SPCHMA (*panels A* and *B*) and WRF CTRL d01 forecast (*panels C* and *D*) of 850 hPa height (*contoured black*), wind (*barbs*), and dew point *(shaded*, Celsius) valid at 1200 UTC, 3 July 2014 (*A, C*), and 0000 UTC, 4 July 2014 (*B, D*).

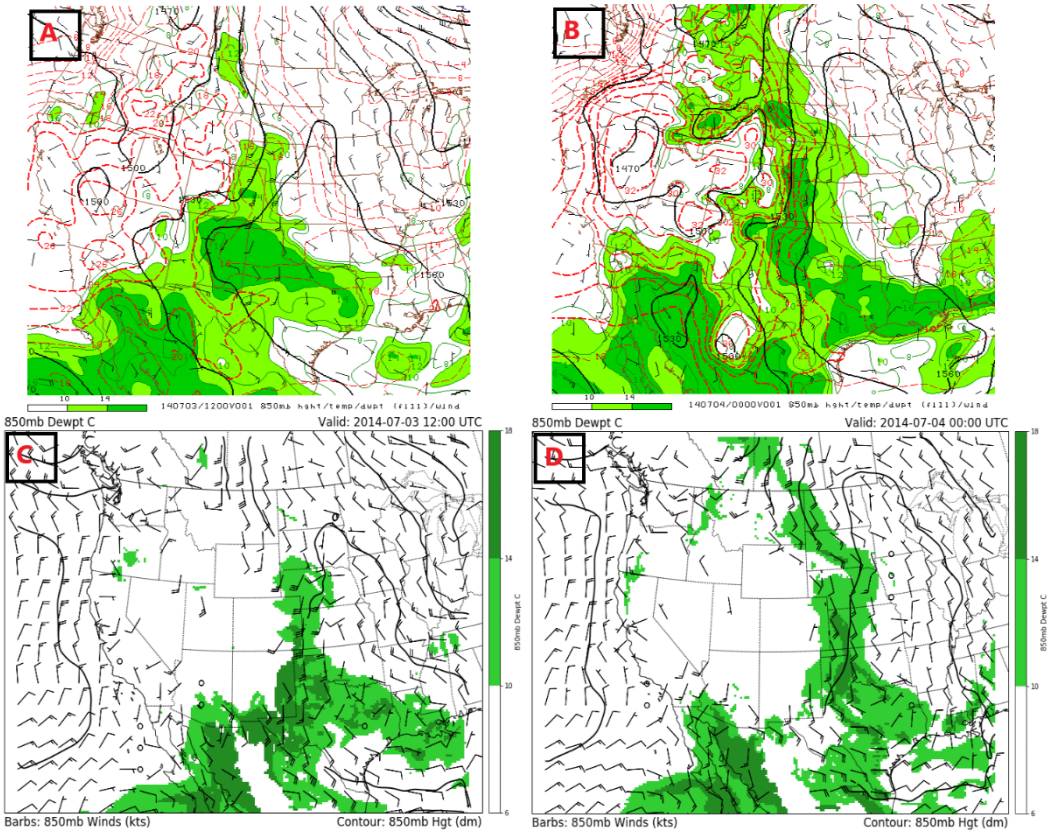

Figure 9. SPCHMA (*panels A* and *B*) and WRF CTRL d02 forecast (*panels C* and *D*) of column-integrated precipitable water (under 400 hPa, *shaded* and *contoured* in inches) valid at 1200 UTC, 3 July 2014 (*A*, *C*), and 0000 UTC, 4 July 2014 (*B*, *D*). Contours are every 0.1 in.

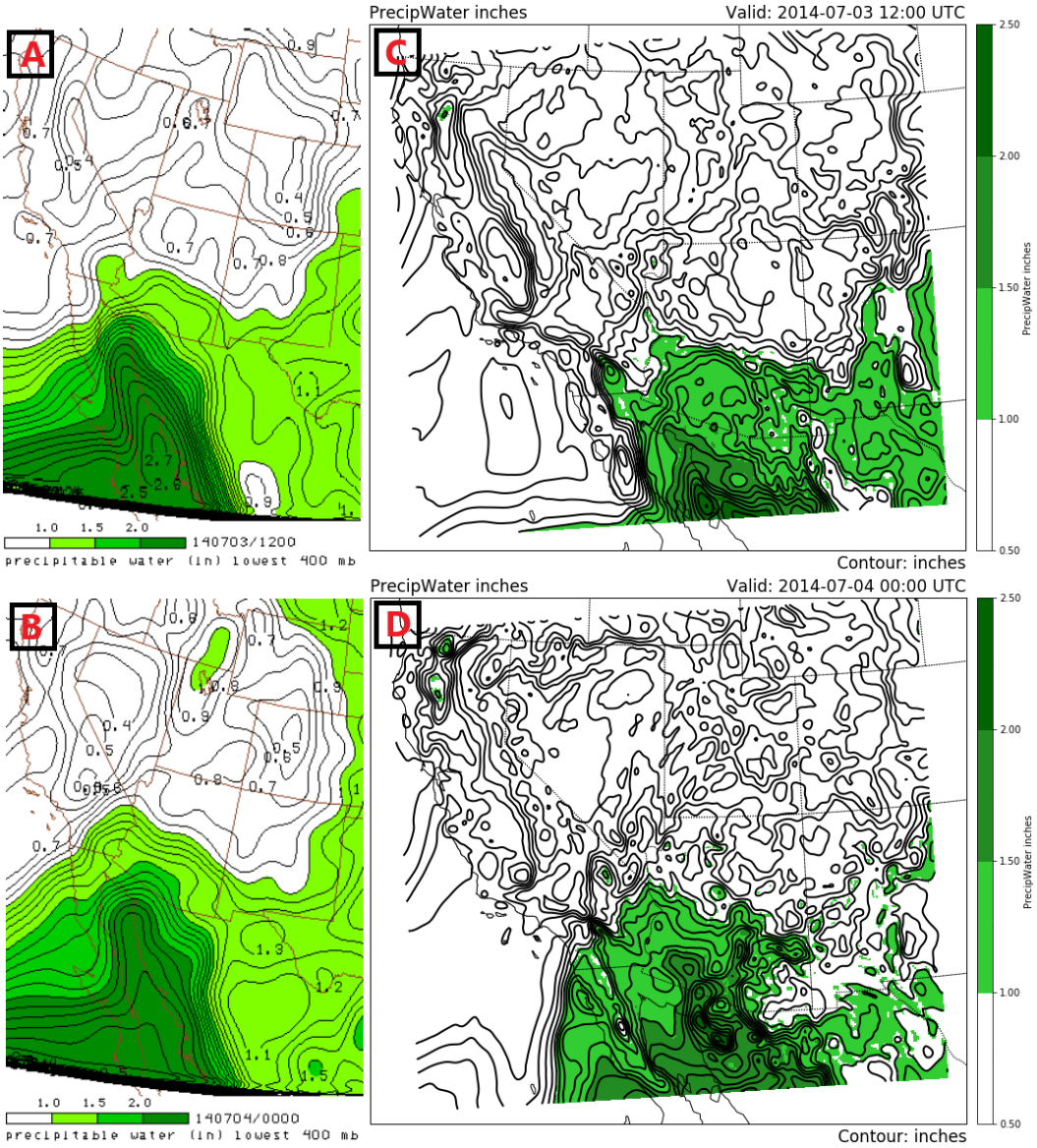

Figure 10. Observed NEXRAD radar (*panels A–F*) and WRF CTRL d03 simulated 1 km AGL (above ground level) radar (*panels a–f*) for 2000 UTC, 3 July 2014 (*A*, *a*); 2200 UTC, 3 July 2014 (*B*, *b*); 0000 UTC, 4 July 2014 (*C*, *c*); 0200 UTC, 4 July 2014 (*D*, *d*); 0400 UTC, 4 July 2014 (*E*, *e*); and 0600 UTC, 4 July 2014 (*F*, *f*).

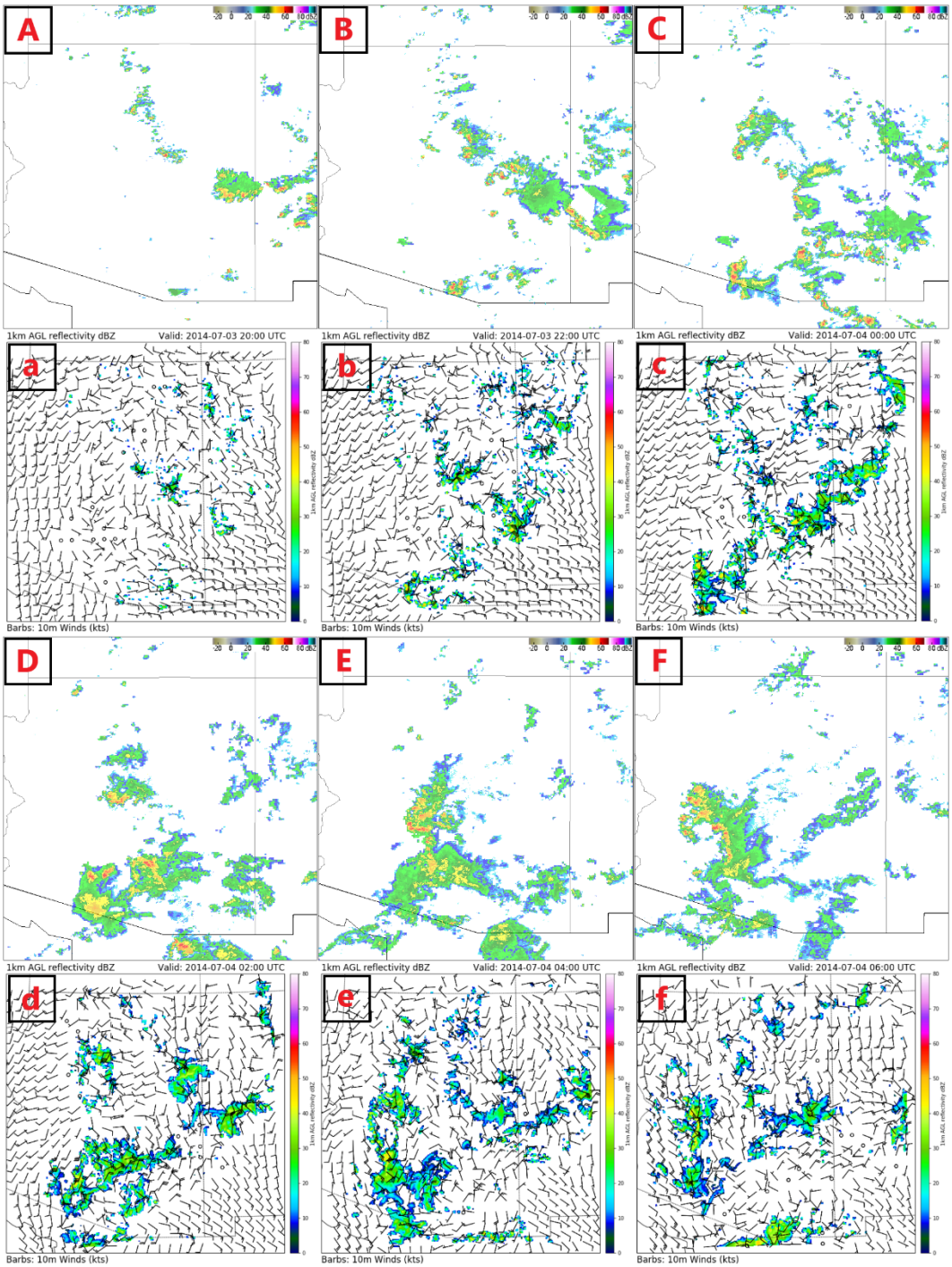

Still, the CTRL simulation was not perfect; it lacked a trailing northwest–southeast convective line that passed over Tucson. The convective cores' reflectivity values were slightly lower in the CTRL forecasts by up to 10

dBZ. However, this difference may be due to the radar composites rendering images from angled radar beams and the simulated reflectivity diagnostic representing values 1 km AGL.

As time progressed, the CTRL continued to produce skillful forecasts. At 0200 UTC, 4 July, the CTRL reproduced the three main clusters of convection in the western half of Arizona as they began to merge. By 0600 UTC, 4 July, these simulated cells successfully merged into a north–south convective line with a slight westward curve at the northern tip as stronger convection outran the southern half.

We assessed the ability of the CTRL to simulate the wind evolution over the entirety of d03 through network averages of all available stations within the domain. Figures 11 and 12 show time series of observed and CTRL-forecasted surface wind speed from 0000 UTC, 3 July, through 1800 UTC, 4 July, for ASOS and RAWS observations, respectively. In general, the CTRL simulated average surface winds at ASOS stations quite well, predicting a similar peak in wind speed, albeit 1 to 2 hr early and about 1 m s^{-1} more intense. The average bias for the entire forecast period was +0.59 m s^{-1}; however, a large portion of this overestimation occurred during nonconvective nocturnal hours (0500–1500 UTC, 3 July, and 0800–1600 UTC, 4 July).

Figure 11 also shows wind speed time series from four ASOS stations near the convective activity, including KSAD, KPHX, KSDL, and KDVT. KSAD is an ASOS station just south of the White Mountains in eastern Arizona, KPHX is in downtown Phoenix, and KSDL and KDVT are about 20 to 25 km north of Phoenix. The CTRL underforecasted the peak wind speeds at KSAD by about 5 m s^{-1} and overforecasted peak winds at both KSDL and KDVT by 2 to 6 m s^{-1}, approximately 1 to 2 hr too early. Despite these errors, our results suggest that our CTRL configuration simulated intense, short-duration peaks in wind speeds in d03 reasonably well for dust-modeling applications, especially at locations like KPHX, where forecasted winds matched the observed intensity very well with the peak arriving early by only less than an hour.

Alternately, the CTRL appeared to have markedly less skill forecasting conditions at RAWS stations. While the timing of low and peak wind speeds matched well, the CTRL severely and consistently overpredicted average surface winds with an average bias of +1.19 m s^{-1} and a network

average bias of +2.1 m s^{-1} during the peak of the event. This systematic overprediction may be the result of inappropriate aerodynamic surface-roughness values assigned to RAWS locations in the WRF framework, potential sheltering of observation stations from high winds by surrounding topography and obstacles unresolved in the model, model physics errors, or some combination of the three (e.g., Cao and Fovell 2018; Fovell and Gallagher 2018).

Figure 11. Time series of observed (*black*) and modeled (*red*) surface (10 m) wind speed during the 3 July 2014 dust storm for the network average of all ASOS stations (*A*), KSAD (*B*), KPHX (*C*), KSDL (*D*), and KDVT (*E*). The *gray line* in the network average shows the number of stations used in the network average. The 1 min observations are supplemented by METARs (Meteorological Aerodrome Reports) at individual stations when needed and are denoted by *dots*.

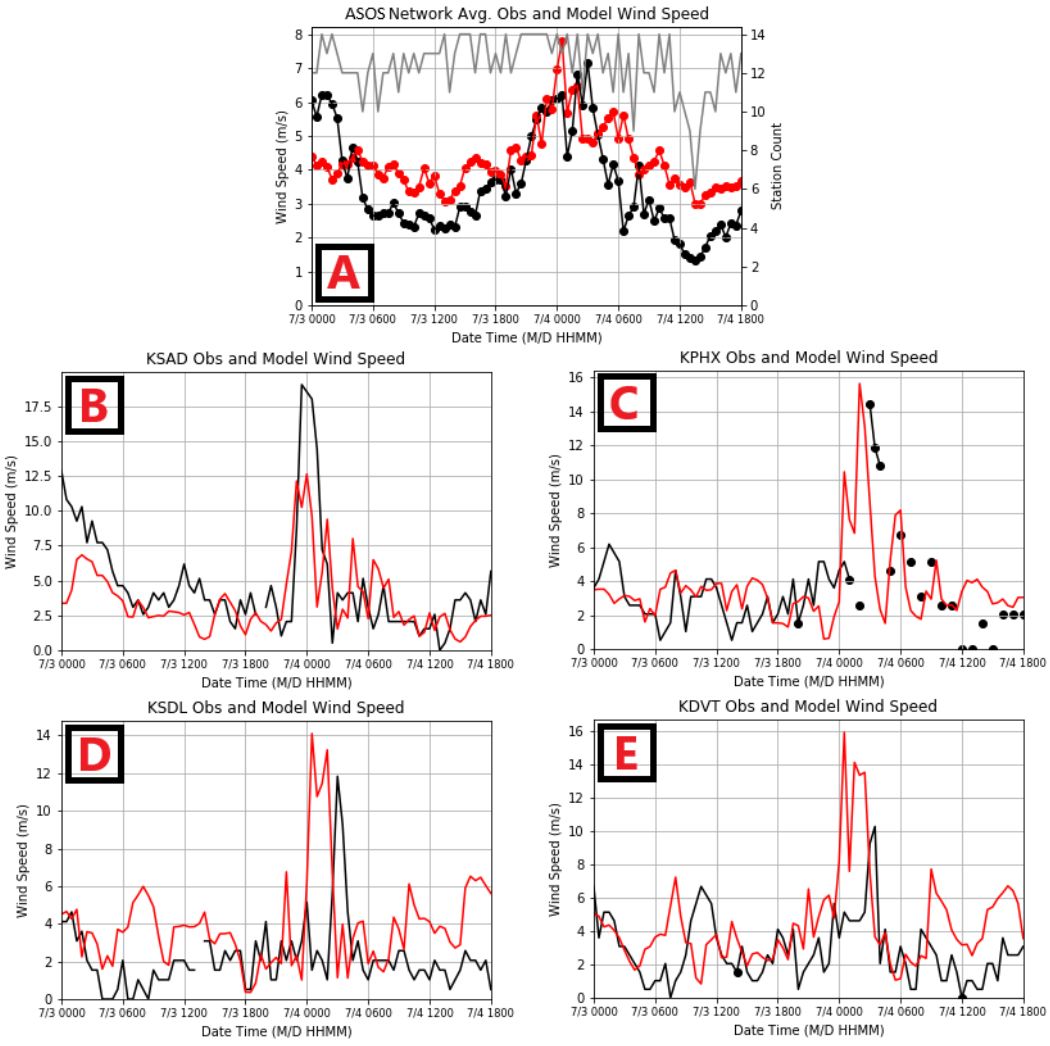

While the CTRL performed poorly compared to values averaged across the approximately one hundred RAWS stations in the domain, it performed much better at individual locations closest to the convective event. The

four RAWS stations in Figure 12 are GRAA3 near Coolidge; BLMA3, approximately 80 km west-northwest of Phoenix; and QSPA3 and QHBA3, both north of Lake Pleasant, respectively east and west of the Bradshaw Mountains. Each station comparison displayed unique behavior in terms of model skill. At GRAA3, winds prior to the event peak were underforecast by 2 m s^{-1} but matched the timing of peak winds at 0100 UTC, 4 July, quite well. The CTRL forecasted multiple peaks in wind speed associated with the passage of convective cells at BLMA3; but only one was observed, offset slightly from the second predicted peak. Farther north, the simulation forecasted winds at QSPA3 and QHBA3 excellently, with peaks in wind speed arriving 1 to 2 hr early but intensities matching near perfectly.

Figure 12. Similar to Fig. 11 except for the average of all RAWS stations (*A*), GRAA3 (*B*), BLMA3 (*C*), QHBA3 (*D*), and QSPA3 (*E*) surface (6.1 m) wind speed. *Dots* are used for individual stations since data are reported only once every hour with no specific reporting time.

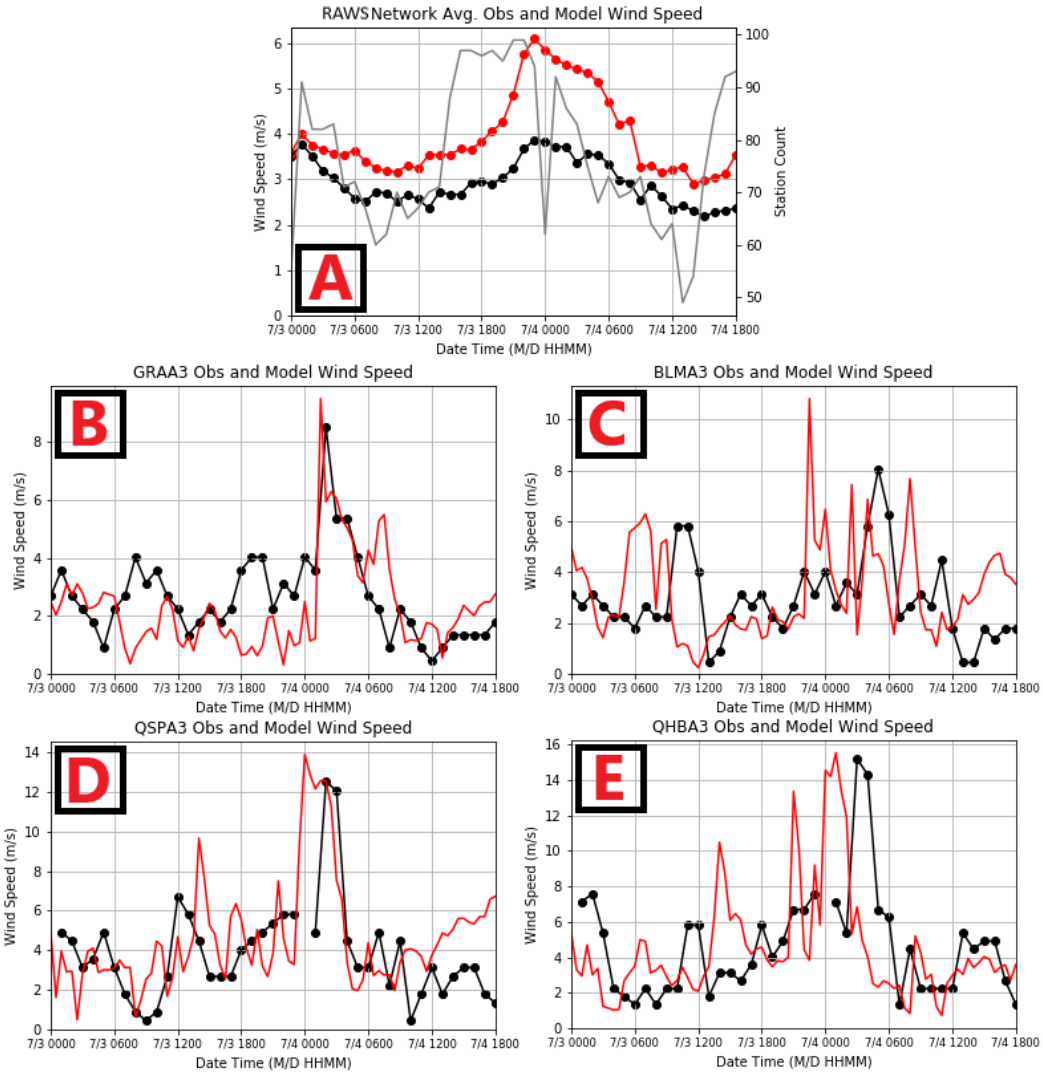

3.1.3 Model sensitivity analysis

We ran nine additional simulations for this case study, using the other WRF-model physics and configurations detailed in section 2.2 and Table 2 to test the sensitivity of the forecasted convective evolution and to identify combinations with potentially higher fidelity. The resulting convective evolution for each of these simulations was highly similar. As with the CTRL run, convection initiated over the White Mountains at approximately 1800 UTC in all cases, primarily in a northwest–southeast line that grew gradually over the Mogollon Rim. Each alternate simulation also produced multiple isolated cells in the southern half of Arizona that merged and organized into a larger convective line as they propagated westward.

Figure 13 shows the simulated radar reflectivity for each of the simulations at the peak of the event. The resulting overall convective structures were largely identical between model configurations. In general, each simulation produced a northwest–southeast line of convection along the Mogollon Rim, a leading north–south convective line in southern Arizona, and trailing a southwest–northeast line of reflectivity that wrapped around the eastern edge of the Mogollon Rim and extended into western New Mexico.

While the overall spatial patterns were similar, some differences between configurations were apparent. For example, reflectivity consolidated around the cores of convective activity in the simulation produced by the alternate MP scheme configuration (see Figure 13, WSM6, panel *B*). This pattern, along with a general lack of weaker reflectivity in the surrounding area, indicated that the WSM6 MP scheme led to tighter, stronger storms. There were also some differences in the reflectivity generated by one of our alternate PBL-scheme settings. The MYJ PBL configuration, henceforth MYJ, produced a stronger and broader wind field compared to the CTRL (see Figure 13; MYJ, panel *D*). Wind speeds in the MYJ simulation were 5 to 10 m s^{-1} stronger, especially in the vicinity and directly ahead (west-southwest) of convection coming off of the Mogollon Rim.

The resulting convection was much weaker than the CTRL when we altered the initialization time to 1200 UTC, 2 July, 12 hr earlier (see Figure 13, 12hrInit, panel *F*). The reflectivity of the 12hrInit simulation was similar to the WSM6 simulation in spatial extent but was lower in magnitude, indicating weaker and sparser convective activity. On further exploration, we found this was the result of overly intense pre-event convective activity

between 1800 UTC, 2 July, and 0000 UTC, 3 July, which dried out the environment before convective initiation for the main event. Similarly, the GFS-initialized simulation produced a more intense and progressive bowing convective system in southern Arizona and a weaker convective line along the Mogollon Rim compared to the CTRL (see Figure 13, GFS, panel *I*). This outcome was likely due to the coarser resolution of the GFS initialization, which resulted in the confinement of available atmospheric moisture to the southernmost region of Arizona and less moisture available downslope of the Mogollon Rim. Lastly, the simulation configured with lower horizontal resolution (see Figure 13, 3km, panel *G*) resembled a smoothed version of the CTRL run reflectivity. The alternate grid-scale configuration reproduced the overall shape and mode of the convection correctly but lacked some of the smaller, noisier aspects.

Figure 14 provides simulated surface wind speed (10 m AGL) results associated with our sensitivity study. Overall, the evolution of network average surface wind speed for both ASOS and RAWS was relatively consistent between model configurations. In general, all simulations agreed on the timing of wind speed lulls and peaks within an hour or two of each other. Each of the configurations also tended to overpredict average wind speeds overnight and through the morning between 0600–1600 UTC, 3 July, and 1100–1800 UTC, 4 July (corresponding to 2300–0900 MST and 0400–1100 MST, respectively), for the ASOS network. While all simulations captured the increase in wind speed between 2000 UTC, 3 July, and 0400 UTC, 4 July, they varied in the intensity of the peak and, in some cases, the number of peaks. The ASOS network average wind speeds predicted by the two alternate PBL configurations (MYJ and YSU) were approximately 1 m s^{-1} faster than the CTRL. Conversely, the GFS and 12hrInit forecast peak wind speeds were 1 m s^{-1} slower than the CTRL. The MYJ simulation, in particular, produced the most noticeable deviations compared to observations, with peak wind speed overpredicted by 3 m s^{-1} and a secondary peak slightly more intense, approximately 1 m s^{-1} faster, than those produced by the other configurations.

At KPHX, near the event epicenter, all model configurations generally agreed on the background wind speeds before and after the event (0000–2300 UTC, 3 July, and 0800–1800 UTC, 4 July, respectively). However, simulated peak winds for this location varied in the intensity and timing. The MYJ, WSM6, 3km, 12hrInit, alternate vertical resolution (VertRes), and YSU configurations predicted the wind speed peak for this location

approximately 3 hr too early. Furthermore, the MYJ configuration over-predicted wind speeds at KPHX by 8.5 m s^{-1}, and the 12hrInit simulation underpredicted the wind speed peak magnitude by 5 m s^{-1}.

Figure 13. Observed NEXRAD radar composite (*J*) and WRF d03 simulated 1 km AGL radar from various WRF configurations at 0000 UTC, 4 July 2014 (peak of the 4 July 2014 event): CTRL configuration (*A*), WSM6 (*B*), NoahMP (*C*), MYJ (*D*), YSU (*E*), 12hrInit (*F*), 3km (*G*), VertRes (*H*), and GFS (*I*).

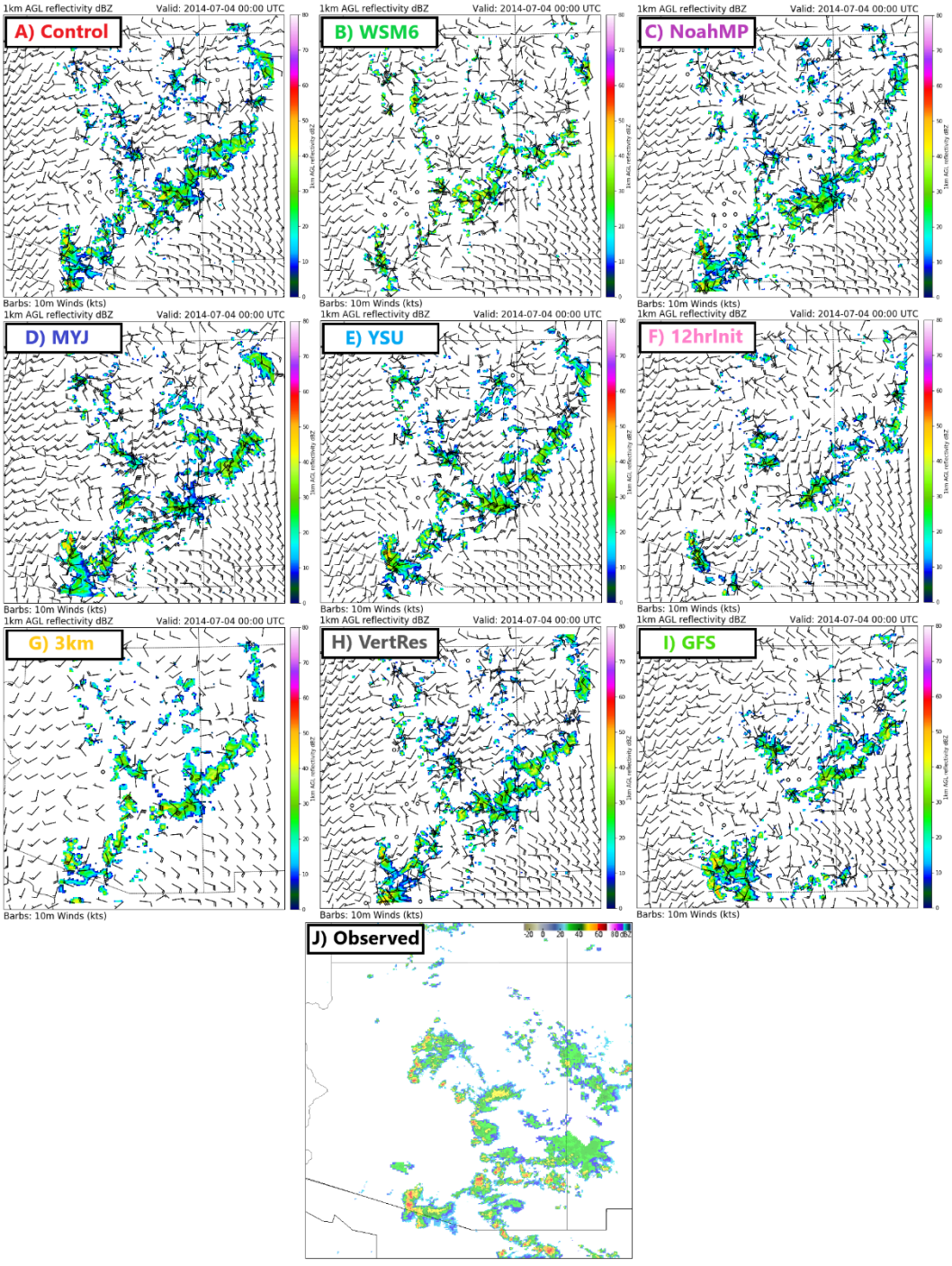

Figure 14. Observed and forecasted wind speed from all WRF simulations for ASOS (*A*) and RAWS (*B*) network averages and stations nearest the epicenter of the event, KPHX from ASOS (*C*) and GRAA3 from RAWS (*D*). Additionally, model-forecasted average wind speed mean absolute error (MAE) and bias (*E*) with ASOS verification in the *dots* and RAWS in *diamonds*.

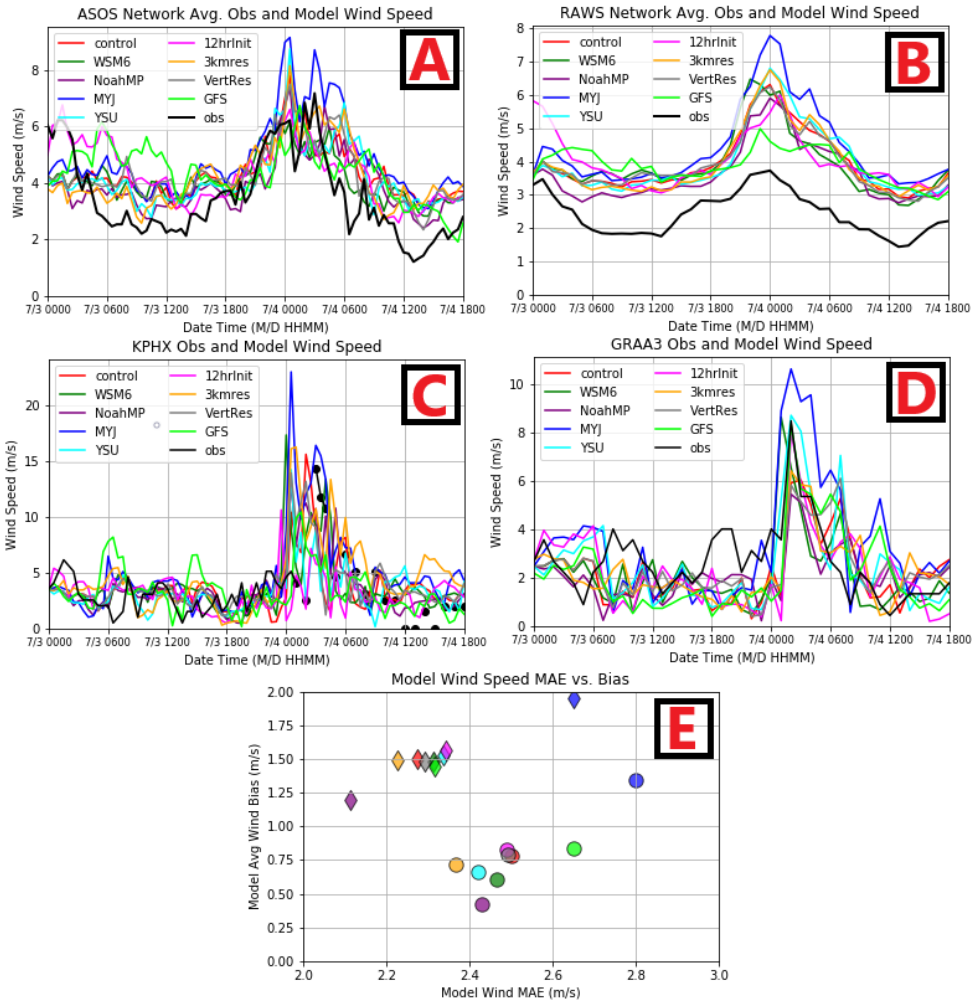

For the RAWS network average wind speed evolution, all model configurations systematically overpredicted surface wind speeds similar to the CTRL (Figure 14). The two extremes of this range were the MYJ and GFS simulations, which exceeded network average wind speeds at the peak of the event by 4 m s^{-1} and 1.25 m s^{-1}, respectively. However, this overprediction did not apply to all RAWS stations. One of the RAWS stations nearest the center of the event, GRAA3, just like in Figure 12, indicated skillful forecasts of surface wind speed. Each of the configurations forecasted a very similar evolution in wind speed for this location, peaking between 0100–0200 UTC, 4 July, with a secondary peak around 0600–0800 UTC, 4 July. Similar to what we observed with the average comparison of the

ASOS network, the MYJ and YSU configurations stand out as outliers with forecasted peak wind speeds 2 m s^{-1} greater than the CTRL.

Figure 14 also shows the average wind speed mean absolute error (MAE) versus bias for each configuration. Here, forecasts with lower MAE and biases closer to zero (i.e., closer to the lower-left corner of the plot) were more skillful. All configurations generally overpredicted wind speeds. For the ASOS network, the CRTL simulation appeared to be outperformed by the WSM6, YSU, 3km, and NoahMP configurations. For the RAWS network, only the 3km and NoahMP simulations surpassed the CTRL. However, these gains in skill were relatively small, with less than a 0.1 m s^{-1} reduction in MAE and a 0.1–0.4 m s^{-1} smaller average bias.

The discrepancy between network average and individual station wind speeds creates uncertainty about the general skill of the WRF model. As previously noted, this systematic overprediction could have been the result of inappropriately assigned surface roughness, unresolved sheltering, model physics error, or some combination of the three. It is less likely that model physics error was the source of error, though, since each configuration produced similar positive biases.

Recall that the majority of RAWS stations used in our verification were on steep slopes and topographic peaks (e.g., Figure 1), and poor resolution of complex terrain features in the model can affect forecasts. Figure 15 shows the topography of d03 for this case study and the RAWS stations within, color coded by the average forecast bias for each station from the CTRL simulation. Note that stations located at high elevations or along steep gradients have larger positive biases than the few RAWS stations located at lower and flatter elevations.

Also shown in Figure 15 is the relationship between the actual station observation minus model-prescribed elevation to average bias. The overall representativeness of the d03 terrain was ambiguous, with the model placing station location elevations both higher and lower than their actual elevations. Each station fell within one of three groupings:

1. Positive elevation difference and positive wind speed bias
2. Negative elevation difference and negative wind speed bias
3. Negative elevation difference and positive wind speed bias

When elevation difference and wind speed bias were positively correlated (group 1), the incorrect terrain elevation settings placed the station location higher in the atmosphere where winds tend to be faster. Alternately, when elevation difference and wind speed bias exhibited a negative correlation (group 2), the WRF model terrain positioned the station lower in the atmosphere where winds tend to be slower. For group 3, we hypothesized the errors may have been due to inappropriate surface-roughness assignments (i.e., land use and vegetation characterization at these locations may have been inaccurate, causing errors in modeled surface drag on the winds).

According to the US Department of Agriculture and the US Forest Service, chaparral shrublands (i.e., a mix of summer-drought-tolerant shrubs and heathland plants) cover much of the Arizona landscape (Nichol 1952; Lowe 1964; Pase and Brown 1982). However, vegetation classifications at elevations above 2000 m in the region are usually evergreen needleleaf or mixed forests, which create markedly different surface drag effects than shrubs.

Figure 15 includes a histogram of prescribed land-use-type occurrence at each of the RAWS stations in d03. Because of the large number of stations classified as shrubland (including both "open-" and "closed-" shrubland categories), we conducted a brief test to see if increasing the roughness at locations with RAWS stations situated above 2000 m from the open- and closed-shrubland roughness settings (z_0 = 0.06 m and z_0 = 0.05 m, respectively) to that of the forest classifications (z_0 = 0.5 m) alleviated the bias. We performed this assessment using a diagnostic detailed by Wieringa (1980):

$$U_{h_{z_{0\mathrm{cor}}}} = U_{\mathrm{WRF}}\left(\left[\frac{\ln\left({}^{h_{\mathrm{f}}}/_{z_{0\mathrm{WRF}}}\right)}{\ln\left({}^{h_{\mathrm{WRF}}}/_{z_{0\mathrm{WRF}}}\right)}\right] * \left[\frac{\ln\left({}^{h_{\mathrm{R}}}/_{z_{0\mathrm{cor}}}\right)}{\ln\left({}^{h_{\mathrm{f}}}/_{z_{0\mathrm{cor}}}\right)}\right]\right), \quad (4)$$

where

h_{WRF} = the height AGL of the simulated wind speed (10 m);
U_{WRF} = the simulated 10 m wind speed;
h_{f} = 60 m AGL, a height at which we assume minimal surface influences (i.e., the transition between the "near-surface" layer and the remainder of the PBL);
$z_{0\mathrm{WRF}}$ = the WRF-prescribed surface roughness;
h_{R} = the height AGL of the RAWS observation;

$z_{0\mathrm{cor}}$ = the artificially prescribed forest surface roughness (0.5 m); and

$U_{h_{z_{0\mathrm{cor}}}}$ = the final forecasted wind speed adjusted for the new surface roughness and height.

Figure 15. WRF d03 topography (*shaded*) and RAWS station locations, color coded by the average forecast wind speed bias at each station from the CTRL simulation during the 4 July 2014 dust event (*A*). Average bias of the CTRL forecast vs. the difference between the model elevation and actual observation elevation (model minus observed) for each RAWS station (*B*). Histogram of RAWS station land-use index, 1 = Evergreen Needleleaf Forest, 5 = Mixed Forests, 6 = Closed Shrubland, 7 = Open Shrubland, 10 = Grasslands, and 13 = Urban/Built Up (*C*).

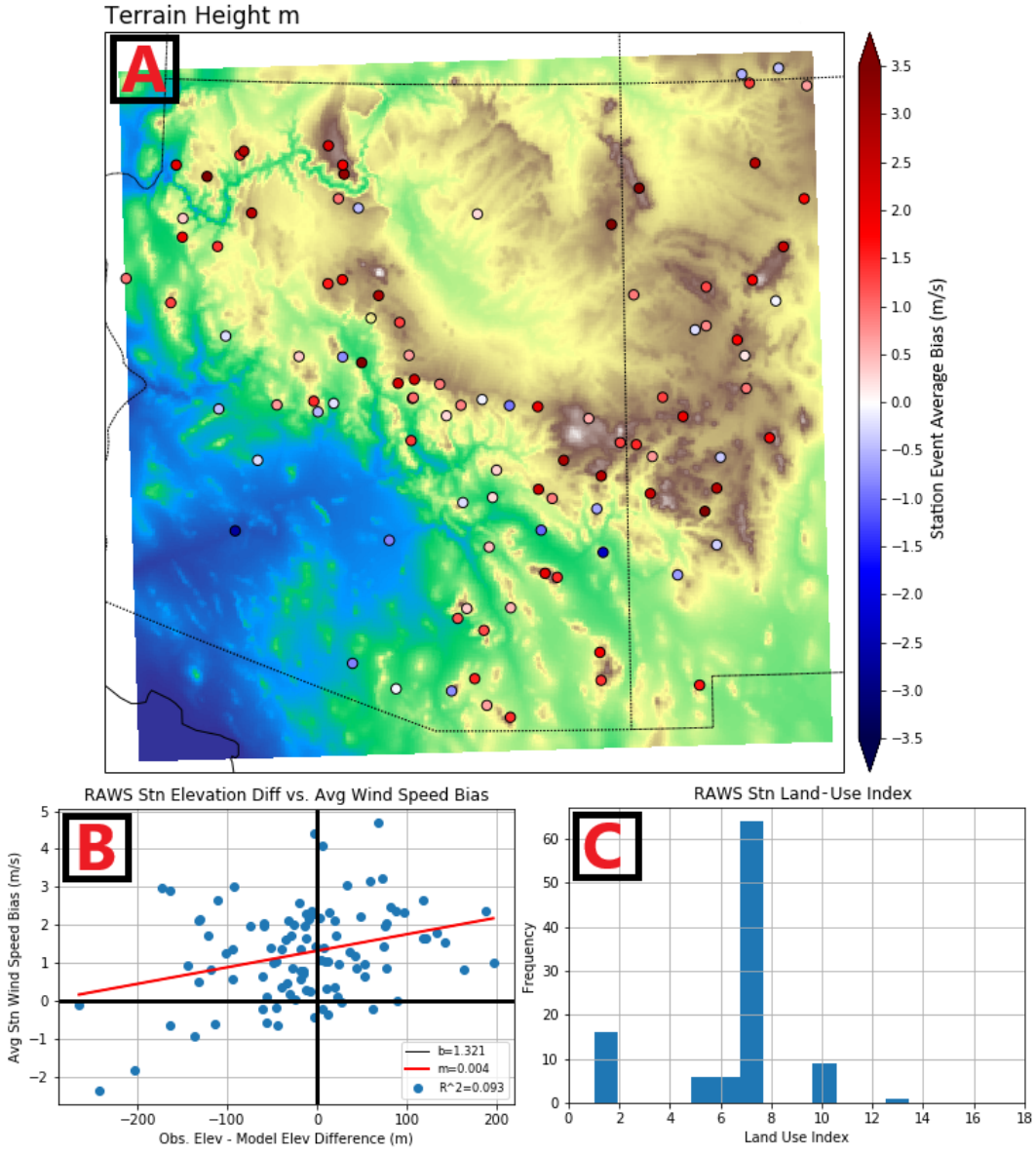

There were 102 RAWS stations within d03, of which 52 resided above 2000 m and 33 were classified as open shrubland or closed shrubland. Figure 16 shows a time series of wind speeds averaged over the network with and without the roughness adjustment. Overall, the roughness modification helped mitigate the systematic overprediction, reducing the average bias from +1.19 m s^{-1} to +1.05 m s^{-1} and the network average bias during the peak of the event from +2.2 m s^{-1} to +1.7 m s^{-1} (closer to that of the ASOS network average), but did not eliminate it, leaving observation sheltering as a potential cause. However, given the scope of this paper and the relatively skillful prediction of winds near lower-elevation dust sources, we chose not to investigate the cause of the error further. Subsequent verification of RAWS network average and individual station wind speed in this report used the equation (4) surface-roughness adjustment at high elevation stations (>2000 m) instead of that from equation (1).

Figure 16. Time series of observations (*black*), base forecasts (*red*), and surface-roughness-adjusted forecasts (*purple*) of surface wind speed (6.1 m) averaged over the RAWS network. The surface-roughness adjustment uses a static z_0 = 0.5 m for stations with an elevation above 2000 m.

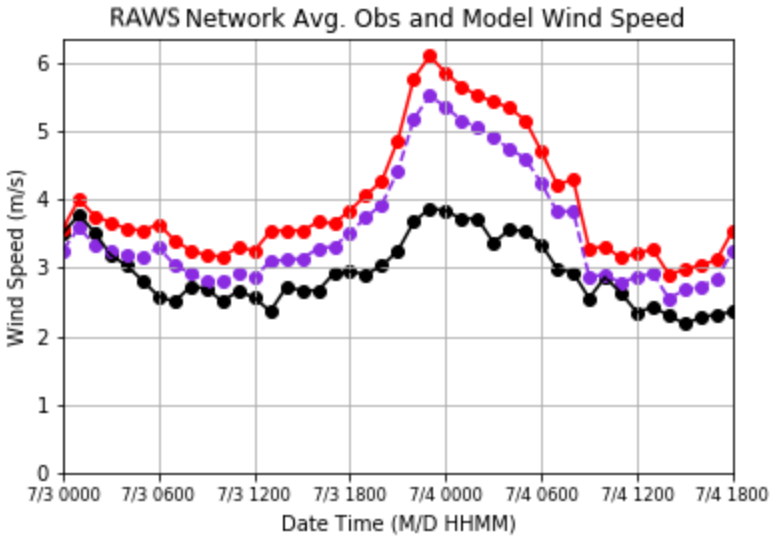

Aside from the wind speed overprediction issues at RAWS station sites, our sensitivity analysis showed that the event's overall evolution and structure were largely independent of model physics selection. Changes in configuration had more influence on the smaller-scale details like convective intensity, peak wind speeds, and timing of passage over individual locations.

For the NoahMP configuration in particular, its relative gain in skill relative to CTRL was primarily due to its retention and use of larger surface-

roughness values for all stations. Both Noah and NoahMP initialize with the same prescribed surface roughness; but after the first model time step, Noah lowered the surface roughness while NoahMP continued to use the initial or larger values (e.g., Figure 17).

Figure 17. Histograms of the prescribed surface roughness at RAWS stations by the Noah (*blue bars*) and NoahMP (*red bars*) LSMs at the initialization time (*A*) and 2 hr into the forecast (*B*), binned every 0.1 m. *Purple* shaded areas indicate overlap between the two LSMs.

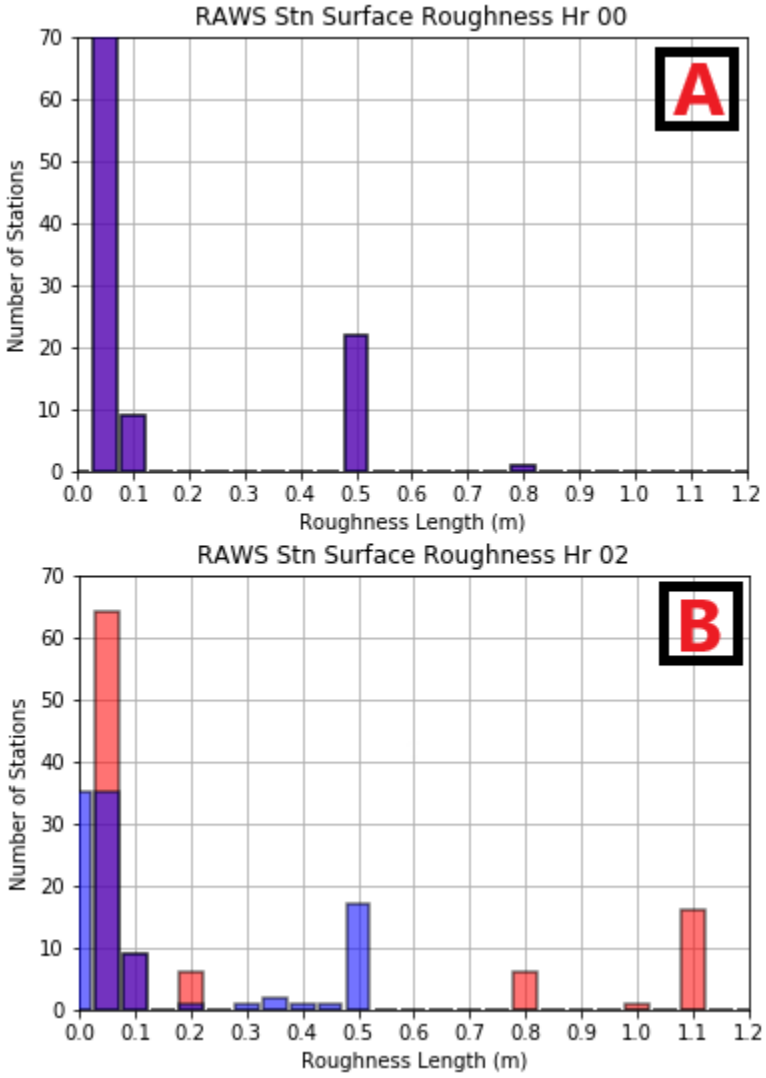

This is rather common for LSMs, many of which, including Noah and NoahMP, take an initial roughness-length value from a lookup table and make modifications to it as the simulation progresses. These two LSMs diverge in their values of prescribed roughness length due to the offset in the seasonal cycles coded into each scheme (Cao and Fovell 2018) The higher-magnitude surface-roughness values helped reduce positive wind speed

bias and error throughout the forecast period but had a larger influence in terms of percentage change during the preconvection and postconvection periods when winds were much calmer.

Overall, we chose to continue using the CTRL configuration for the remaining four case study analyses. From a synoptic perspective, we noted little change in the overall synoptic performance compared to other configurations. Furthermore, we determined the CTRL to have sufficient skill in simulating the convective structure, evolution, and resulting winds. The NoahMP configuration did provide some improvement; however, the observed gains were minor. Ultimately, we chose to continue using the original Noah LSM in our model setup because of its broader use in the modeling community.

3.2 21 August 2014 case study

3.2.1 21 August 2014 event overview

The second case study selected for analysis took place on 21 August 2014 along the border of California and Arizona. Because of its geographic location and occurrence in the latter half of summer, this dust event is unique compared to the other selected events, differing in both its synoptic setup and resulting convective activity. Figure 18 shows the evolution of the SPCHMA 500 hPa analysis from 1200 UTC, 21 August, through 0600 UTC, 22 August. At 1200 UTC, the 500 hPa pattern shows a weak amplitude trough/ridge/trough pattern with features centered over the Great Basin, Mississippi River Valley, and the continental East Coast near Chesapeake Bay, respectively. Additionally, there was a weak cutoff (i.e., isolated) low pressure to the west of the southern California coast. This pattern provided strong southwesterly flow over the Gulf of California that shifted to southerly flow inland along the California-Arizona border and into Arizona. As time progressed, this pattern gradually moved east, and the cutoff low pressure began to contract in size. As the pressure center shrank, the wind accelerated briefly on the south side of the low-pressure center, creating a jet streak. This area of strong, upper-level winds entered the southwest region of Arizona by 2100 UTC, 21 August, 1 hr before peak convective activity. The positioning of the jet streak south of the Mexican border and the progression of the low pressure farther east promoted stronger upward vertical motion and convective activity over the border between California and Arizona. By the end of the event at 0300 UTC, 22

August, the low-pressure system weakened, and the associated jet streak disappeared at the 500 hPa level.

Figure 18. SPCHMA of 500 hPa height (*contoured*) and wind (*barbs* and *shaded*) valid at 1200 UTC, 21 August 2014 (*A*); 2100 UTC, 21 August 2014 (*B*); and 0300 UTC, 22 August 2014 (*C*).

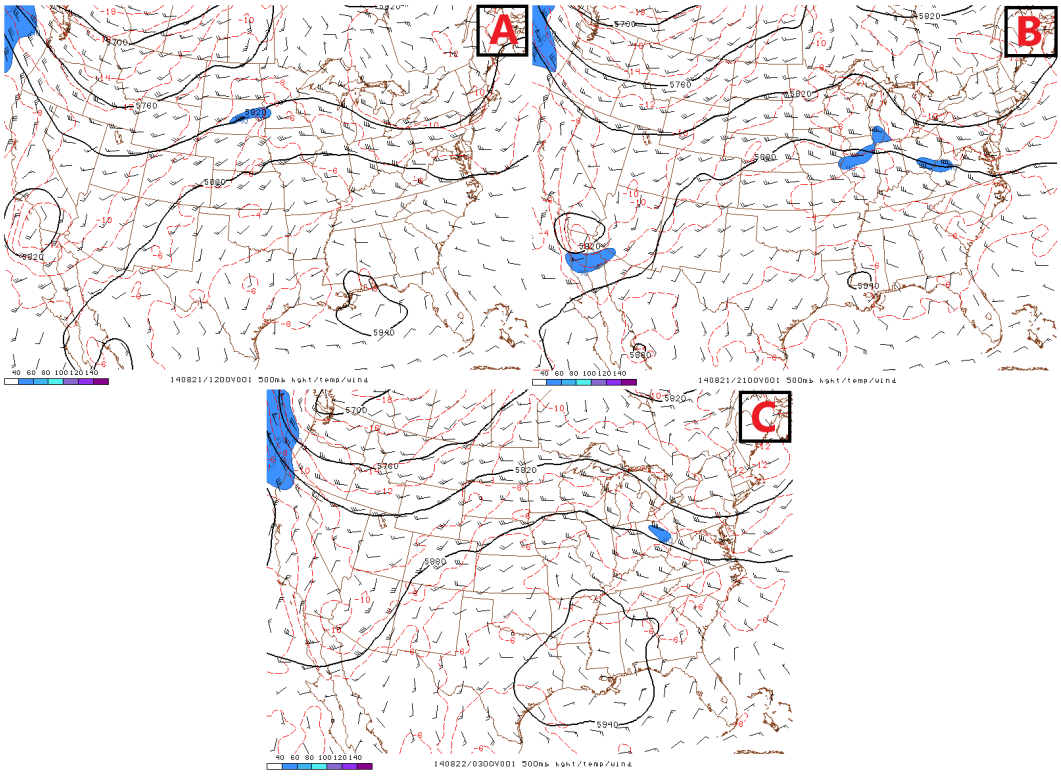

Because the dust event occurred well west of central Arizona, the Gulf of California was likely the primary source of atmospheric moisture. The SPCHMA 850 hPa analysis throughout the event (Figure 19) supports the Gulf of California as the dominant moisture source. Before convection formed (1200 UTC, 21 August), weak southerly and southeasterly winds came out of the Gulf of California, turning southwesterly on entry into southeast California and southwest Arizona. During the buildup to the event, these southerly winds strengthened to about 10 kn (5.14 m s^{-1}), feeding more moisture into southern California and Arizona. By 1800 UTC, 21 August, winds over southern California and Yuma shifted more southeasterly. This wind shift allowed more moisture transport inland and pushed it farther west, favoring convective formation over southern California instead of central Arizona.

Figure 19. SPCHMA of 850 hPa height (*contoured black*), wind (*barbs*), and dew point (*shaded*, Celsius) valid at 1200 UTC, 21 August 2014 (*A*); 1800 UTC, 21 August 2014 (*B*); 0000 UTC, 22 August 2014 (*C*); and 0600 UTC, 22 August 2014 (*D*).

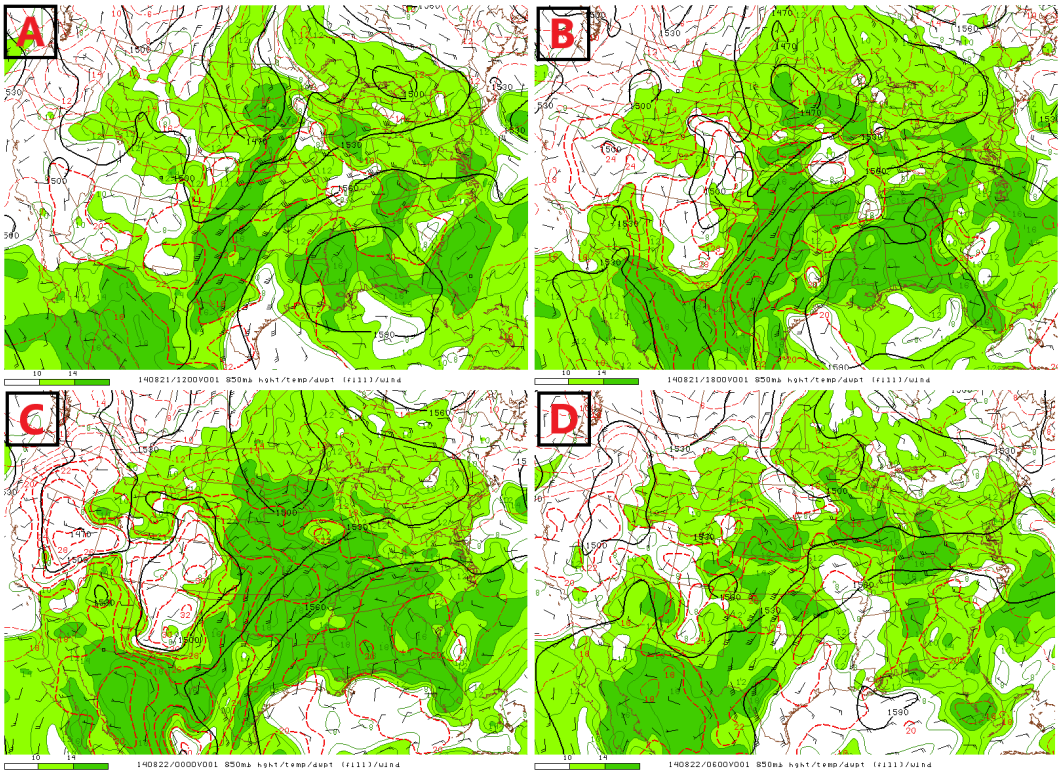

Figure 20 shows the evolution of the convection throughout the event through NEXRAD radar composite imagery. Thunderstorms began forming just before 1600 UTC, 21 August, and coalesced into a small cluster just west of the Mojave Valley. Two hours later, at 1800 UTC, this cluster traversed northward and joined with a weak collection of small thunderstorms moving northwest out of Arizona, pushing into southern Nevada. At the same time, thunderstorms began to form along the Peninsular Range, marking the onset of the main convective event. These thunderstorms continued to intensify with time, forming a line of convection along the ridgeline while convection reformed and rapidly reintensified west of the Mojave Valley. All developing convection slowly rotated counterclockwise around the surface low pressure located over the borders between California, Arizona, and Nevada (referred to as the “triple point”). The thunderstorms along the Peninsular Range then quickly intensified as they merged into a QLCS and moved rapidly downslope and over the area southeast of the Salton Sea. At 2200 UTC, the peak of the event, the QLCS continued to move swiftly northeast as convective cells that had formed near the triple point moved south on a collision course. Shortly after, these systems collided, forming a convective line arcing from the California

badlands near Landers to southwest Arizona and continued to move eastward, rotating slightly counterclockwise as it traveled. The convective activity mostly ceased by 0100 UTC, 22 August, with only weak remnant clusters of cells continuing to move more progressively eastward as they traversed deeper into central Arizona.

Figure 20. NEXRAD radar composite imagery for the 21 August 2014 case for 1600 UTC, 21 August 2014 (*A*); 1800 UTC, 21 August 2014 (*B*); 2000 UTC, 21 August 2014 (*C*); 2200 UTC, 21 August 2014 (*D*); 0000 UTC, 22 August 2014 (*E*); 0200 UTC, 22 August 2014 (*F*); and 0400 UTC, 22 August 2014 (*G*).

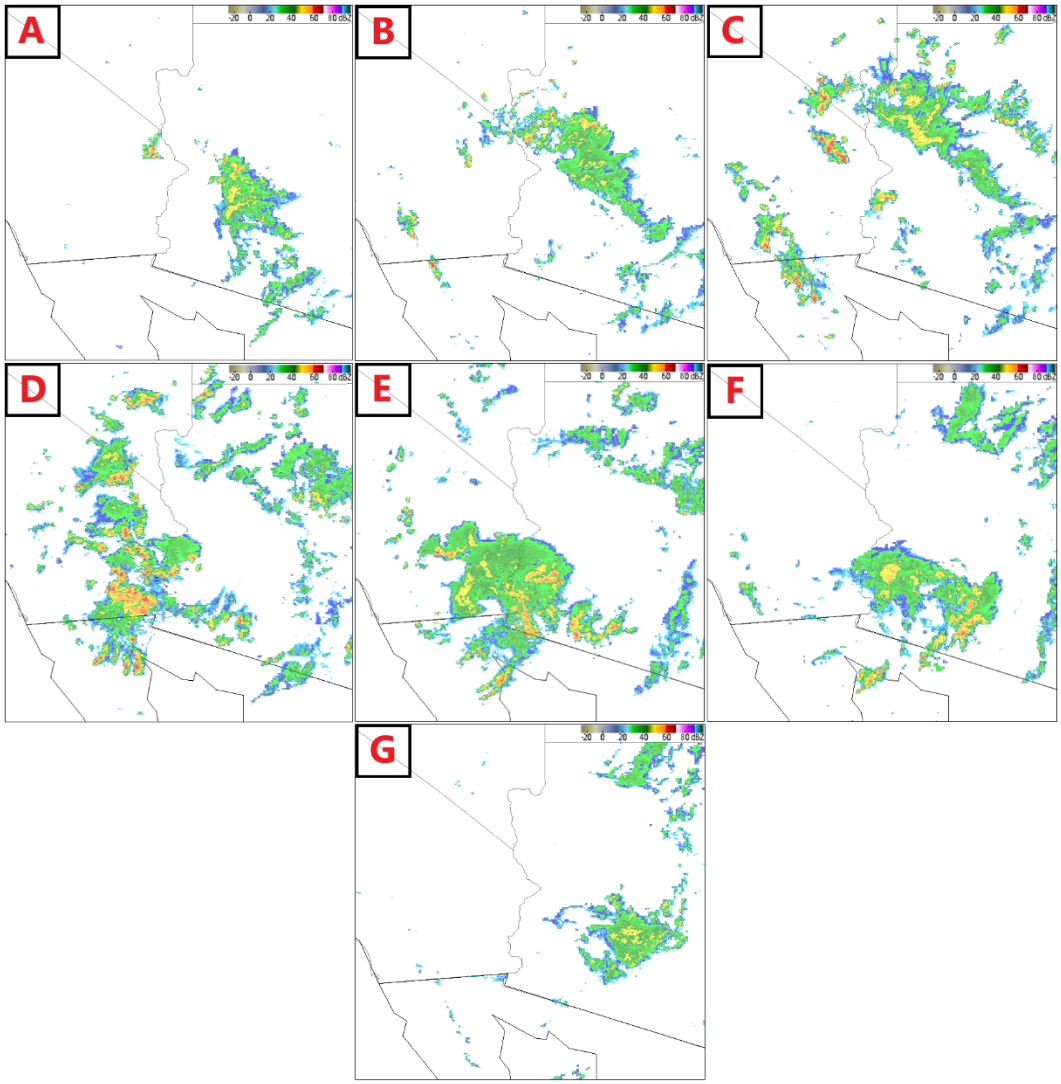

3.2.2 21 August 2014 simulation results

We compared the SPCHMA and WRF-simulated 500 hPa synoptic patterns (Figure 21) and found that our simulation effectively reproduced the synoptic conditions from the analysis product. The WRF simulation

properly forecasted placement of the trough and ridge pattern centered over the Great Basin and Mississippi River Valley, respectively, as well as the cutoff low-pressure system over southwest California. Our simulation also captured the gradual weakening of the cutoff low-pressure center with time and the resulting change in wind direction over the California-Arizona border. The one aspect of the synoptic flow that our simulation did not fully recreate was the landfalling jet streak in southwest Arizona. WRF was able to forecast the appearance of the jet streak and its maximum intensity of 40 kn (25.6 m s^{-1}) at 2100 UTC, 21 August, providing forcing for upward vertical motion. However, the simulation maintained the jet-streak intensity 6 hr later, diverging from the SPCMHA version, which weakened the jet-streak maximum to 35 kn (15.4 m s^{-1}). Despite this deviation, we deemed our simulation as relatively skillful since it reproduced realistic synoptic conditions and generated an appropriate magnitude of upper-level forcing at the peak of the event.

With regard to low-level atmospheric flow, our simulation was able to reproduce the SPCHMA flow pattern at 850 hPa throughout the event quite skillfully (Figure 22), capturing the broad, clockwise circulation over the panhandle of Florida. This circulation feature effectively cut off the Gulf of Mexico as a potential moisture source due to the strong southerly and southwesterly winds along the southern coast. Additionally, our simulation forecasted the wind evolution over the Gulf of California and along the California-Arizona border. The forecasted wind pattern started as weak southerly at 1200 UTC, 21 August, and developed into a weak counter-clockwise rotation, spanning from the Baja Peninsula to the triple-point area. However, the forecasted southerly winds were initially too strong (approximately 10 kn [5.14 m s^{-1}]) compared to the SPCHMA analysis (5 kn [2.57 m s^{-1}]), which resulted in higher dew-point temperatures (i.e., more moisture) in the southwest half of Arizona.

At 1200 UTC, 21 August, the SPCHMA dew-point temperatures were less than 10°C over much of Arizona, whereas our simulation forecasted dew-point temperatures of 12°C–14°C over southern Arizona. We also saw this difference in available moisture in terms of PWAT (Figure 23). At this time, the predicted PWAT pattern matched the SPCHMA well, displaying lower moisture available along the mountains of southern California and the Baja Peninsula. Our simulation also reproduced the sharp gradient along the west coast of Mexico, but it formed an additional pocket of higher PWAT (1.57–1.97 in.) over southern Arizona that was not present in

the analysis. This additional moisture pocket may have led to increased convective activity early in the event; but otherwise, our simulation showed skill in reproducing the pattern of the lower atmosphere.

Figure 21. SPCHMA (*panels A–C*) and WRF CTRL d01 forecasts (*panels D–F*) of 500 hPa height (*contoured*) and wind (*barbs* and *shaded*) valid at 1200 UTC, 21 August 2014 (*A*, *D*); 2100 UTC, 21 August 2014 (*B*, *E*); and 0300 UTC, 22 August 2014 (*C*, *F*).

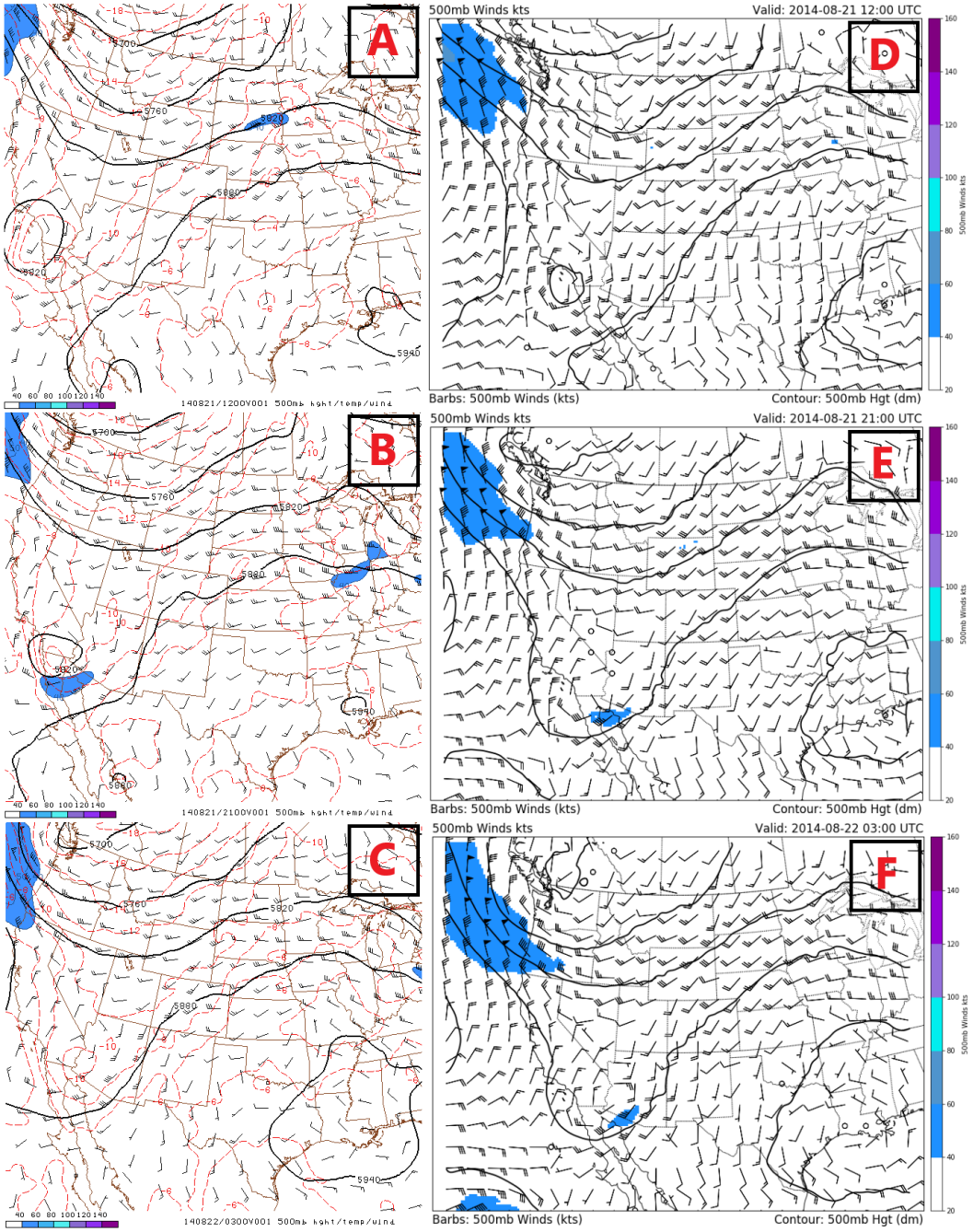

Figure 22. SPCHMA (*panels A–C*) and WRF CTRL d01 forecasts (*panels D–F*) of 850 hPa height (*contoured black*), wind (*barbs*), and dew point (*shaded*, Celsius) valid at 1200 UTC, 21 August 2014 (*A*, *D*); 1800 UTC, 21 August 2014 (*B*, *E*); and 0000 UTC, 22 August 2014 (*C*, *F*).

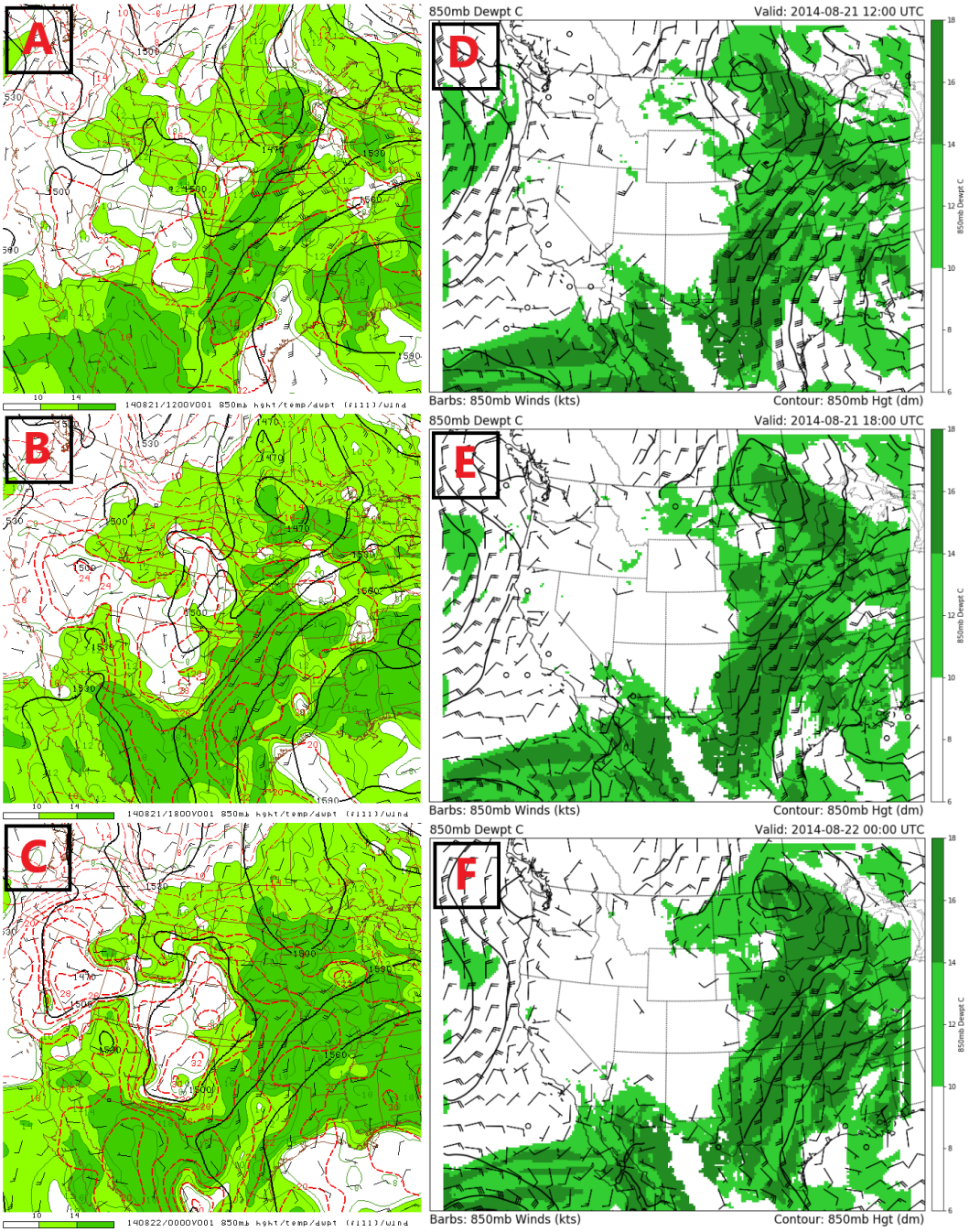

Figure 23. SPCHMA (*panels A–C*) and WRF CTRL d02 forecasts (*panels B–F*) of column-integrated precipitable water (under 400 hPa, *shaded* and *contoured* in inches) valid at 1200 UTC, 21 August 2014 (*A*, *D*); 1800 UTC, 21 August 2014 (*B*, *E*); and 0000 UTC, 22 August 2014 (*C*, *F*). Contours are every 0.1 in.

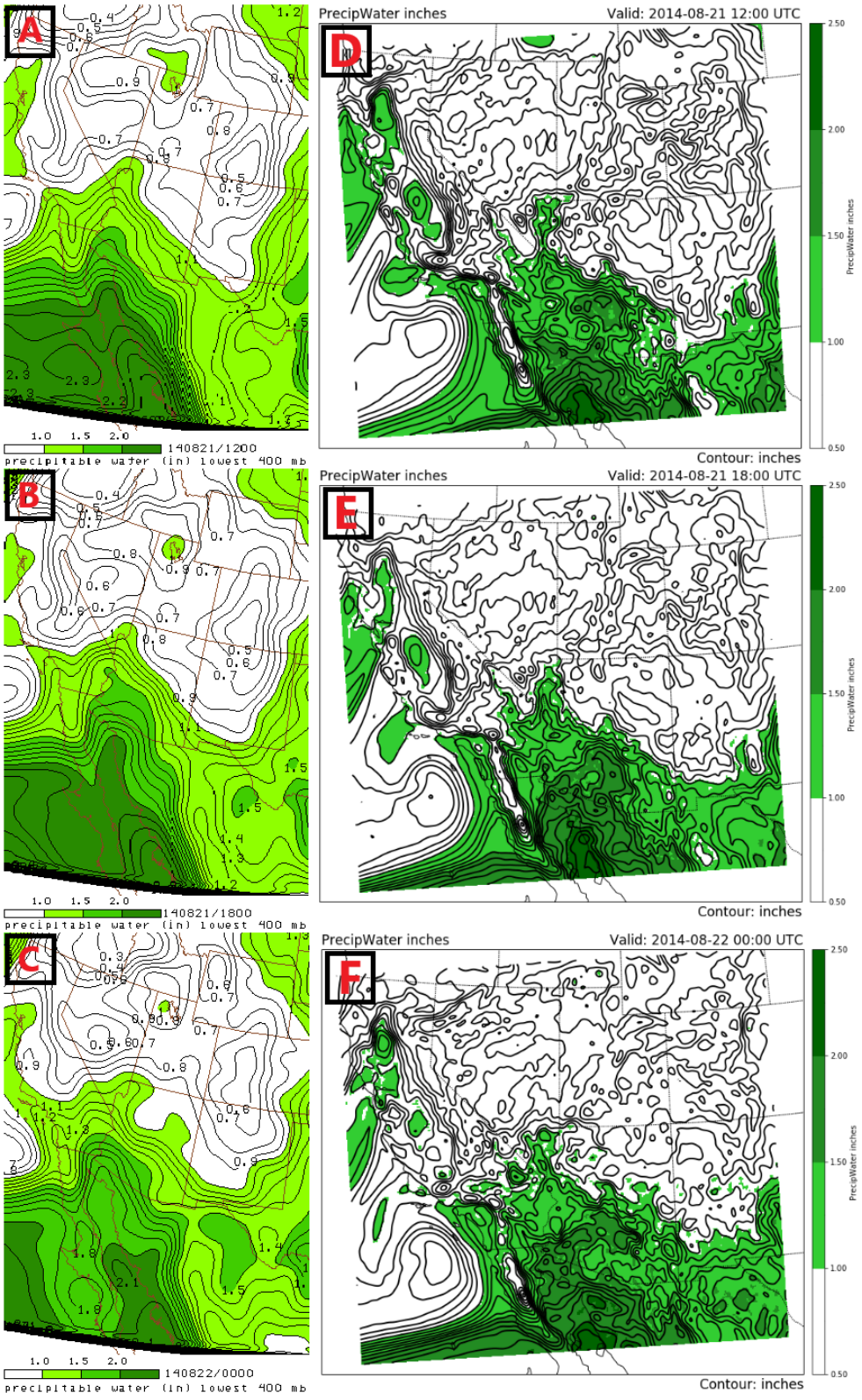

Figure 24 shows the radar reflectivity comparisons for the event. By 1600 UTC, 21 August, shortly after convection initiated, appreciable differences between the observed and forecasted radar conditions were already present. The initial cell generated by the simulation traveled north into southern Nevada and was much more robust than the cell observed by NEXRAD. Furthermore, the simulated northwest–southeast convection over Arizona was much weaker, only starting to initiate. Over the next 4 hr, this deviation proved to be problematic for the development of convection associated with this event's peak. By 2000 UTC, 21 August, the more intense simulated cell that moved into Nevada had mostly collapsed. This change generated a strong outflow, especially to the southwest in eastern California, which helped trigger convection over the California badlands northeast of the Salton Sea. Our simulation's resultant environmental conditions caused the secondary cell near the Salton Sea to produce an outflow boundary and easterly winds on the east side of Peninsular Range, which limited the convective growth along the range from westerly cross flow and reduced moisture availability in the lee of the mountains. This unobserved cell may have been related to the smaller, intense convective cell in the observed radar closer to the California-Nevada border, potentially pushed farther southwest by the intense outflow of the initial northern cell.

At 2200 UTC, 21 August, the peak of the event, our simulated radar reflectivity was considerably different from the observed radar composites. Both incorporated a convective cluster with an embedded QLCS near the California-Arizona border but differed in terms of the QLCS placement and orientation. In the composite radar image, the QLCS line was on the west side of the border with a northwest–southeast orientation. The position of the QLCS in our simulation, however, was east of the California-Arizona border with a southwest–northeast orientation. This difference was likely due to the halting of the convection along the Peninsular Range. By preventing downslope propagation, the simulated convection developed into a QLCS farther east along the boundary between the secondary cell's outflow and the southerly flow from the Gulf of California.

Figure 24. Observed NEXRAD radar (*panels A–F*) and WRF CTRL d03 simulated 1 km AGL radar (*panels a–f*) for 1600 UTC, 21 August 2014 (*A*, *a*); 1800 UTC, 21 August 2014 (*B*, *b*); 2000 UTC, 21 August 2014 (*C*, *c*); 2200 UTC, 21 August 2014 (*D* and *d*); 0000 UTC, 22 August 2014 (*E* and *e*); and 0200 UTC, 22 August 2014 (*F* and *f*).

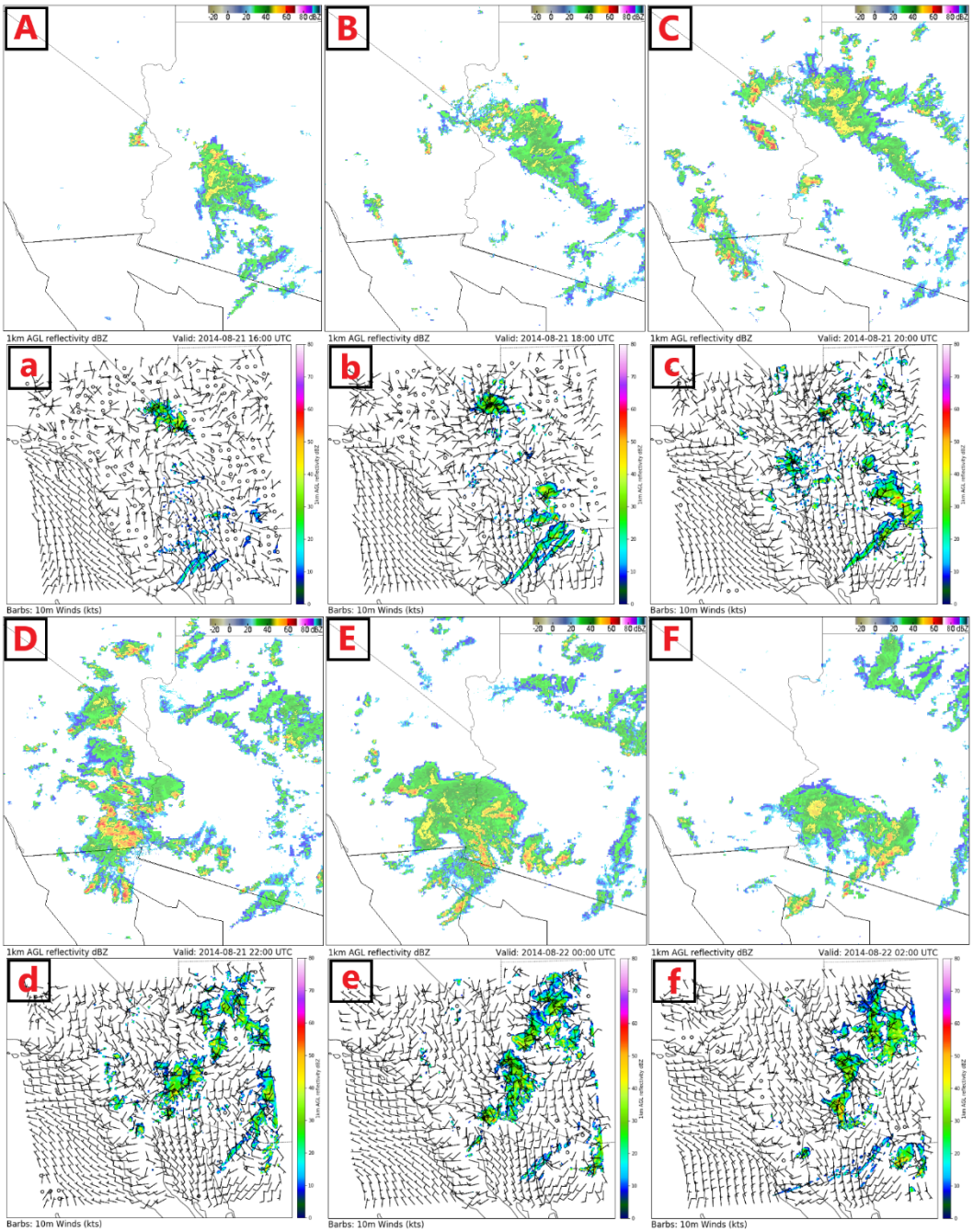

As the event continued, the forecasted reflectivity aligned better with observations. The simulation reproduced the transition of the convective mode from a straight line QLCS to a more extensive curved convective line; however, the simulated values appeared to be more progressive due to the shift in initiation. Comparison of the 0000 UTC forecasted and

0200 UTC observed radar on 22 August revealed many similarities, including the "comma head" northern end of the convective line, trailing convection farther south just north of the Gulf of California, and weaker convective lines in southeastern and northern Arizona. Overall, our simulation favored the correct convective mode and progression; however, overly intense initial preceding convection that led to a shift of convective initiation offset the accuracy.

We verified the resulting surface wind speeds with ASOS observations (Figure 25). The forecast followed a similar pattern to the observed network average wind speed but differed in several aspects. For example, the forecast exhibited a peak in wind speeds before the onset of the event between 0500 and 1000 UTC, increased wind speeds 2 hr earlier than observations (1500 UTC instead of 1700 UTC), and overforecasted the network peak by 0.5 m s^{-1}. Collectively, these differences contributed to the event average bias of +1.205 m s^{-1} for the ASOS network.

We also verified surface wind forecasts at three ASOS stations along the California-Arizona border, including KEED, KBLH, and KNYL, and one station in southern California, KIPL. At the northernmost station, KEED, our simulation missed the first peak in surface wind speed between 1500 and 2000 UTC, 21 August, but successfully predicted the intensity of the secondary peak of 11.5 m s^{-1}, albeit an hour early at 0100 UTC, 22 August. This pattern was consistent with the underdeveloped northwest–southeast convection that spanned Arizona during the hours building up to the event. Farther south, our simulation completely missed the very sharp peak in wind speed (22 m s^{-1}) at KBLH due to the shift in convective initiation farther east. Aside from this error, the model captured the evolution of wind speed outside of the peak (2000–2300 UTC, 21 August) at this location incredibly well. The initial ramp-up of wind speeds at KNYL between 1500 and 2000 UTC was consistent with an increase in southerly winds ahead of convective passage, though the simulation developed the convective line too far north and east. This caused the simulation to ramp up wind speeds at 2000 UTC, 21 August, miss the peak in wind speed from the outflow of the primary convection, but still capture the weaker local peak in wind speed at 0100 UTC, 22 August, from the convective line that trailed farther south as overall winds died down. Lastly, at KIPL, the wind pattern struggled to match observations, especially during the 16 m s^{-1} peak winds at 2100 UTC, 21 August. At this time, observed winds were

westerly and downslope, reaching KIPL before convection from the Peninsular Range passes. The passage of a secondary gust front from convection on the backside of the leading convective edge produced a secondary peak in wind speed of 10 m s^{-1} that our simulation predicted well. Despite this decent agreement, the secondary peak originates from disparate convective cells in the observations and simulations. Overall, the issues with convection initiation caused the model to miss observed peaks in wind speed. However, the peak winds generated by the simulation were of similar intensity and timing, though more so for observed secondary peaks than primary spikes in wind speed.

Figure 25. Time series of observed (*black*) and modeled (*red*) surface (10 m) wind speed during the 21 August 2014 dust storm for the network average of all ASOS stations (*A*), KEED (*B*), KBLH (*C*), KNYL (*D*), and KIPL (*E*). The *gray line* in the network average shows the number of stations used in the network average. The 1 min observations are supplemented by METARS at individual stations when needed and are denoted by *dots*.

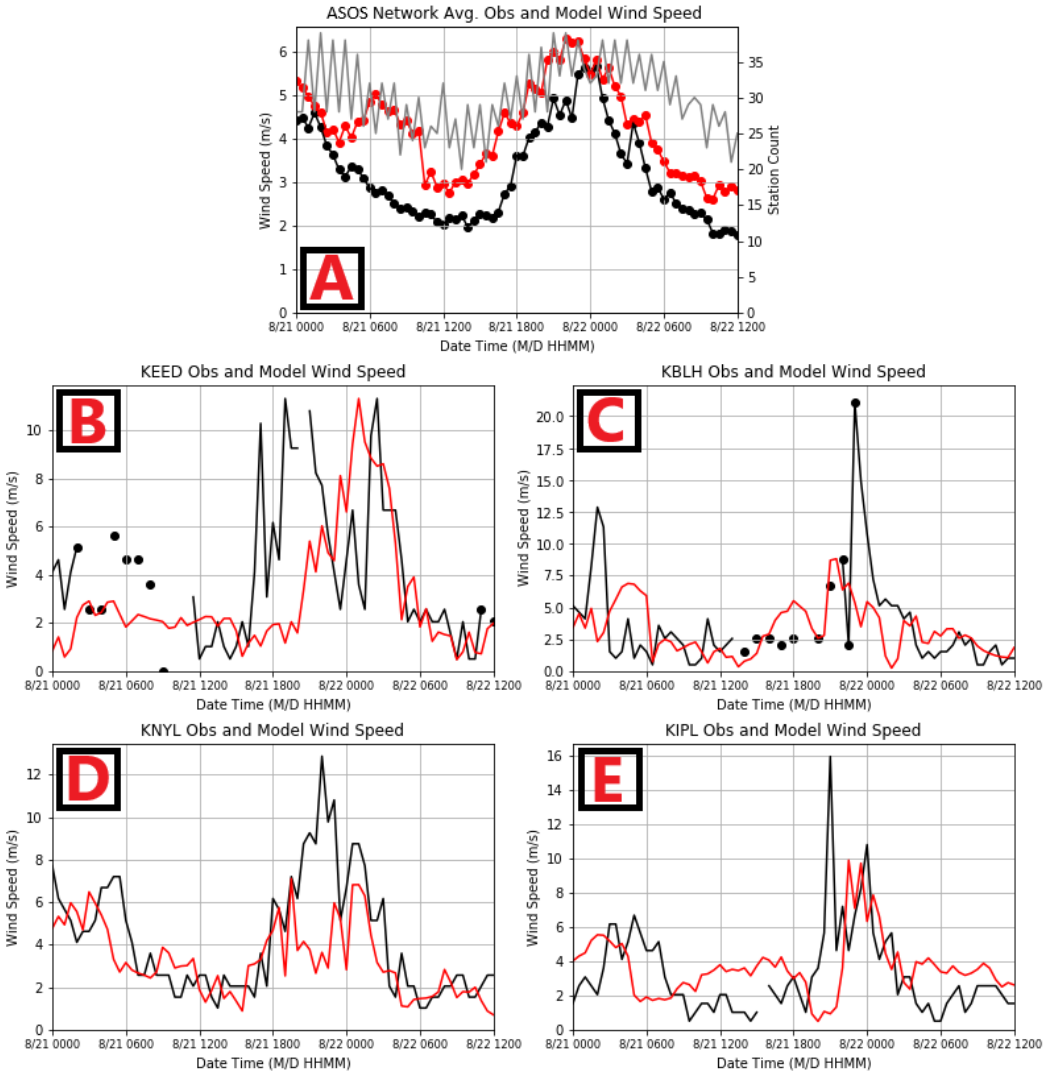

Figure 26 compares simulated and observed wind speeds at RAWS station locations. Similar to our findings with the ASOS observations, forecasts of RAWS network average wind speed exhibited a pre-event peak between 0500 and 1000 UTC on 21 August that was not present in the observations. We also noted that the simulation overpredicted network average peak winds by approximately 1 m s^{-1}, as is typical of RAWS. What was highly unusual was the event average RAWS network bias of +0.967 m s^{-1}, making this the only one of the five case studies where the model average bias was smaller verified against RAWS stations than ASOS.

We compared wind forecasts and observations at four RAWS stations near the California-Arizona border, including QUPA3, AKPA3, CBRA3, and QAC1. The northernmost station, QUPA3, just east of the Arizona-Nevada border, showed a substantial overestimation and late arrival of simulated surface wind speeds due to the exuberant initial northern cell collapse and outflow from the event peak convection that displaced farther north than observed. At AKPA3, the observed peak winds coincided with the outflow from a cell ahead of the peak QLCS. However, the forecasted wind peak was associated with the outflow from the displaced QLCS wake, resulting in a delayed arrival of peak winds and persistence of high winds at the location for the remainder of the simulation. Farther south, CBRA3 highlighted how differences in convective initiation affected the number of wind peaks at a location. Observed values indicated only one peak in wind speed, at 2300 UTC, 21 August, corresponding to the passage of the northwest–southeast QLCS. The simulation, however, forecasted two peaks in wind speed, one associated with the outflows from the secondary displaced cell over the California badlands and the other with the peak of the displaced QLCS. We observed a very similar pattern at QCAC1, except the observed peak occurred after both forecasted peaks instead of between. This disagreement was due to convection on the backside of the peak QLCS delaying and constraining the spread of strong outflow winds in the wake. As a whole, the individual RAWS station comparison demonstrated problems in the timing of strong winds due to the simulated convective initiation shift, which produced early, late, and multiple peaks in wind speed.

Figure 26. Similar to Fig. 25 except for the average of all RAWS stations (*A*), QUPA3 (*B*), AKPA3 (*C*), CBRA3 (*D*), QCAC3 (*E*) surface (6.1 m) wind speed. *Dots* are used for individual stations since data is reported only once every hour with no specific reporting time.

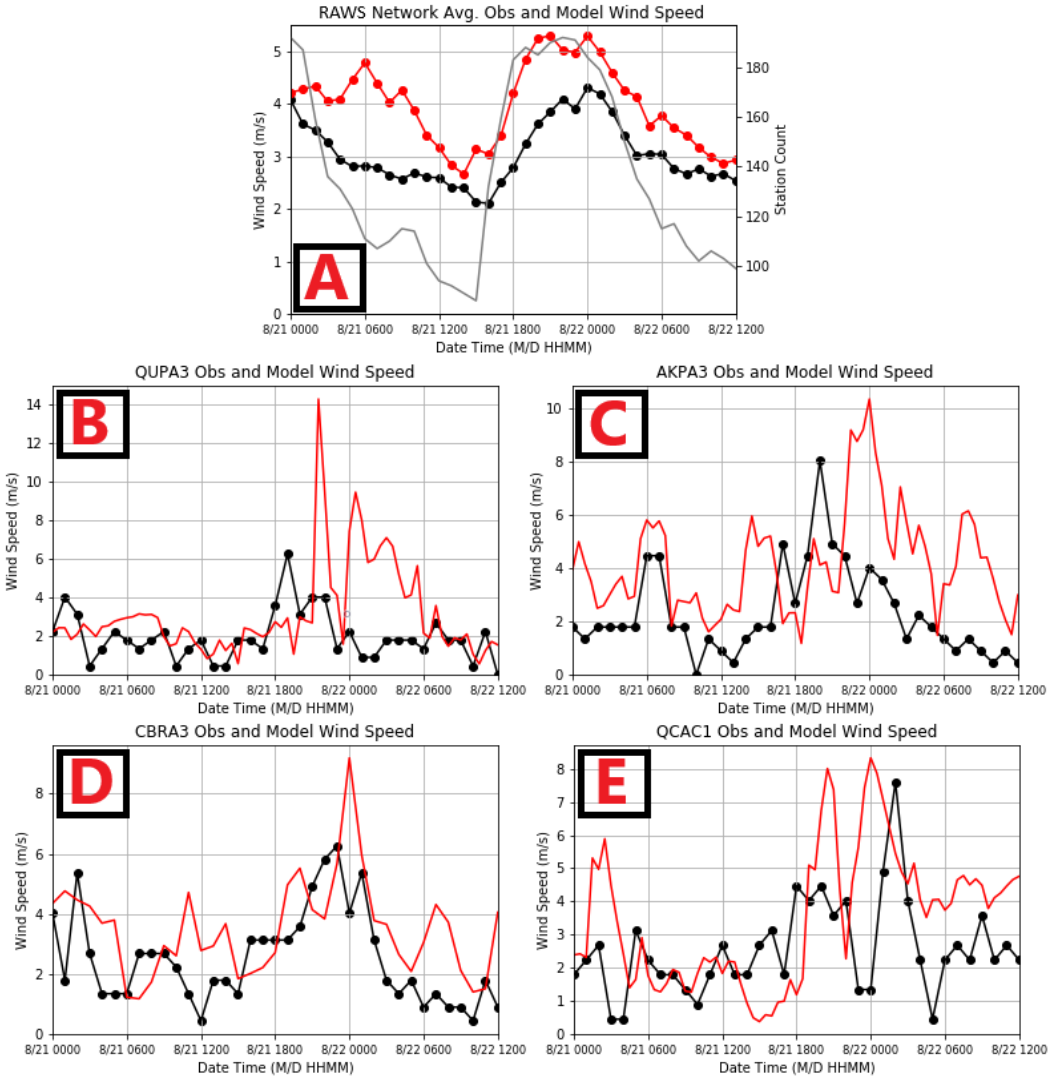

3.3 28 June 2015 case study

3.3.1 28 June 2015 event overview

The third selected dust-event case took place on 28 June 2015 over the central Arizona region, affecting the area in and around Phoenix. Convection during this event initiated around 1800 UTC, 27 June, peaked at 0000 UTC, 28 June, and concluded by 0500 UTC, 28 June. Figure 27 shows the SPCHMA 500 hPa analysis at preconvection (1200 UTC, 27 June) and peak convection times. The synoptic conditions of this event included a largely stationary, highly amplified trough/ridge pattern similar to the setup we observed in the 4 July 2014 case (see section 3.1) but with

higher pressure underneath the ridge centered over the Great Basin area instead of the Four Corners region. Initially, at 1200 UTC, 27 June, the flow pattern produced easterly and northeasterly winds over the entirety of Arizona. As conditions evolved, the high pressure broadened and migrated slightly north, causing the winds over the northern half of Arizona to shift to northeasterly.

Figure 27. SPCHMA of 500 hPa height (*contoured*) and wind (*barbs* and *shaded*) (*panels A* and *B*) and 850 hPa height (*contoured*), wind (*barbs*), and dew point (*shaded*) (*panels C* and *D*) valid at 1200 UTC, 27 June 2015 (*A*, *C*), and 0000 UTC, 28 June 2015 (*B*, *D*).

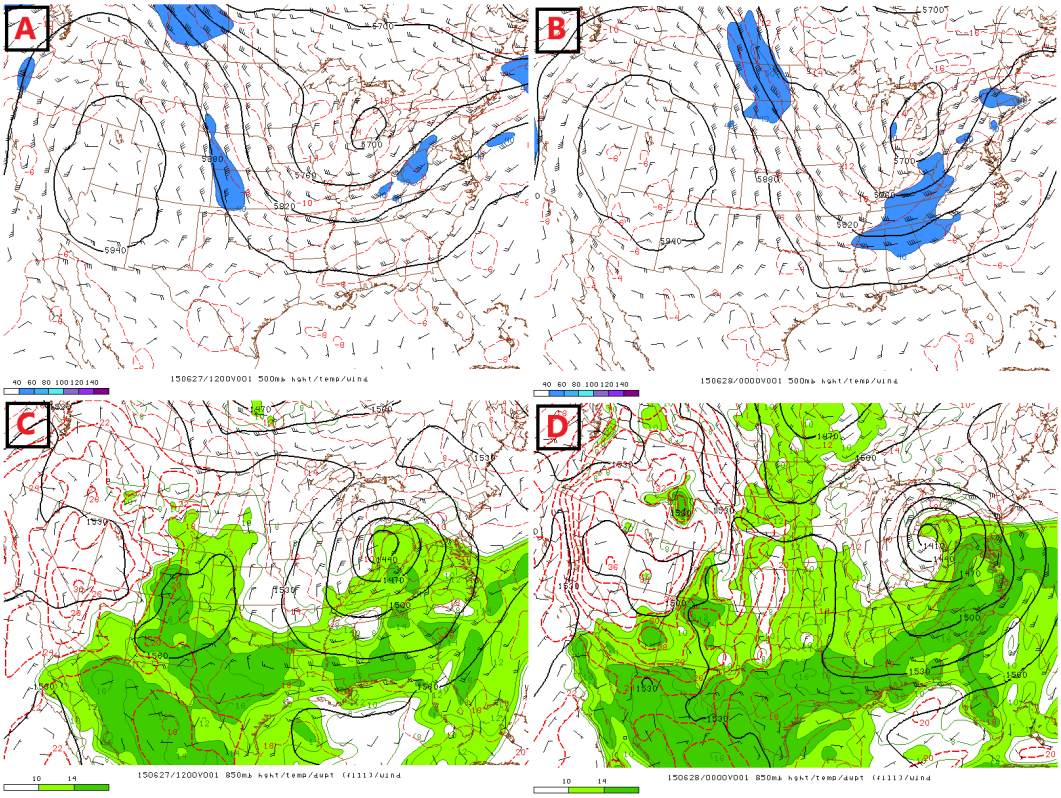

Figure 27 also shows the SPCHMA 850 hPa analysis for the preconvection and peak convection periods. Unlike the upper-level pattern, the lower atmosphere underwent substantial evolution in the 12 hr between pre- and peak convection. At 1200 UTC, 27 June, the low-level wind pattern generally restricted moisture transport into Arizona. Southerly winds coming out of the Gulf of California were incredibly weak, and the predominantly southwesterly winds over Texas and easterly winds over Mexico impeded moisture advection from the Gulf of Mexico. As time progressed closer to the peak convection period, winds over the western half of the Gulf of Mexico began to form a difluence zone, where southerly winds from the

Gulf and southern Texas diverged into easterlies and westerlies. This action increased easterly flow from the Gulf of Mexico into Arizona, building up additional moisture over the eastern Mogollon Rim.

Figure 28 displays the evolution of the convection through radar reflectivity throughout the event. As with the 4 July 2014 case, convection began at approximately 1800 UTC over the White Mountain Range and continued to develop as it moved southwest downslope. By 2200 UTC, the initial convection formed a QLCS oriented west-northwest to east-southeast with new convective cells forming in its wake farther north-northeast up into western New Mexico. Simultaneously, isolated convective cells started forming in a northwest–southeast line in the southern region of Arizona. Of note, this particular NEXRAD radar composite image was difficult to assess due to substantial radar-beam blockage east of the QLCS.

Shortly after the QLCS began to break into smaller cellular clusters. The westernmost cluster moved increasingly westward and began converging with a developing convective line that was moving southwest near the northwestern edge of the Mogollon Rim and an area of northward progressing convection that originated in southern Arizona. These three convective systems began to merge and by 0000 UTC resembled a convective line in the shape of a backward "C," collapsing on the Phoenix area. As time moved forward, the northern flank of these converging systems overtook the other two, sweeping southwest in a northwest–southeast line that passed over an area spanning from Phoenix to Tucson. This system left areas of widespread, semistationary reflectivity values in its wake, potentially indicative of lofted dust.

Figure 28. NEXRAD radar composite imagery for the 28 June 2015 case for 1800 UTC, 27 June 2015 (*A*); 2000 UTC, 27 June 2015 (*B*); 2200 UTC, 27 June 2015 (*C*); 0000 UTC, 28 June 2015 (*D*); 0200 UTC, 28 June 2015 (*E*); 0400 UTC, 28 June 2015 (*F*); and 0600 UTC, 28 June 2015 (*G*).

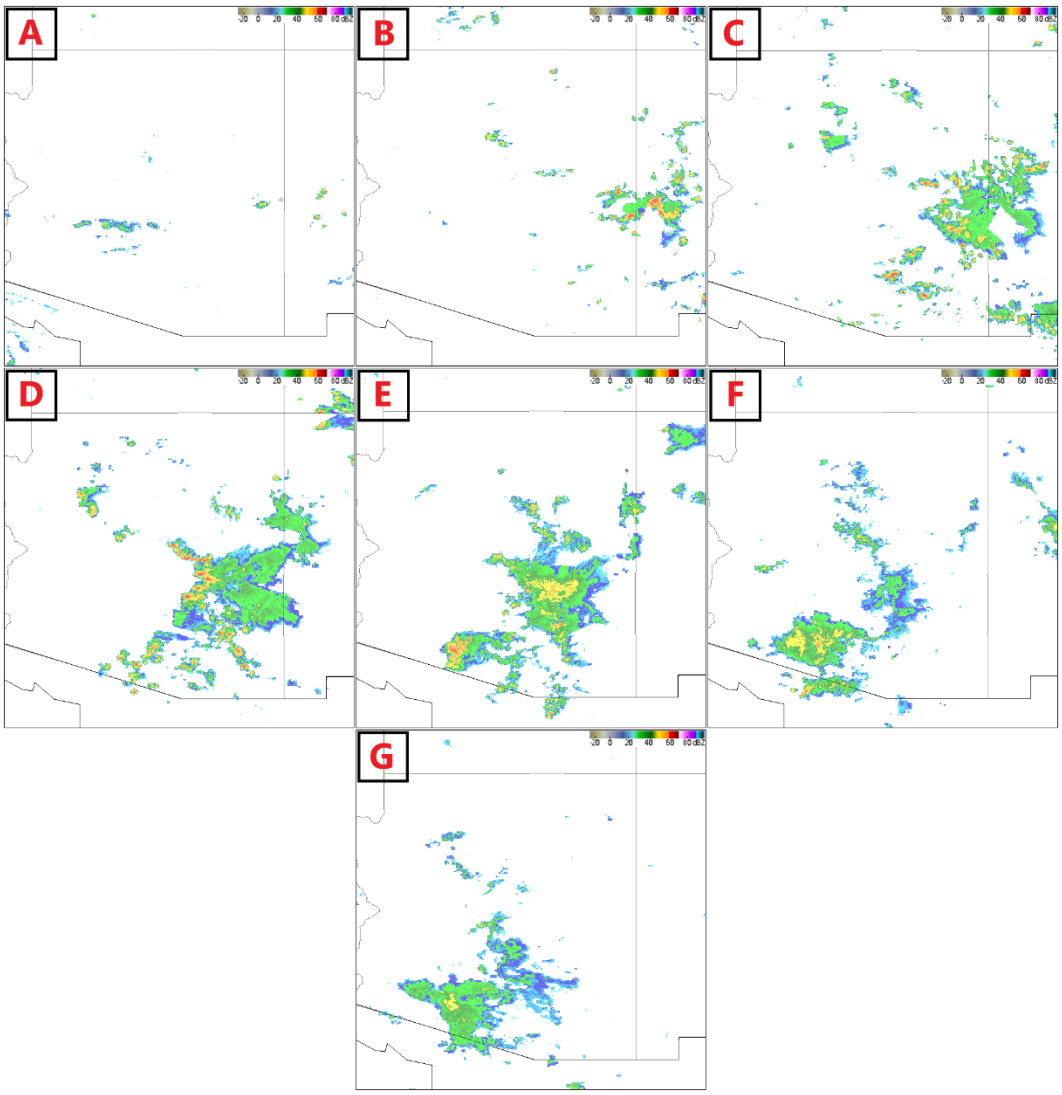

3.3.2 28 June 2015 simulation results

Overall, the simulation skillfully reproduced the 28 June 2015 dust-event synoptic conditions. Figure 29 compares the SPCHMA analysis and WRF-simulated 500 hPa height and wind fields for 1200 UTC, 27 June, and 0000 UTC, 28 June. At both times, the WRF simulation generated a highly amplified ridge over the Great Basin and a trough over the Great Lakes region. Our model captured the broadening and slightly northeast shift of the high pressure associated with the ridge. It also predicted the position of the jet streaks over Nebraska, Kansas, and Canada (north of North Dakota) at 1200 UTC, 27 June, and the jet-streak locations over

North Dakota, South Dakota, and west of California at 0000 UTC, 28 June. Furthermore, the WRF simulation effectively recreated the upper-level synoptic pattern that provided weak, large-scale forcing for convection and easterly flow in the upper atmosphere.

Figure 29. SPCHMA (*panels A* and *B*) and WRF CTRL d01 forecast (*panels C* and *D*) of 500 hPa height (*contoured*) and wind (*barbs* and *shaded*) valid at 1200 UTC, 27 June 2015 (*A*, *C*), and 0000 UTC, 28 June 2015 (*B*, *D*).

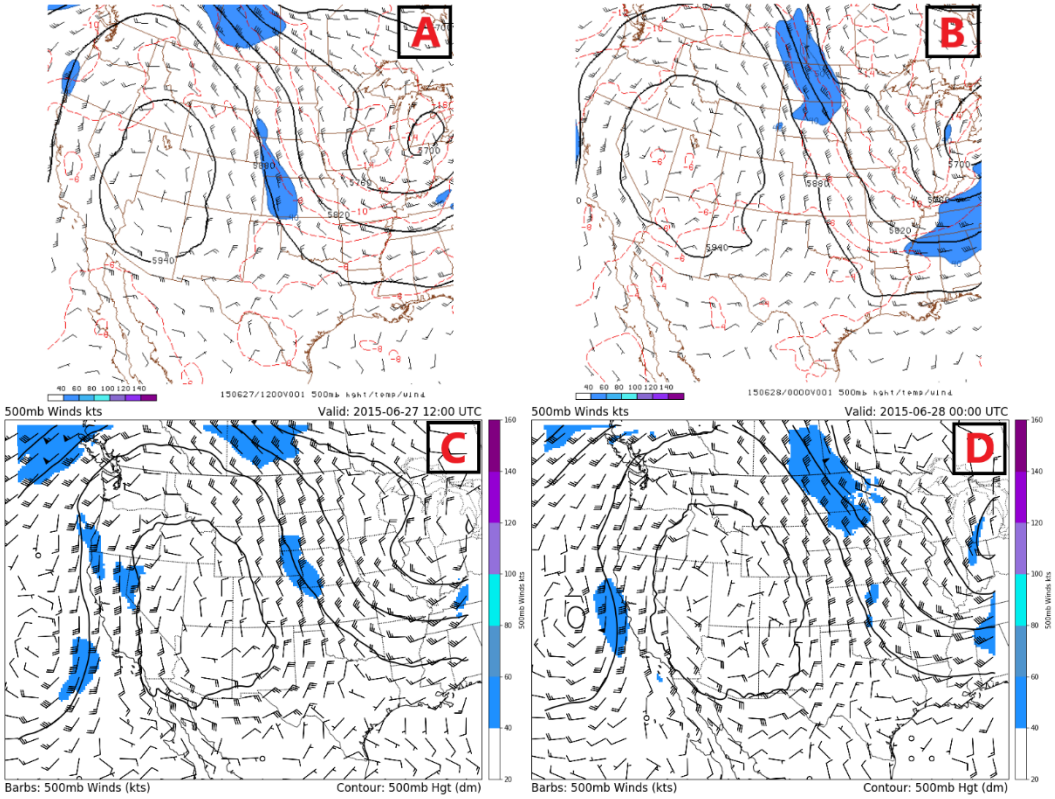

Figure 30 compares the SPCHMA analysis and WRF-simulated lower atmosphere flow pattern at 850 hPa. The simulation reproduced the 850 hPa height pattern at both preconvection and peak-convective times. Additionally, the WRF simulation captured the progression of the low-pressure system over Ohio (east of the d01 boundary), the elongation of height contours south and southwest marking the position of the cold front, and the deepening of the trough over North Dakota and Minnesota.

Assessing our simulation's ability to generate a realistic moisture source for convection was somewhat challenging. Figure 30 shows that the WRF model reproduced the stream of high dew-point temperatures and moisture ahead of the cold front (i.e., a warm conveyor belt). The model also captured the reduction in dew-point temperatures over northern Texas

and eastern New Mexico from northerly winds bringing in cold, dry air. However, simulated atmospheric pressures over sections of the Great Basin, the Rocky Mountains, and the Mexican Sierra Madre Range were lower than 850 hPa, causing data gaps in our 850 hPa forecast output.

Figure 30. SPCHMA (*panels A* and *B*) and WRF CTRL d01 forecasts (*panels* C and D) of 850 hPa height (*contoured black*), wind (*barbs*), and dew point (*shaded*, Celsius) valid at 1200 UTC, 27 June 2015 (*A*, *C*), and 0000 UTC, 28 June 2015 (*B*, *D*).

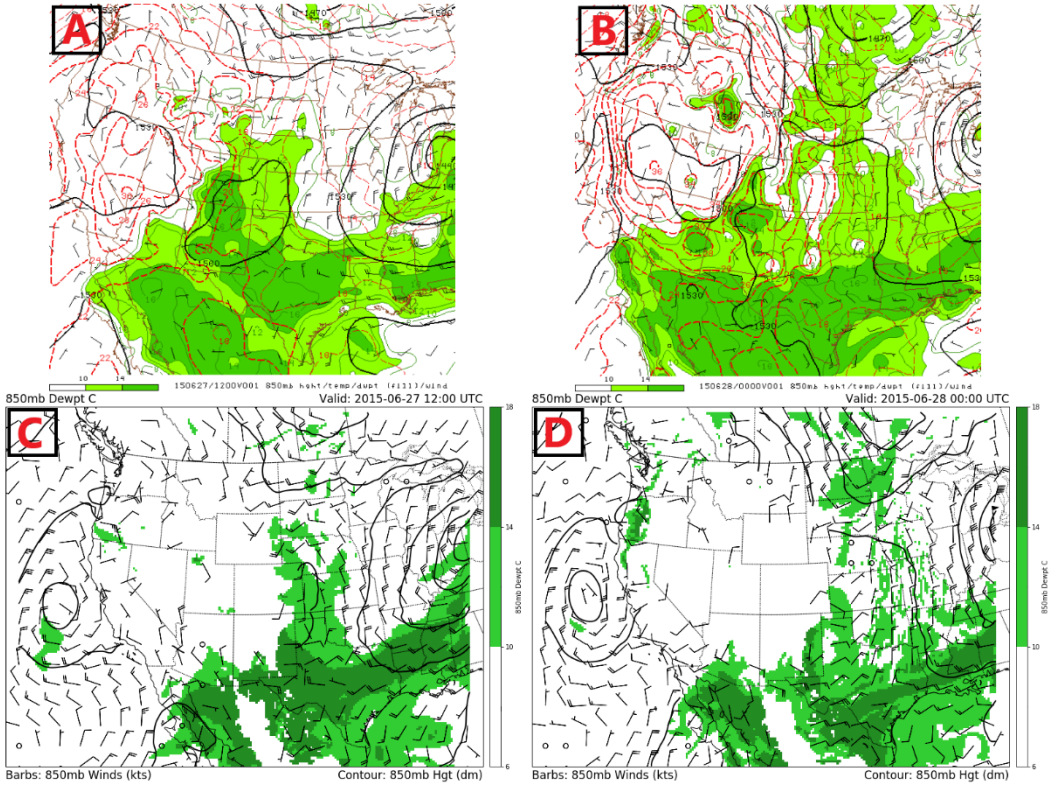

For the area where verification was possible, the simulation forecasted the development of a diffluent zone over Texas with winds split between easterly over most of Texas and westerly over eastern Texas. These diffluent winds transported moisture brought into Texas by southerly winds over Mexico and the Gulf of Mexico both west and east. This setup provided a small corridor for Gulf of Mexico moisture to funnel into Arizona, similar to the SPCHMA analysis, as winds in southeast Arizona changed from calm to 10 m s^{-1} southeasterly. As a result, WRF was also able to reproduce the SPCHMA PWAT pattern (Figure 31). At 1200 UTC, 27 June, a small area of 1.5–2 in. PWAT extended into southern Arizona, just west of Tucson. By 0000 UTC, 28 June, this area expanded westward, creating a strong north–south gradient in moisture over central Arizona and a west–east gradient near Tucson as western New Mexico dried slightly.

Figure 31. SPCHMA (*panels A* and *B*) and WRF CTRL d02 forecasts (*panels C* and *D*) of column-integrated precipitable water (under 400 hPa, *shaded* and *contoured* in inches) valid at 1200 UTC, 27 June 2015 (*A*, *C*), and 0000 UTC, 28 June 2015 (*B*, *D*). Contours are every 0.1 in.

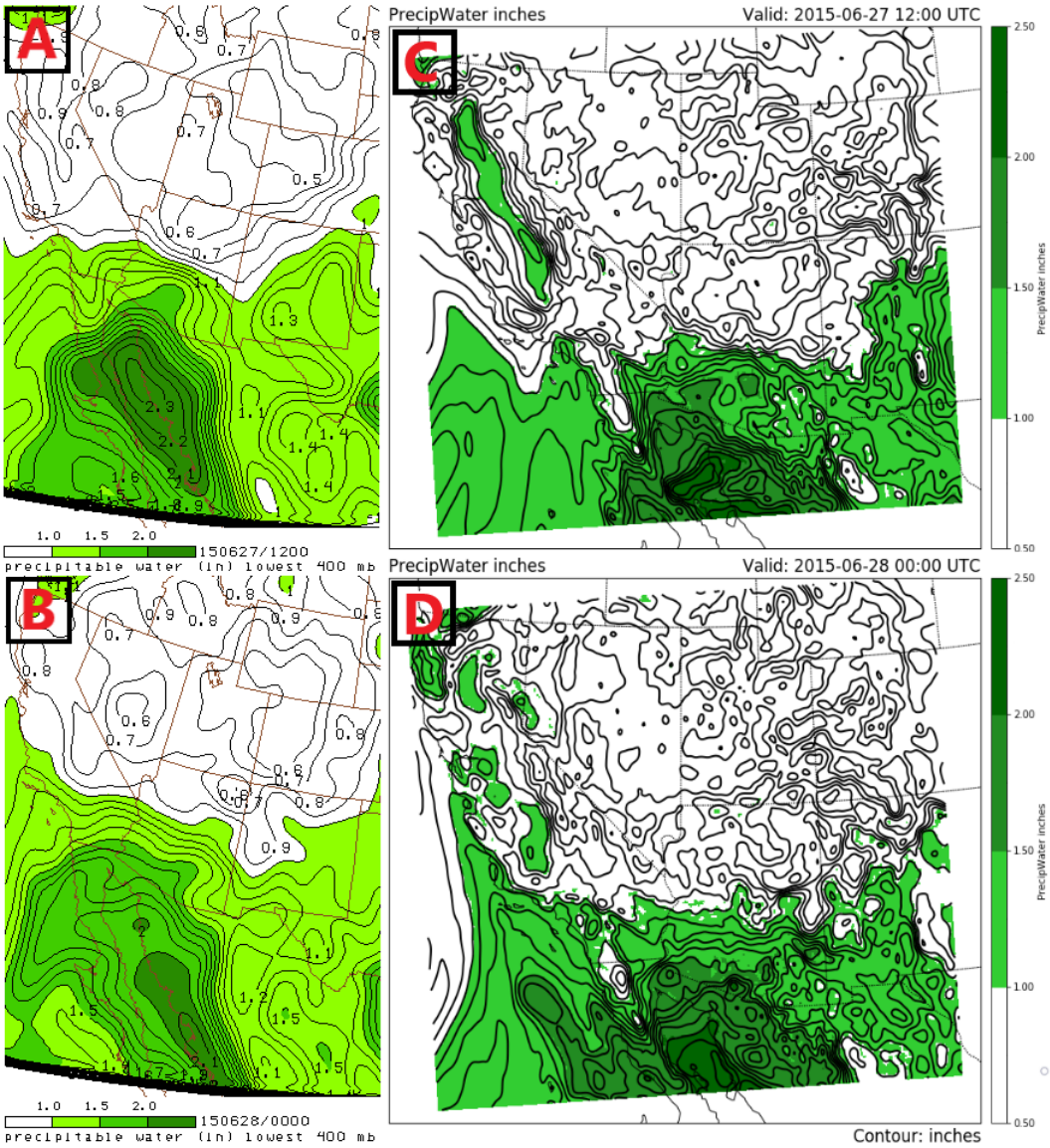

Regarding radar reflectivity (Figure 32), the model started well at 2000 UTC, 27 June, with convection initiating over the White Mountains and extending into western New Mexico in a north–south line of convective cells. The simulated convection extended farther south than the observed radar, but it is difficult to tell if the model was erroneous due to the potential for radar-beam blockage (note what appears to be a semipermanent gap in observed radar reflectivity just east of the White Mountains [highly visible at 2200 UTC]). Two hours later, the convection organized into a northwest–southeast QLCS along the ridgeline. Concurrently, isolated

thunderstorms began to form around Tucson and nearby mountain peaks. The WRF model forecasted the southern cells near Tucson, but they were considerably weaker in our simulation than reality and farther south, west of Rio Rico. At the peak of the event, 0000 UTC, 28 June, the simulation accurately forecasted the merging of several convective features to form the characteristic "backward C" shape seen in the observed radar, including the intensification and orientation of the southern line of cells

The model's most egregious failing was the progression of the eastern half of the initial QLCS. In reality, this half of the convective line advanced steadily southwest, positioned ahead of the Pinaleño (or Graham) and Chiricahua Mountains. However, the forecast was far less progressive. In the simulation, the tail end of the convective line remained wrapped counterclockwise around the White Mountains and extended into New Mexico. The back half of the line started to catch up to the observed pattern by 0200 UTC, 28 June, as northeasterly winds within the convective line, and subsequently the outflow, intensified. At this time, the model matched the observed radar reasonably well concerning the main northwest–southeast line of convection, lower reflectivity values trailing in the convection line's wake, and a more intense MCS southwest of the line near the Arizona border with Mexico.

The simulation produced overly intense convection between these two systems but otherwise predicted the structure quite well. Over the next few hours, 0400–0600 UTC, 28 June, the large northwest–southeast convective line dissipated entirely; and the MCS to the southwest began to weaken and spread out. The forecast depicted the broadening of the MCS, near Ajo northeast of the Sonoran Desert, and the weak remnant northwest–southeast reflectivity values as it collapsed. However, the model also produced additional convective cells and widespread stratiform precipitation in the wake of the QLCS that were not visible in the composite radar images. Despite some timing and erroneous precipitation issues in the southeast region, the simulation effectively recreated the overall convective structure and placement.

Figure 32. Observed NEXRAD radar (*panels A–F*) and WRF CTRL d03 simulated 1 km AGL radar (*panels a–f*) for 2000 UTC, 27 June 2015 (*A*, *a*); 2200 UTC, 27 June 2015 (*B*, *b*); 0000 UTC, 28 June 2015 (*C*, *c*); 0200 UTC, 28 June 2015 (*D*, *d*); 0400 UTC, 28 June 2015 (*E*, *e*); and 0600 UTC, 28 June 2015 *(F, f)*.

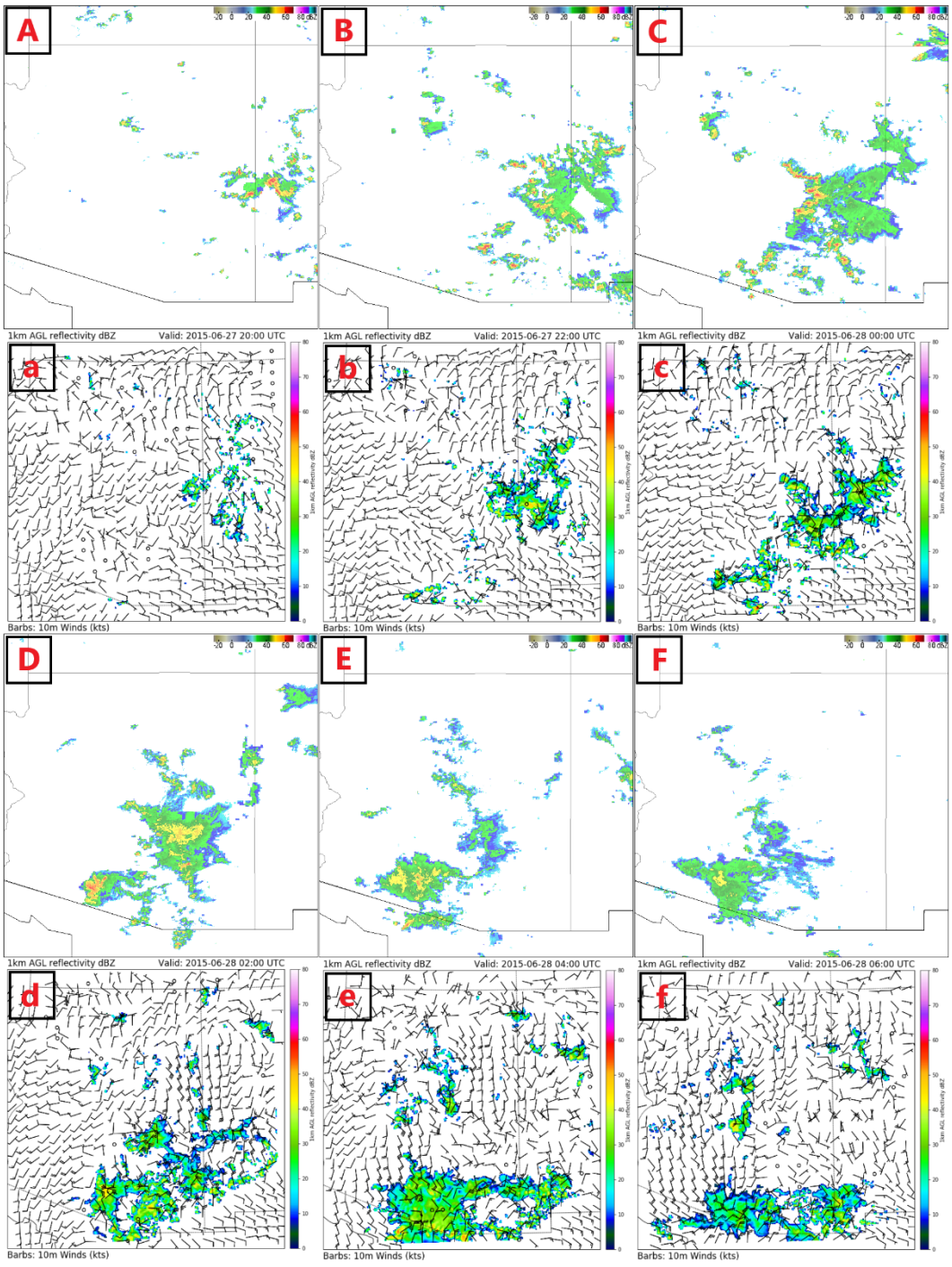

The observed and forecasted ASOS network average wind speed showed incredible agreement for the first 27 hr (75%) of the event (Figure 33). On 27 June, the model slightly underpredicted winds between 0000 and 0300

UTC and overpredicted winds between 1000 and 1500 UTC but followed the buildup to the peak of the event between these periods nearly perfectly. The model only slightly underestimated the average peak of the event by about 0.3 m s^{-1}, but it erroneously maintained higher wind speeds between 0300 and 1200 UTC, 28 June. This error was the primary contributor to the average bias of +0.586 m s^{-1}.

Some of the timing issues discussed previously were evident in the time series of individual stations like KSAD, an ASOS station located near the eastern border of Arizona at the base of the White Mountains, just south of where convective activity began. The model agreed perfectly with observations on the intensity of the peak winds, about 15 m s^{-1}, but arrived 5 hr later, an outcome consistent with the slower progression of the eastern half of the convective line. Time series from three stations spread throughout the Phoenix area near the center of this event (KPHX, KSDL, and KDVT) also demonstrated a similar pattern. The peak intensity forecasted at these stations relative to observations varied (+2 m s^{-1}, +2.8 m s^{-1}, and +1.25 m s^{-1}, respectively), but each station time series displayed secondary peaks, sustained high winds for an additional 4 hr (0200–0600 UTC, 28 June), or both. Overall, the simulation handled the development and peak of this event well; but the event propagated too slowly, extending the duration of the forecasted event.

Analysis of RAWS surface wind speeds in Figure 34 shows similar patterns to that of ASOS. Simulated and observed patterns agreed up until 2200 UTC, 27 June (forecast hour 22). At that point, the model predicted peak wind speeds about 2.75 m s^{-1} faster than observed and maintained the overprediction throughout the remainder of the forecast period, resulting in an average bias of +1.02 m s^{-1}. Time-series comparisons for stations QGLA3 and QSLA3 indicated a late arrival of peak winds nearly identical to our assessment at the ASOS KSAD station. This pattern provided further evidence that the modeled convection progression in the southeast corner of Arizona was too slow. Closer to the center of the event at GRAA3, southeast of Phoenix, the model matched nearly perfectly with observations and had far less overprediction in the wake of peak winds. This outcome indicated that the sustained overprediction might be a result of a small rogue convective cell. Lastly, at BLMA3, the forecasted winds followed a similar pattern as the observations but intensified too early and peaked about 5 m s^{-1} faster. This pattern was in part due to the broader

area covered by the southern MCS and its subsequent outflow boundary reaching farther north ahead of the main QLCS.

Figure 33. Time series of observed (*black*) and modeled (*red*) surface (10 m) wind speed during the 28 June 2015 dust storm for network average of all ASOS stations (*A*), KSAD (*B*), KPHX (*C*), KSDL (*D*), and KDVT (*E*). The *gray line* in the network average shows the number of stations used in the network average. The 1 min observations are supplemented by METARS at individual stations when needed and are denoted by *dots*.

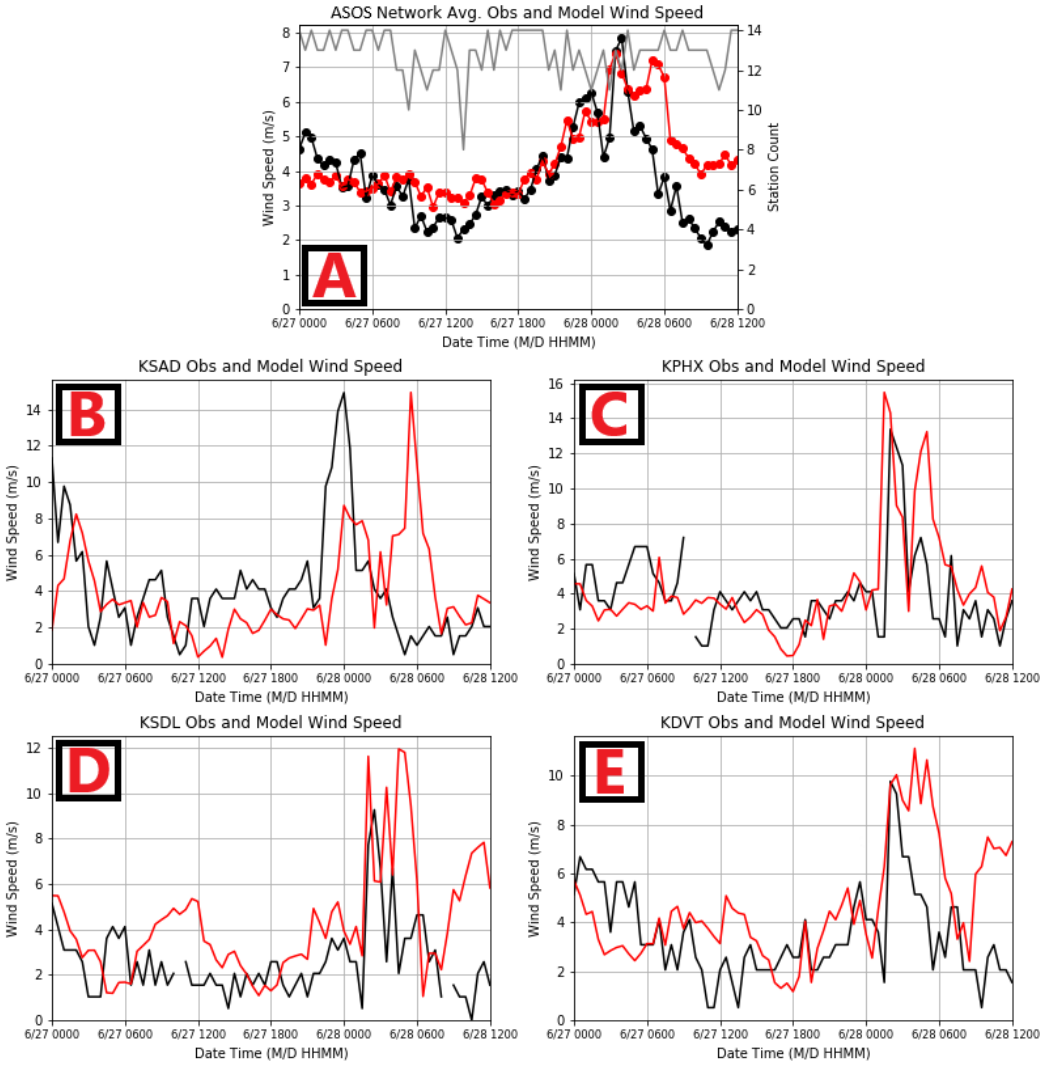

Figure 34. Time series of observed (*black*) and modeled (*red*) surface (10 m) wind speed during the 28 June 2015 dust storm for network average of all RAWS stations (*A*), QGLA3 (*B*), QSLA3 (*C*), GRAA3 (*D*), and BLMA3 (*E*) surface (6.1 m) wind speed. *Dots* are used for individual stations since data is reported only once every hour with no specific reporting time.

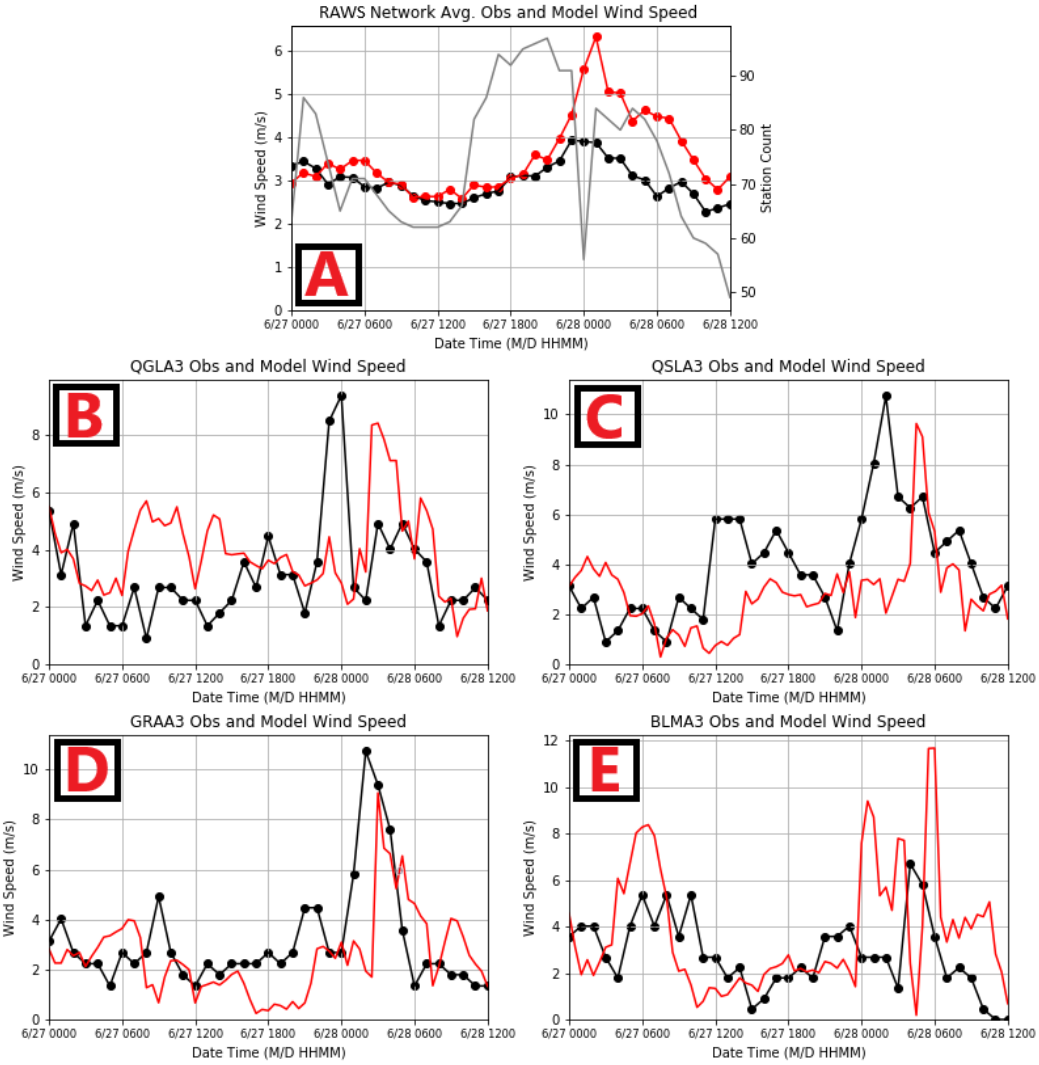

3.4 1–2 August 2017 case study

3.4.1 1–2 August 2017 event overview

The 1–2 August 2017 case was a multiday dust event over northwest Arizona and eastern California that lasted from 0200 UTC, 31 July through 1000 UTC, 3 August. At 0000 UTC, 31 July, the SPCHMA 500 hPa flow pattern showed incredibly weak height gradients and winds with a broad high-pressure system and a zonal (i.e., flat) ridge centered over the Great Basin and a trough with a positively tilted axis (i.e., tilted towards the east) draped across the US East Coast (Figure 35).

Figure 35. SPCHPA of 500 hPa height (*contoured*) and wind (*barbs* and *shaded*) valid at 0000 UTC, 31 July 2017 (*A*); 1200 UTC, 31 July 2017 (*B*); 0000 UTC, 1 August 2017 (*C*); 1200 UTC, 1 August 2017 (*D*); 0000 UTC, 2 August 2017 (*E*); 1200 UTC, 2 August 2017 (*F*); and 0000 UTC, 3 August 2017 (*G*).

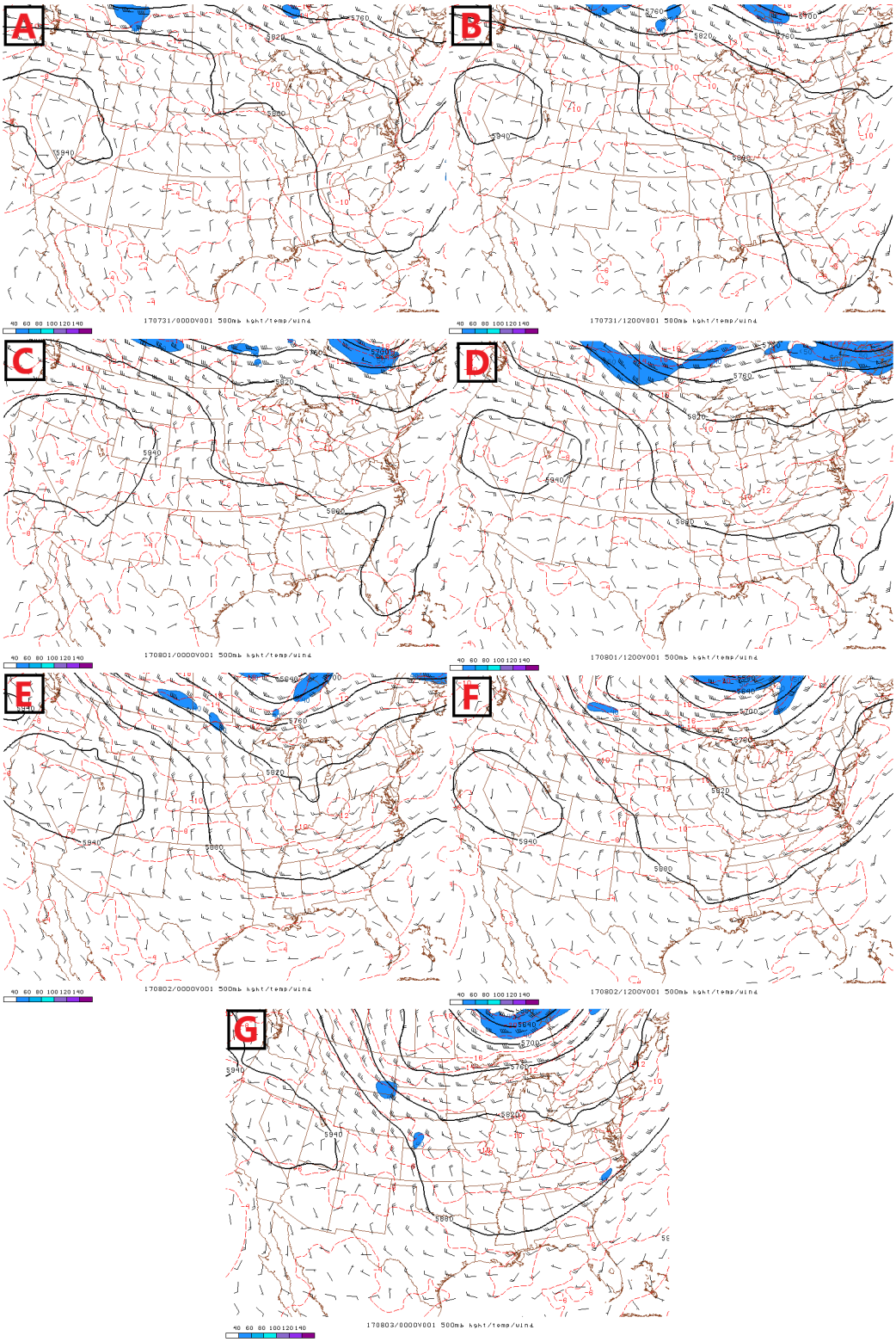

Over the next two days, the synoptic pattern began to evolve. The high-pressure system remained stationary but extended slightly eastward as the ridge amplified and became less zonal. Stronger northwesterly and northerly winds sped down the east side of the Rocky Mountains as the height contours began to tighten and the downstream trough built backward toward the Mississippi River Valley. This change led to a shift in upper-level winds over Arizona from light and variable to more consistently east-northeasterly. The 0000 UTC, 2 August, SPCHMA product best exemplified the new synoptic pattern, though conditions were still changing.

The flow pattern continued to amplify as strong northwesterly winds persisted over the northern and central plains, acting to broaden the trough and tighten height gradients upstream of its axis. Additionally, this distorted and weakened the Great Basin high pressure over time, pulling and elongating the high-pressure zone into a more northwest–southeast orientation. As this occurred, winds above the DSWUS region gradually shifted from uniformly east-northeasterly to southeasterly and even southerly, weakening with the high pressure. Of note, portions of this 500 hPa setup closely resembled features identified by NOAA as common synoptic dust forcing conditions for the DSWUS (Lader et al. 2016; see Dust Storm Pattern 2).

The flow pattern of the lower atmosphere, just like the upper-level pattern, underwent substantial evolution throughout the event duration. Figure 36 shows the SPCHMA 850 hPa analysis at each of the critical stages of development. At the initial time (0000 UTC, 31 July), the 850 hPa analysis showed broad high and low pressures centered over Wisconsin and northern Mexico, respectively. These pressure systems promoted northerly flow over the US east coast that shifted northeasterly as it approached the Georgia-Florida area. As the pressure system continued to rotate clockwise, the flow became easterly over the southern coast and southeasterly and southerly over central Mexico, northern Texas, and the Great Plains. This flow pattern created a stream of low-level moisture coming from the Gulf of Mexico that split as it made landfall, moving west-northwesterly along the US-Mexico border and northerly up the central plains. At 0000 UTC, 1 August, the high pressure had moved southeast, centered over Indiana, and showed signs of shrinking. Over the next day, the high pressure continued to move east-southeast and wane. Between 0000 UTC, 31 July, and 0000 UTC, 2 August, this pattern supplied a nearly constant flow of moisture

from the Gulf of Mexico into the DSWUS, albeit weakened as the high pressure decayed or blocked by weak northerly winds over New Mexico.

As the initial high-pressure system moved off to the east and decayed, another appeared as higher pressure poured down the eastern side of the Rockies into the central US At 1500 UTC, 2 August, the 850 hPa pattern had changed over the DSWUS. High pressure settled over New Mexico and northern Texas, cutting off flow from the Gulf of Mexico and promoting southerly winds over the Gulf of California. The secondary high pressure dissipated rapidly, vanishing completely by 2100 UTC, 2 August, as low pressure over the Great Basin intensified. Both of these pressure systems provided southerly winds over the Gulf of California and supplied ample moisture ahead of the last peak in convection for this event at 0000 UTC, 3 August. Throughout this event, overall winds over the DSWUS remained east-southeasterly, interrupted only briefly by bursts of southerly wind at 2200 UTC, 1 August, and 0200 UTC, 2 August (not shown), and 2000 UTC, 2 August, through 0000 UTC, 3 August, shown in Figure 36. This transported moisture behind or ahead of convection during the first and latter halves of the event, respectively.

While this dust event was the longest duration case study in our analysis, convective activity did not occur continuously over the entire 80 hr. Rather, thunderstorms developed, traveled, and dissipated in a similar diurnal pattern over the 3 days. Figure 37 shows the evolution of convection at notable time periods. Initial convective activity began on 0200 UTC, 31 July, as small pop-up thundershowers formed along the northwest end of the Mogollon Rim and just south of the Kaibab Plateau. These individual cells moved south-southwest, rapidly intensified, and decayed by 0330 UTC, 31 July. Convection quickly reorganized as a small north–south QLCS that moved over the Mohon Mountains (0430 UTC) but lost coherence shortly after (0530 UTC) as convection proceeded to move increasingly southward. Most of the convective activity had ceased around 0900 UTC, 31 July, and remained inactive until 12 hr later when isolated thunderstorms began to develop over the northern half of Arizona. However, this follow-on convection never properly organized as it traveled southwest in loose, northwest–southeast bands of individual thunderstorms. These lines passed over Flagstaff in northern Arizona and the Mohon Mountains.

Figure 36. SPCHMA of 850 hPa height (*contoured black*), wind (*barbs*), and dew point (*shaded*, Celsius) valid at 0000 UTC, 31 July 2017 (*A*); 0600 UTC, 31 July 2017 (*B*); 0000 UTC, 1 August 2017 (*C*); 0000 UTC, 2 August 2017 (*D*); 1500 UTC, 2 August 2017 (*E*); 2100 UTC, 2 August 2017 (*F*); and 0000 UTC, 3 August 2017 (*G*).

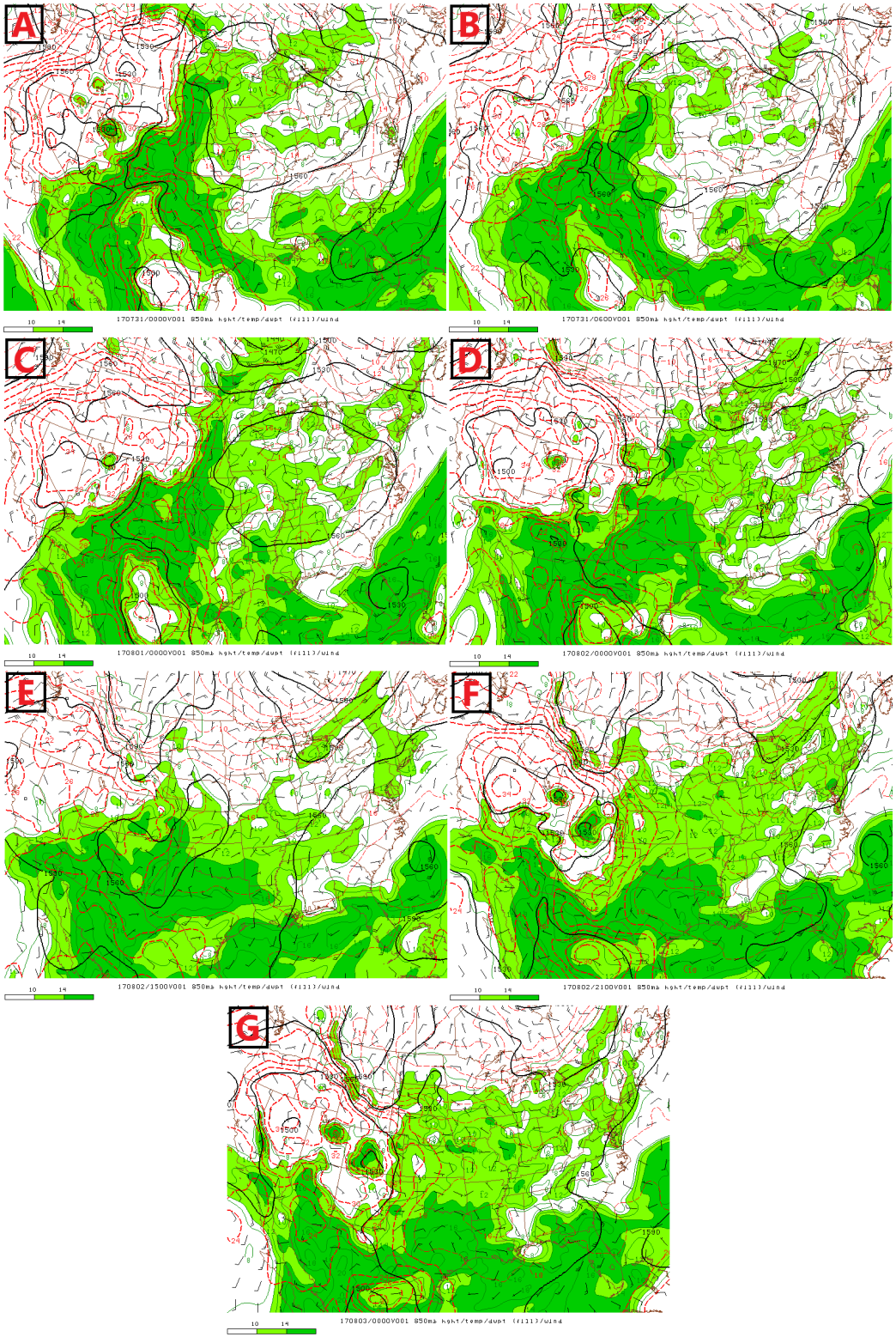

Figure 37. NEXRAD radar composite imagery for the 1–2 August 2017 case for 0200 UTC, 31 July 2017 (*A*); 0430 UTC, 31 July 2017 (*B*); and 0700 UTC, 31 July 2017 (*C*); 2100 UTC, 31 July 2017 (*D*); 0000 UTC, 1 August 2017 (*E*); 0300 UTC, 1 August 2017 (*F*); 0600 UTC, 1 August 2017 (*G*); 2200 UTC, 1 August 2017 (*H*); 0000 UTC, 2 August 2017 (*I*); 0200 UTC, 2 August 2017 (*J*); and 0400 UTC, 2 August 2017 (*K*); and 2000 UTC, 2 August 2017 (*L*); 0000 UTC, 3 August 2017 (*M*); 0130 UTC, 3 August 2017 (*N*); and 0300 UTC, 3 August 2017 (*O*).

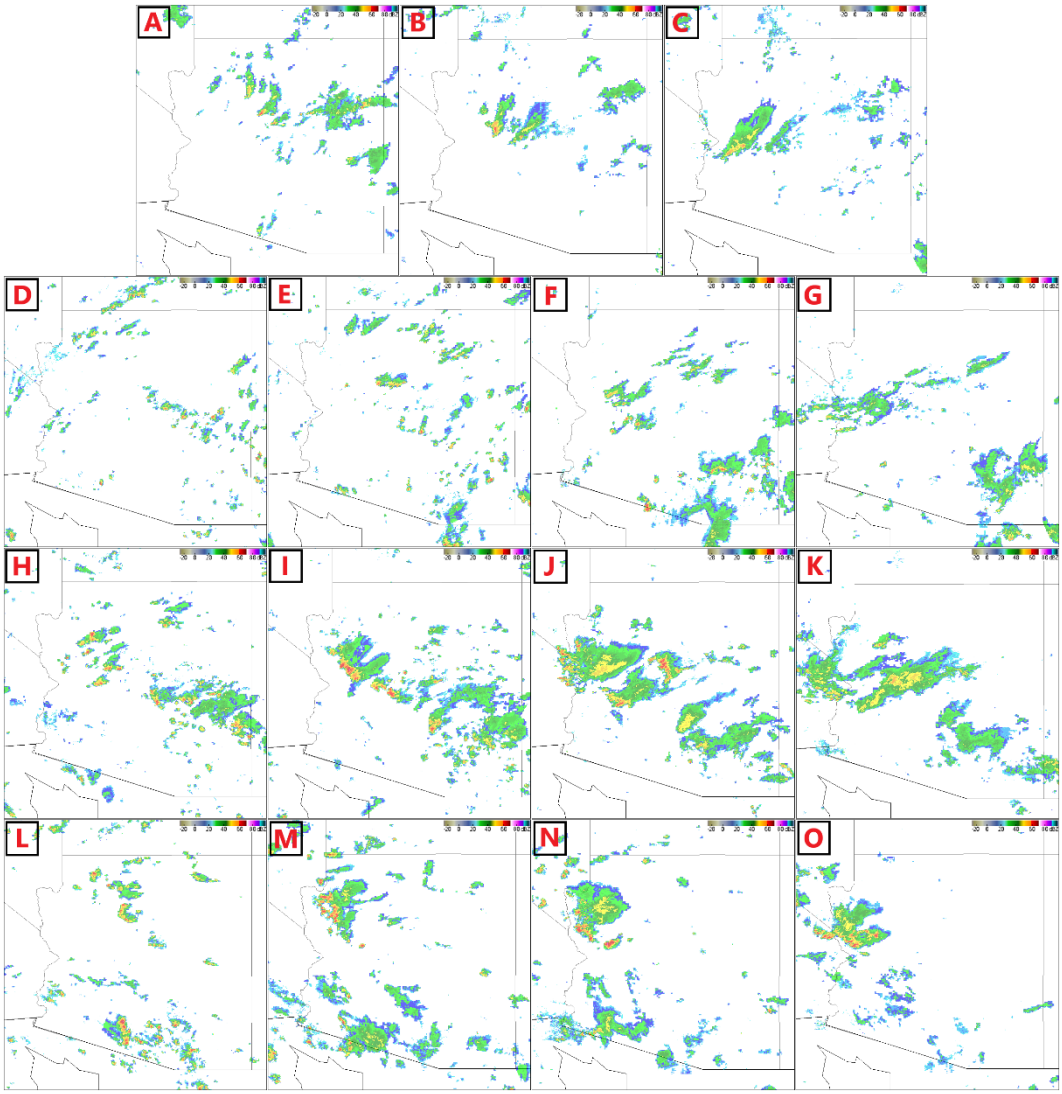

At 0630 UTC, 1 August, the radar composites (Figure 37) show a long, west–northeast line of weak radar reflectivity values left in the wake of the passing thunderstorms spanning from south of Pinon, Arizona, to Palm Springs, California. The convective activity went quiet again until 2000 UTC, 1 August, when the general pattern began to repeat. Again, the convection began as individual thunderstorms traveling south-southwest. This time, however, multiple cells coalesced and organized into an intense northwest–southeast QLCS over the Mohon Mountains, peaking in intensity at 0000 UTC, 2 August. At the same time, a secondary convective line

formed just southeast of the main line over the Bradshaw Mountains, northwest of Phoenix. Both lines progressed farther southwest, deteriorating along the way. By 0130 UTC, 2 August, the main line substantially weakened and broke apart while the second line persisted until 0230 UTC, 2 August.

As the primary QLCS dissipated, a tertiary QLCS formed northeast of Flagstaff at 0130 UTC, 2 August, and traveled in the wake of the secondary QLCS until it gradually weakened by 0430 UTC, 2 August. The cycle continued as convection ceased from 0500 to 1900 UTC, 2 August, before starting up again as isolated thunderstorms. A northwest–southeast QLCS formed on the northern end of the Mohon Mountains closer to Nevada and reached its maximum intensity at 0000 UTC, 3 August. Just south of the QCLS, a secondary cluster of convective cells grew, peaking in intensity at 0130 UTC, and moved westward, merging with the QLCS as it weakened slightly. These features moved together as a convective line before breaking apart into individual cells at 0400 UTC, 3 August. This cluster of cells continued to move west-southwest and were briefly reinvigorated before collapsing by 1000 UTC, 3 August, over Palm Springs.

3.4.2 1–2 August 2017 simulation results

Due to this event's long duration, upper-level and large-scale synoptic features were essential to the evolution of the resulting convection, making the accurate characterization of the synoptic conditions critical to the overall success of the simulation. Figure 38 shows SPCHMA analysis and WRF-simulated 500 hPa flow patterns at regular intervals throughout the event. In general, our simulation reproduced the upper-level evolution quite well, including the initial synoptic setup with a highly flat zonal ridge covering much of the western US; small, weak high pressure centered over northern California and Nevada; and a trough over the eastern US with a step-like "kink" over Nebraska and South Dakota. Our simulation also predicted the gradual amplification of the ridge starting at 1200 UTC, 1 August, the strengthening northerly winds in the lee of the Rockies, and the appearance of a jet streak between Nebraska and Montana by 0000 UTC, 3 August. However, we did note some minor differences, especially the high pressure over the US West Coast being too broad for the entire event duration. As a result, there was occasional disagreement between the WRF-simulated and the SPCHMA analysis upper-level wind speed and direction over the DSWUS, particularly between 1200 UTC, 1 August, and

0000 UTC, 2 August. During this period, our simulation forecasted southerly winds along the California-Arizona border and western Arizona while the analysis product consistently had easterly upper-level winds due to its more compact and coherent circulation of the high pressure. These potential simulated upper-level flow errors may have influenced the resultant steering of deep convection and shear available for developing convection; but overall, we considered the synoptic evolution well forecasted.

Figure 38. SPCHMA (*panels A–F*) and WRF CTRL d01 forecasts (*panels a–f*) of 500 hPa height (*contoured*) and wind (*barbs* and *shaded*) valid at 1200 UTC, 31 July 2017 (*A*, *a*); 0000 UTC, 1 August 2017 (*B*, *b*); 1200 UTC, 1 August 2017 (*C*, *c*); 0000 UTC, 2 August 2017 (*D*, *d*); 1200 UTC, 2 August 2017 (*E*, *e*); and 0000 UTC, 3 August 2017 (*F*, *f*).

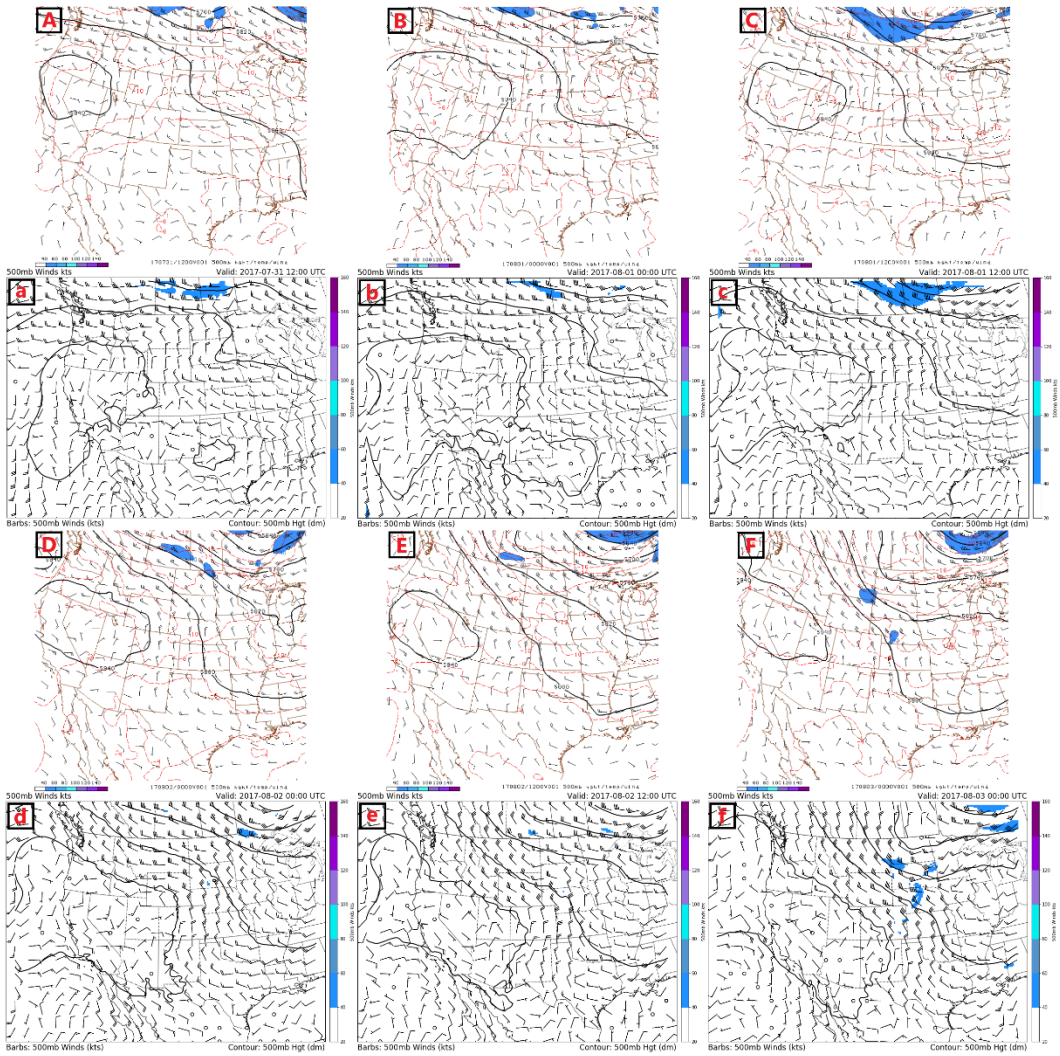

At the 850 hPa level (Figure 39), our simulation effectively captured features such as the weakening and progression of the high pressure over the Great Lakes farther eastward; the shift in wind direction over Texas from southeasterly to northeasterly; and the gradual building of higher dewpoint temperatures and moisture farther west into southwest Arizona, southeast California, and the southern tip of Nevada. These features were all essential aspects of the low-level flow, indicating that WRF also captured the cutting off of moisture transport from the Gulf of Mexico and the building of moisture availability ahead of convective development through light southerly winds out of the Gulf of California. Other aspects of the low-level flow, like the transient high pressure over the Great Basin between 1500 and 2100 UTC, 2 August, and the moisture content in the northernmost region of Arizona, approximately a third of the whole state, were difficult to verify due to data gaps in the simulated 850 hPa fields over high terrain where the near-surface pressure fell below 850 hPa. One notable difference between our simulation and the SPCHMA is WRF's tendency to favor continuously easterly winds over the southern half of Arizona. This discrepancy caused our simulation to match well with the SPCHMA when the wind pattern was more consistent (e.g., 0600 UTC, 31 July, and 1500 UTC, 2 August). In reality, however, the low-level winds for the majority of this event were relatively weak (e.g., less than 5 kn [2.57 m s^{-1}]) and sporadic in direction.

While our simulation did forecast weak and calm winds, its tendency towards an easterly direction may have influenced the resultant steering of convection. Despite this inconsistency, the moisture availability forecasted by the WRF model matched nearly perfectly with that of the SPCHMA (Figure 40). Our simulation started well, capturing the placement of local maxima in PWAT over southwest Arizona and the Gulf of California. As the simulation progressed, it matched the SPCHMA product's moisture content increase over the California-Arizona border, with moisture extending northward along the Arizona-Nevada border and westward through California toward the Santa Barbara Basin.

Figure 39. SPCHMA (*panels A–F*) and WRF CTRL d01 forecasts (*panels a–f*) of 850 hPa height (*contoured black*), wind (*barbs*), and dew point (*shaded*, Celsius) valid at 0600 UTC, 31 July 2017 (*A*, *a*); 0000 UTC, 1 August 2017 (*B*, *b*); 0000 UTC, 2 August 2017 (*C*, *c*); 1500 UTC, 2 August 2017 (*D*, *d*); 2100 UTC, 2 August 2017 (*E*, *e*); and 0000 UTC, 3 August 2017 (*F*, *f*).

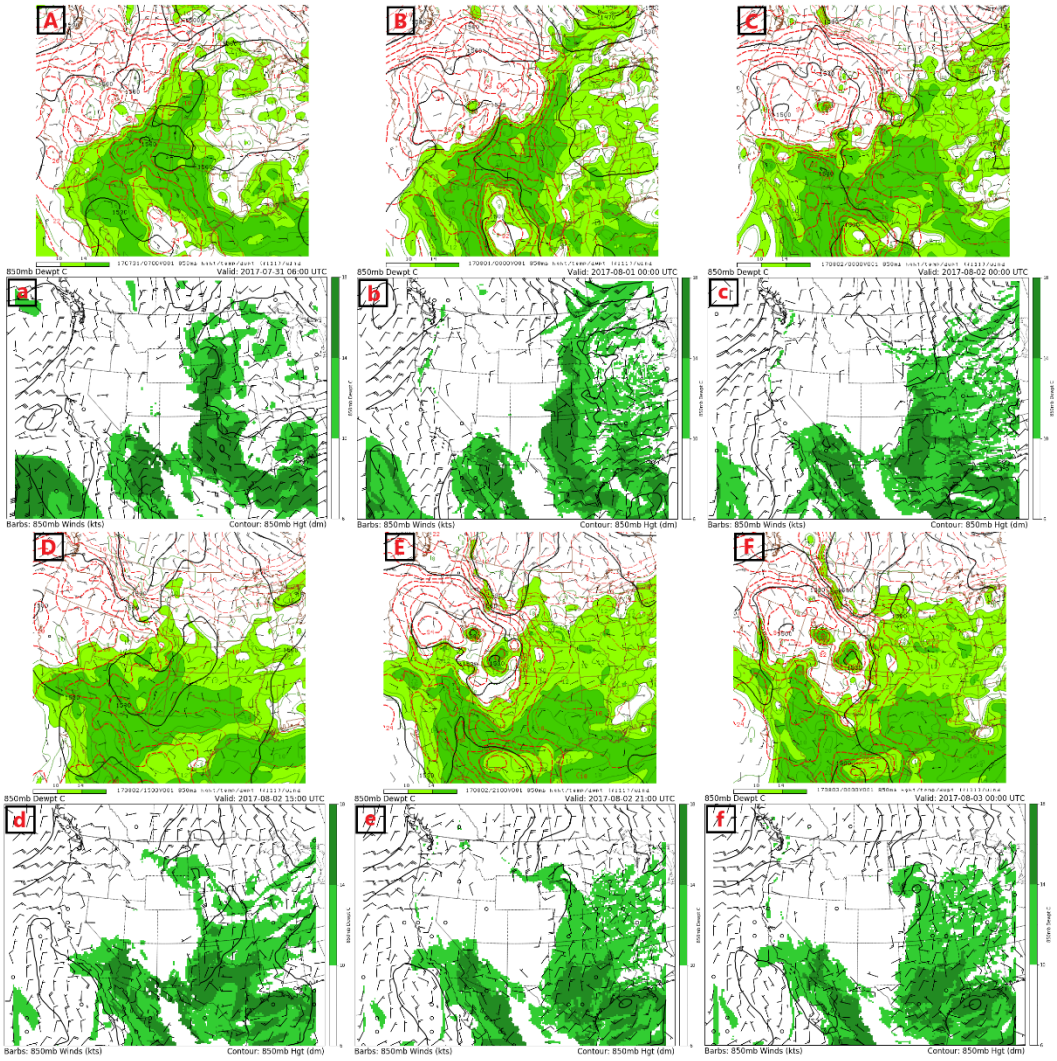

Figure 40. SPCHMA (*panels A–F*) and WRF CTRL d02 forecasts (*panels a–f*) of column-integrated precipitable water (under 400 hPa, *shaded* and *contoured* in inches) valid at 0600 UTC, 31 July 2017 (*A*, *a*); 1800 UTC, 31 July 2017 (*B*, *b*); 0600 UTC, 1 August 2017 (*C*, *c*); 1800 UTC, 1 August 2017 (*D*, *d*); 0600 UTC, 2 August 2017 (*E*, *e*); and 1800 UTC, 2 August 2017 (*F* and *f*). Contours are every 0.1 in.

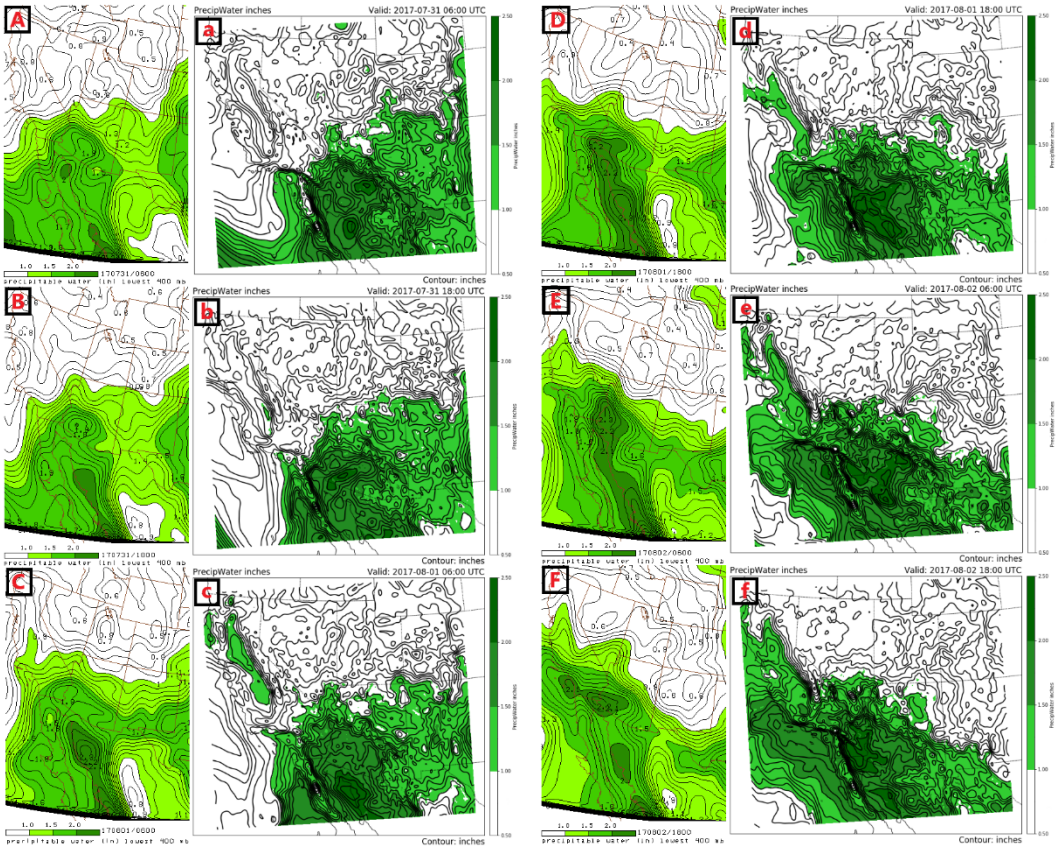

For conciseness, we compared the simulated and observed radar reflectivity only during periods of peak convective activity (Figure 41). In general, we were not overly concerned with simulated convection between 0000 and 0900 UTC, 31 July, due to its weak intensity relative to the main dust event, which would not occur until 0000 UTC, 2 August. However, we did verify that our model favored convective activity shortly after initialization. Furthermore, our simulation developed a southwest–northeast convective line at 0700 UTC similar to the NEXRAD imagery, albeit displaced slightly, weaker, and later than observed.

During the next convectively active period, 2100 UTC, 31 July, to 0600 UTC, 1 August, our simulation reproduced the initiation of isolated convective cells along the Mogollon Rim and elevated gradients. However, development was farther west than observed, shown at 0000 UTC, 1 August. Shortly after at 0300 UTC, 1 August, our simulation forecasted a single cell approaching the California-Arizona border. While the observed radar

showed a clustering of small cells instead of one moderately sized cell, the simulated pattern was consistent with the overall flow and positioning of the observed radar reflectivity for the remainder of the period.

Figure 41. Observed NEXRAD radar (*panels A–G*) and WRF CTRL d03 simulated 1 km AGL radar (*panels a–g*) for 0700 UTC, 31 July 2017 (*A*, *a*); 0000 UTC, 1 August 2017 (*B*, *b*); 0200 UTC, 1 August 2017 (*C*, *c*); 0000 UTC, 2 August 2017 (*D*, *d*); 0300 UTC, 2 August 2017 (*E*, *e*); and 0000 UTC, 3 August 2017 (*F*, *f*); and 0300 UTC, 3 August 2017 (*G*, *g*).

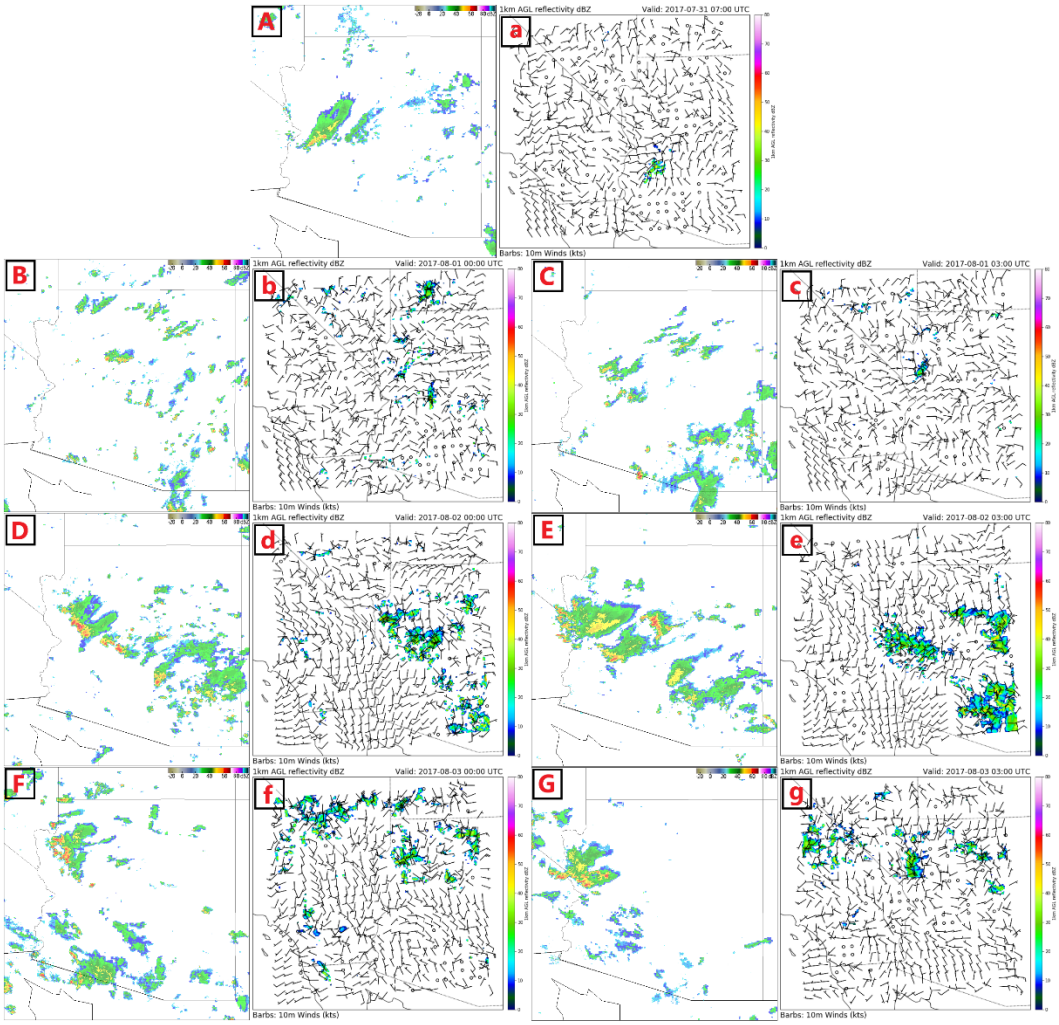

The next convective stage marked the first peak of convective activity, 2200 UTC, 1 August, through 0400 UTC, 2 August, during which our model matched the convective evolution quite well (e.g., Figure 41). At the peak of the period (0000 UTC, 2 August), our simulation had a northwest–southeast convective line that closely followed topographic features (extending from the Arizona-Nevada border down to Tucson), with an intense concentrating leading edge on the southwest side ahead of the trailing precipitation to the northeast. While the intensity of the leading edge

of the line in the northwest region of Arizona was not as intense as in the observed radar, the storm structure matched incredibly well. Two hours later, 0200 UTC, 2 August, the simulation continued to predict the leading edge of the convective activity well, maintaining the line's northwest–southeast orientation and passage into eastern California. Where our model faltered slightly, however, was in the prediction of the small but intense QLCS that passed over Flagstaff. Our simulation produced a longer, west–east QLCS slightly behind the observed northwest–southeast QLCS.

During the final convectively active period and the secondary peak, 2000 UTC, 2 August, to 0300 UTC, 3 August, our simulation performed similarly to the previous convective peak. At the time of peak convection, 0000 UTC, 3 August, it resembled the observed radar quite well, albeit with a weaker leading convective edge. The model produced a north–south convective line approaching the Arizona-Nevada border with scattered convection to the north arcing through Nevada to northeast Arizona and weaker cells in southern California. The important differences were that the observed QLCS had a more northwest–southeast orientation than our simulation and was more intense, which caused further discrepancies as the line progressed.

Three hours later, our simulation maintained a north–south orientation of the QLCS that continued to progress westward into Nevada. In contrast, the observed QLCS shifted its orientation to more west–east and moved southerly along the border. This disparity was partially due to the easterly low-level winds produced by the model over the majority of Arizona, prompting the QLCS to align itself perpendicular to steering flow. Despite this deviation, we considered the overall development and evolution of the entire case study skillfully forecasted, given the event's length and variety of observed convection.

Our comparison of observed and forecasted surface wind speeds, averaged over the ASOS network, shows persistent overprediction of winds throughout the event (Figure 42). While the general pattern and timing of the forecast followed the observations closely (except between 0600–1100 UTC, 2 August), we found biases of approximately +1 m s^{-1} and +0.5 m s^{-1} for peak wind speeds and lulls between convective periods, respectively. Furthermore, the event ASOS network average bias for our WRF simulation was +0.652 m s^{-1}.

Figure 42. Time series of observed (*black*) and modeled (*red*) surface (10 m) wind speed during the 1–2 August 2017 dust storm for the network average of all ASOS stations (*A*), KGCN (*B*), KFLG (*C*), KIGM (*D*), and KEED (*E*). The *gray line* in the network average shows the number of stations used in the network average. The 1 min observations are supplemented by METARS at individual stations when needed and are denoted by *dots*.

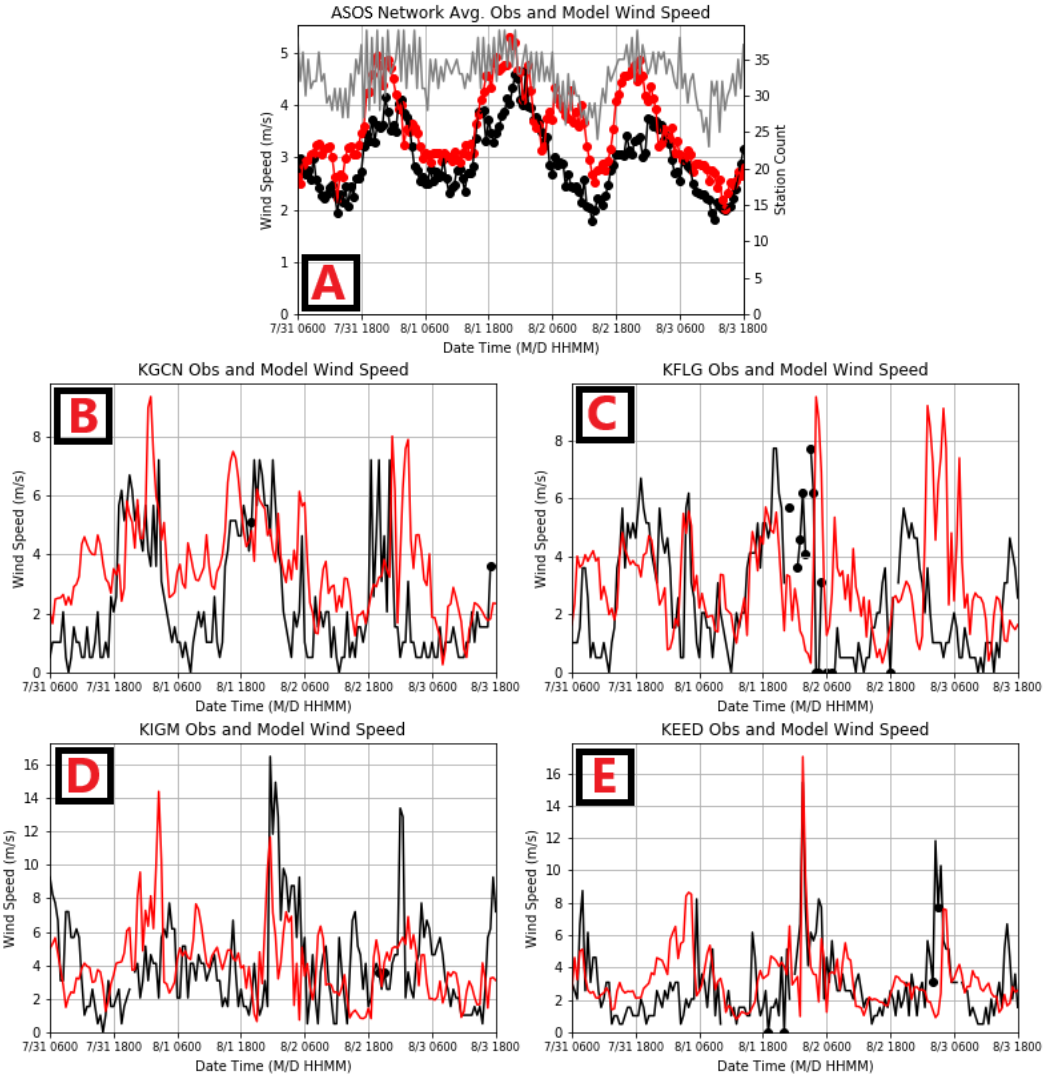

While the ASOS network average bias appears relatively high, verification at individual stations in the area of convective activity suggests that our simulation had high fidelity. The furthest north station, KGCN just south of the Grand Canyon, showed the model largely agreed with observations and reproduced all three peaks in surface wind speed. Though the simulation overpredicted the first peak by 1 m s^{-1}, the intensities of the second and third peaks were quite close to observations, though 2 hr too early and late, respectively. The simulation also predicted a moderate, independent peak at 0600 UTC, 2 August. While this is present in the observations to

some degree, it is less intense and shorter in duration, highlighting the persistence of a strong outflow from the decaying QLCS over a larger area.

At Flagstaff, KFLG, the model followed the observed wind speeds very closely until the second wind peak. It initially underpredicted wind speed by 2 m s^{-1} and then overpredicted the peak by 0.75 m s^{-1}, though the timing is nearly perfect. The major failing at KFLG was the late arrival and overprediction of the third wind peak.

At KIGM, near the Arizona-Nevada border northeast of Kingman, the model exhibited unique errors for each of the three peaks. Forecasted winds were almost twice as fast as the observations (7.5 m s^{-1} versus 14 m s^{-1}) during the first peak. The simulation timed the second peak well but underforecasted it by 5 m s^{-1} and completely missed the very narrow third peak. The failure on the third peak likely occurred due to the orientation and storm motion of the simulated QLCS, which was aligned more north–south and moved farther west than observed, causing the southern half of the line to develop west of KIGM.

Lastly, the simulation was incredibly skillful at KEED near the triple point, capturing the timing of the three wind speed peaks associated with the main body of the event within 30 min of the observations. The forecasted magnitudes of the peaks at 0600 UTC, 1 August, and 0200 UTC, 2 August, were accurate, though the model underpredicted the peak at 0200 UTC, 3 August, by 5 m s^{-1} due to the erroneous progression of the QLCS.

Our verification of forecasts over the RAWS network was quite similar to those over the ASOS network. Figure 43 shows an overprediction of peak wind speeds by 1 m s^{-1} but close agreement of the wind speed between convective periods. This resulted in an event network average bias of +0.888 m s^{-1}.

The first individual station we assessed was QGBA3, located west-northwest of Flagstaff. The simulation slightly overpredicted the magnitude of the second event peak (1.25 m s^{-1}) and greatly overforecasted the magnitude of the third peak (10 m/s), both of which arrived 5 hr late. Farther west, just south of Mount Mohon, the QGDA3 time series showed similar overprediction of both the secondary and tertiary wind speed peaks, with strong sustained wind following the third peak. The simulation did, however, skillfully capture the first observed peak for this location.

Figure 43. Similar to Fig. 42 except for the average of all RAWS stations (*A*), QGBA3 (*B*), QGDA3 (*C*), GMBA3 (*D*), and QHAA3 (*E*) surface (6.1 m) wind speed. *Dots* are used for individual stations since data is reported only once every hour with no specific reporting time.

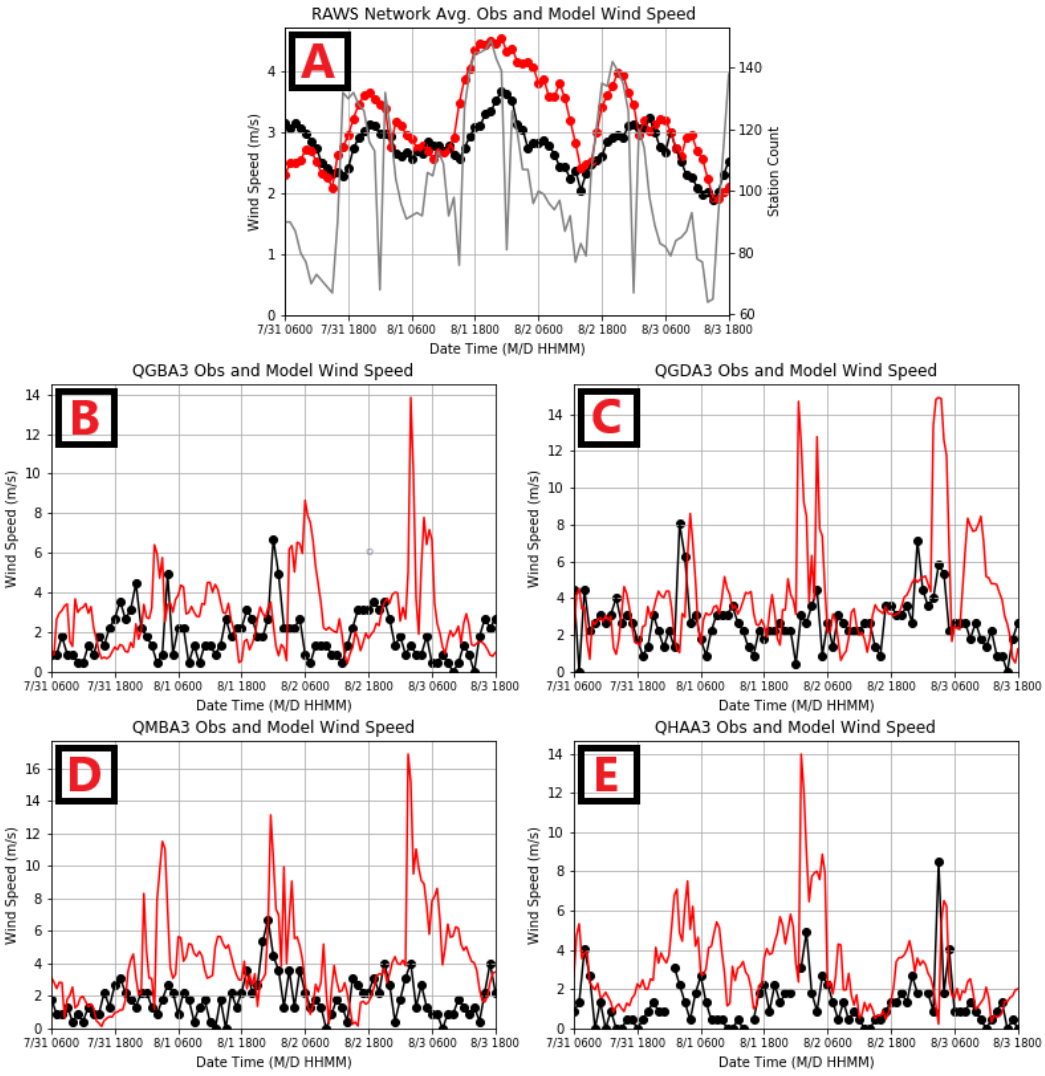

Near Hualapai Peak, QMBA3, our simulation demonstrated nearly identical overprediction of all three peaks, with lingering fast winds following the third event. The last station, QHAA3, only 9 km from KEED, provided an interesting contrast. Here, the model overpredicted the first and second peaks similar to what we saw at the other RAWS stations but underestimated the intensity of the third peak, similar to what occurred at KEED. We believe this difference between KEED and QHAA3 was due to topography. Specifically, the RAWS station site is at the bottom of a 6.5 km valley, 100 m lower than KEED, which may have inhibited strong winds from reaching the surface.

Overall, both the ASOS and RAWS results suggest that the model wind representations were skillful. The simulation adequately captured wind speeds between convective events and effectively reproduced a few of the event peaks during the most extreme part of the event, despite overprediction caused by complex topography.

3.5 30 July 2018 case study

3.5.1 30 July 2018 event overview

The last case occurred on 30 July 2018 over central Arizona, just downslope of the Mogollon Rim. The event began at 1800 UTC, 29 July, peaked around 0030 UTC, 30 July, and concluded mainly by 0500 UTC, 30 July. The synoptic setup was relatively similar to the 4 July 2014 (section 3.1) and 28 June 2015 (section 3.3) cases, with a ridge/trough pattern set up over the CONUS (Figure 44). However, the ridge-and-trough axes in this event were farther west, centered over western California and the central Mississippi River Valley, respectively. Also, the 500 hPa height pattern was much more amplified with the ridge-and-trough peaks extending well north into Canada and south into Mississippi and Alabama, respectively, prompting higher pressure over the DSWUS. These differences resulted in the center of the upper-level rotation occurring farther west than in our other cases (centered over southern Nevada), causing reduced southerly winds in the western half of Arizona and increased northerly winds over the northeast corner of Arizona. As time progressed from event initiation through the event peak, the flow pattern became even more amplified as the ridge built farther northward, and a jet streak migrated southeast between the ridge-and-trough axes.

The SPCHMA 850 hPa analysis (also seen in Figure 44) highlights the individuality of this case. In particular, the dew-point temperatures over Arizona during the preconvection period were 4°C higher in the region southwest of the Mogollon Rim than in the previous cases, indicating higher availability of atmospheric moisture for this event. The preconvection wind field showed moderate (varying between 5 and 15 kn [2.57 and 7.71 m s^{-1}] over land and sea respectively) southerly and southeasterly winds between the western half of Arizona and the Gulf of California. There was also a drastic change in predominant wind direction in the region extending from the Gulf of Mexico to southeast Arizona. This pattern effectively cut off the Gulf of Mexico as a moisture source for developing convection

and deprived storms of an easterly steering flow. Instead, the low-level winds were more westerly, actively pushing upslope against the terrain.

Figure 44. SPCHMA of 500 hPa height (*contoured*) and wind (*barbs* and *shaded*) (*panels A* and *B*) and 850 hPa height (*contoured*), wind (*barbs*), and dew point (*shaded*) (*panels C* and *D*) valid at 1200 UTC, 29 July 2018 (*A*, *C*), and 0000 UTC, 30 July 2018 (*B*, *D*).

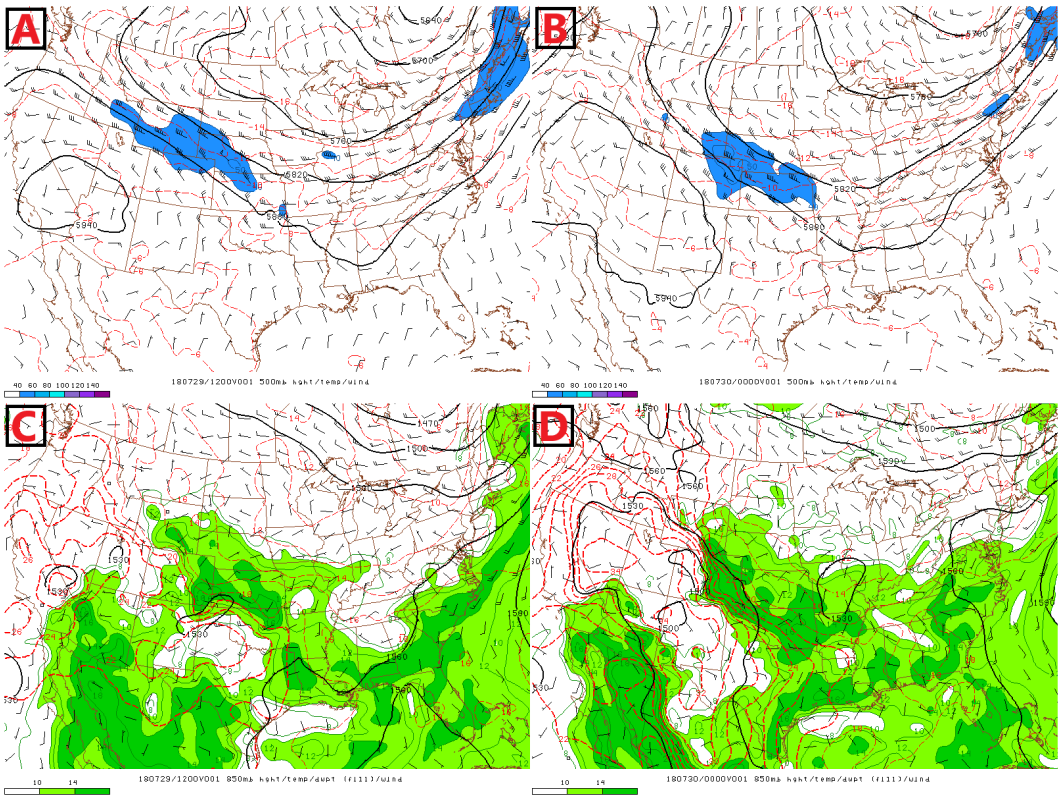

Similar to the 4 July 2014 test case, convection initialized first over the White Mountains and Chiricahua Peak at 1800 UTC, 29 July (Figure 45). The convection along the White Mountains continued to grow until 2100 UTC, at which point the initial cells along the Mogollon Rim collapsed as convection moved slowly south downslope. At this same time, new convection began to form in a line along the Mogollon Rim, and additional scattered cells developed south of Tucson, Arizona. Over the next 3 hr (2100 UTC, 29 July, to 0100 UTC, 30 July), the convective line spanning the Mogollon Rim and the White Mountain Range moved south-southwest downslope while the cells on the leading edge of the eastern portion continually collapsed and redeveloped (approximately every 1.5 hr).

Figure 45. NEXRAD radar composite imagery for the 30 July 2018 case for 1900 UTC, 29 July 2018 (*A*); 2100 UTC, 29 July 2018 (*B*); 2300 UTC, 29 July 2018 (*C*); 0030 UTC, 30 July 2018 (*D*); 0200 UTC, 30 July 2018 (*E*); and 0400 UTC, 30 July 2018 (*F*).

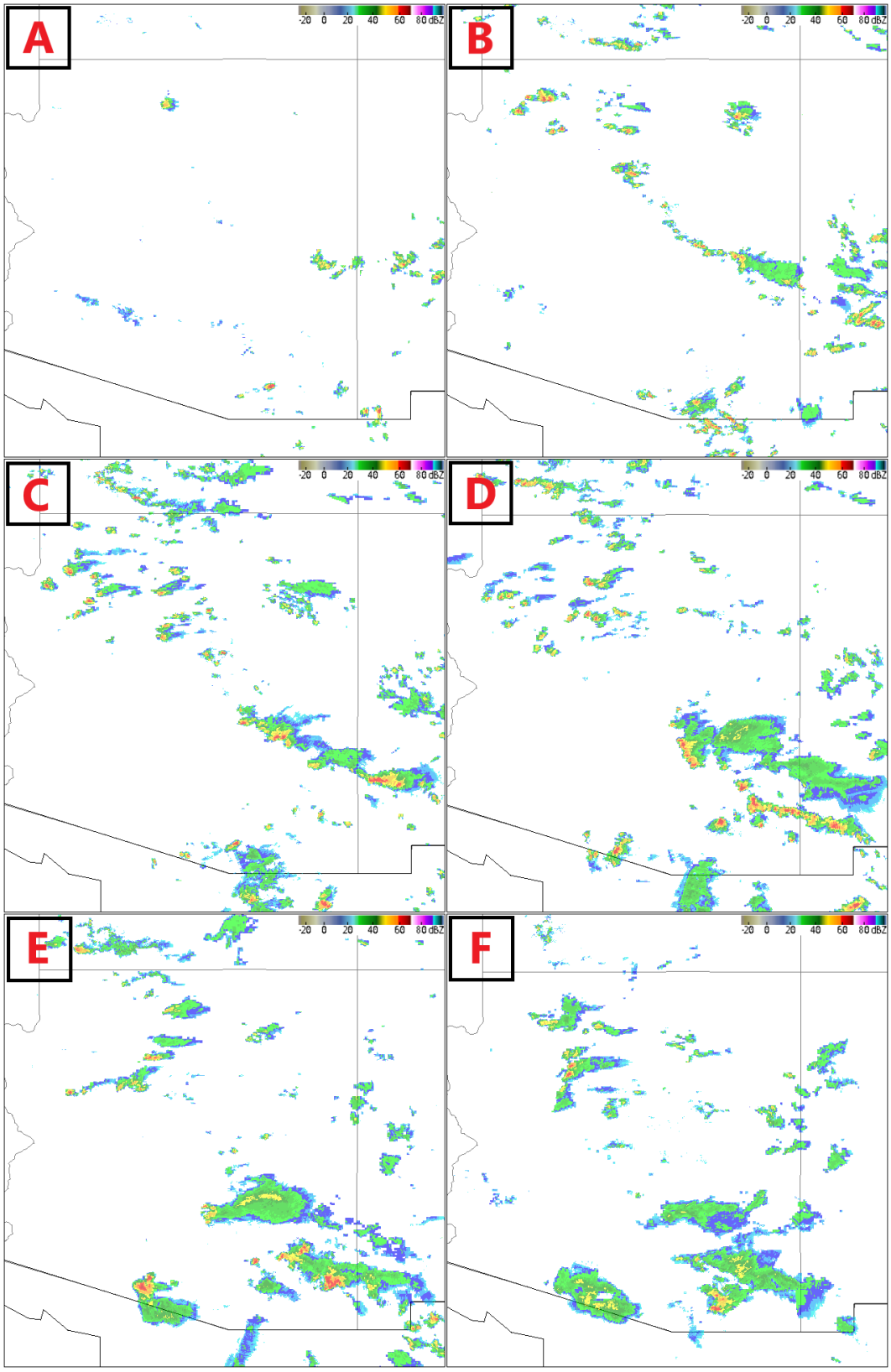

By 0100 UTC, 30 July, the line had split into two distinct, intense QLCSs. The first was a smaller, westward-moving north–south line; and the second was a longer northwest–southeast line propagating southwestward. Both lines left noticeable stationary reflectivity signals in their wake, likely indicating lofted dust. Over the next 4 hr, these lines continued to traverse in their respective directions but deteriorated rapidly, unable to maintain a coherent QLCS structure. The western line fell apart as it moved over the Phoenix area, dissipating completely by 0230 UTC, 30 July, while the southern line broke apart into smaller cellular clusters at approximately 0200 UTC, 30 July. All of the cluster remnants either disappeared or considerably weakened by 0500 UTC, 30 July, as they crossed into the isolated terrain peaks of southern Arizona. Overall, convection throughout the event was unable to maintain a coherent QLCS structure for any significant length of time and ultimately organized as a collection of independent cells.

3.5.2 30 July 2018 simulation results

Like in our other three Arizona-centered cases, our simulation forecasted the synoptic conditions for this event rather well. Figure 46 compares the SPCHMA analysis and WRF-simulated 500 hPa flow pattern at 1200 UTC, 29 July, and 0000 UTC, 30 July. Our simulation successfully captured the broad high-pressure circulation centered over Arizona's northwest corner and the southern tip of Nevada, generating east-southeasterly winds over Arizona despite the larger area covered by the high pressure in our simulation. Also, it reproduced a concentrated area of high winds, known as a jet streak, positioned over Wyoming, Colorado, Nebraska, and Kansas. This setup provided weak synoptic-scale forcing over Arizona and promoted descending vertical motion over the Oklahoma and northern Texas region.

Figure 46. SPCHMA (*panels A* and *B*) and WRF CTRL d01 forecasts (*panels C* and *D*) of 500 hPa height (*contoured*) and wind (*barbs* and *shaded*) valid at 1200 UTC, 29 July 2018 (*A*, *C*), and 0000 UTC, 30 June 2018 (*B*, *D*).

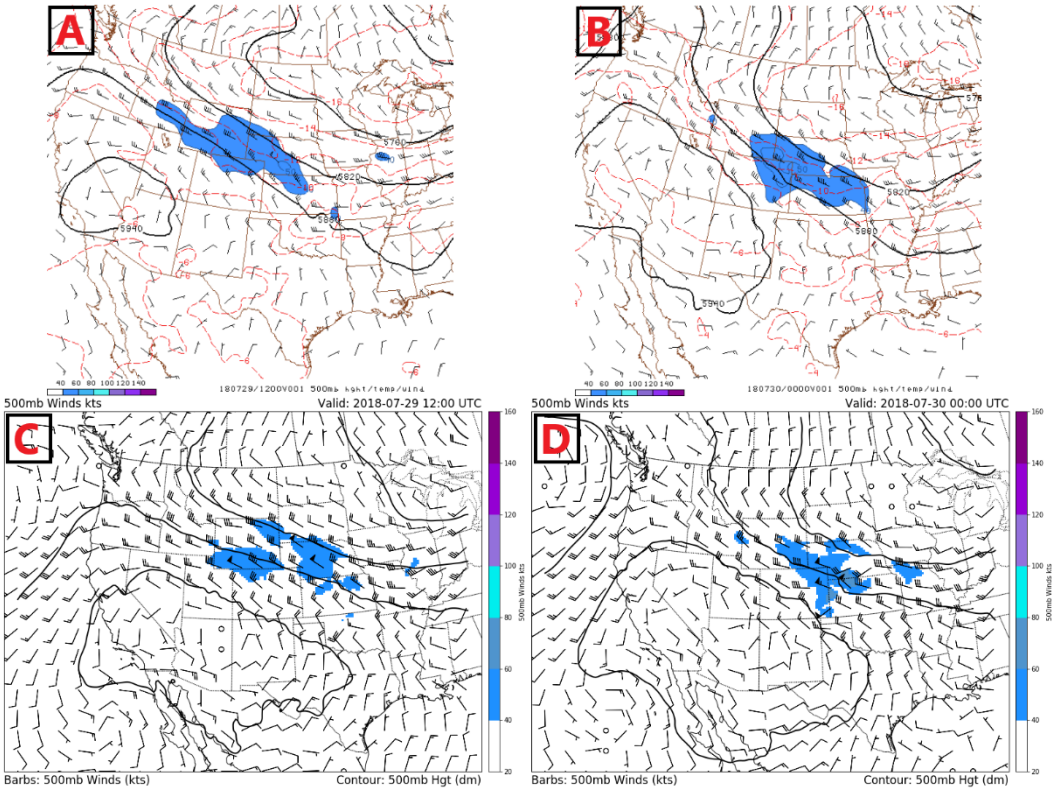

The SPCHMA analysis and WRF-forecasted 850 hPa flow-pattern comparison (Figure 47) shows that our simulation produced similar dew-point temperature patterns as the SPCHMA. Both products incorporated higher dew-point temperatures over western Mexico, southwestern Arizona, and southern California and a sharp southwest–northeast gradient cutting through Arizona. It is unknown if the abrupt dewpoint gradient in the forecast is an artifact of the high terrain cutting off the 850 hPa pressure level or if it is robustly resolved; but either way, our simulation is able to reproduce the areas of higher low-level moisture. Our WRF simulation also recreated the drier conditions over northern Texas and western Oklahoma associated with air subsidence from the upper-level high winds. This process confined the higher dew-point temperatures to southwest Texas at 1200 UTC, 29 July. During the buildup to the event, this pattern continued, allowing dew-point temperatures and moisture content to build up along the southeast Texas coast, Oklahoma, and Kansas while keeping moisture from moving into the DSWUS.

Figure 47. SPCHMA (*panels A* and *B*) and WRF CTRL d01 forecasts (*panels C* and *D*) of 850 hPa height (*contoured black*), wind (*barbs*), and dew point (*shaded*, Celsius) valid at 1200 UTC, 29 July 2018 (*A*, *C*), and 0000 UTC, 30 July 2018 (*B*, *D*).

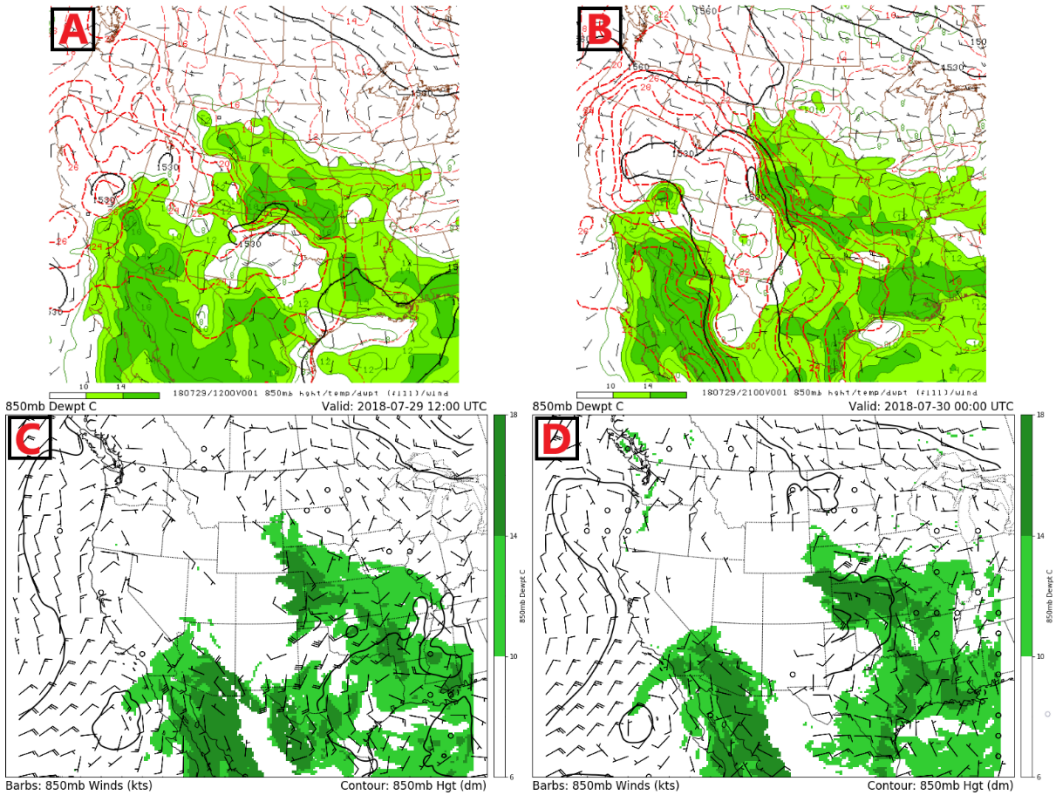

Most importantly, our simulation captured the low-level westerly winds over the southern half of Arizona, distinguishing this dust event from the other Arizona-centered cases. Over the Gulf of California, moderate southerly winds brought in moisture that became trapped in Arizona due to westerly winds running up against the high terrain, a finding supported by our 850 hPa dew-point and PWAT comparisons (Figure 48). Much like dew-point temperatures in the 850 hPa analysis, the higher PWAT values (>1.5 in.) indicate that elevated topographic features bound moisture in southwestern Arizona.

Figure 48. SPCHMA (*panels A* and *B*) and WRF CTRL d02 forecasts (*panels C* and *D*) of column-integrated precipitable water (under 400 hPa, *shaded* and *contoured* in inches) valid at 1200 UTC, 29 July 2018 (*A*, *C*), and 0000 UTC, 30 July 2018 (*B*, *D*). Contours are every 0.1 in.

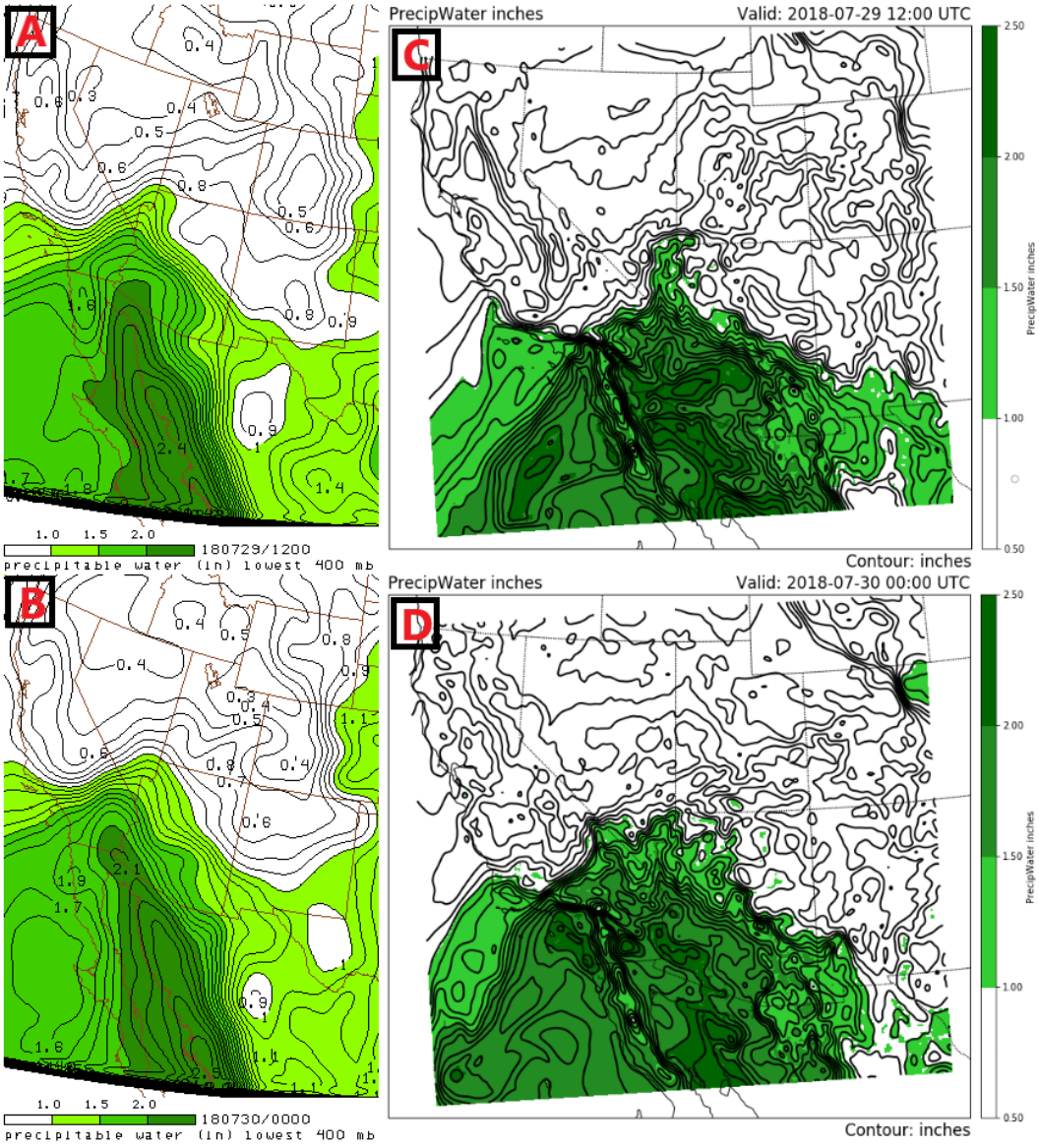

Much like the 4 July 2014 and 28 June 2015 cases, convection initiated first as cells building into a small QLCS over the White Mountains at 1800 UTC, 29 July 2018, followed shortly by isolated thunderstorms along the peaks of southern Arizona (Figure 49). Our simulation reproduced the convection origination, the shift in development to a more extensive line of cells along the Mogollon Rim, and the loose cluster of thunderstorms in southeast Arizona by 2100 UTC, 29 July. However, the observed and forecasted radar began to diverge slightly at 2300 UTC. At this time, the simulation organized the southern Arizona thunderstorms into a more coherent

north–south line with trailing precipitation. It also formed breaks in the northwest–southeast line, underpredicting the intensity of convection particularly in eastern Arizona and western New Mexico, and developed an additional cell south of the leading westward cell. The combination of these differences caused the simulation to generate a more intense north–south convective line.

The gap between the simulation and observation became increasingly apparent by the peak of the event, 0030 UTC, 30 July. Observed radar indicated a small, north–south QLCS advancing westward, a secondary northwest–southeast convective line developing along the gust front of the initial dying line, and convective activity in southern Arizona limited to a small MCS propagating westward. Our simulation captured a considerably weakened version of the small north–south QLCS approaching Phoenix, although it progressed much faster than observed. The model also reproduced the secondary west–east line of cells but positioned them farther west than observed, merging the line with the northern tip of the southern QLCS and nearly merging the line on the southern end. Furthermore, convection that manifested as an independent MCS in the observations was instead merged into a larger area of convection over southern Arizona in our simulation.

Ultimately, our simulation produced a single unified bow echo (i.e., an intense curved QLCS) with an incredibly strong and broad outflow at 0200–0400 UTC, 30 July. This feature was utterly absent from the NEXRAD observations, which only showed remnant stratiform radar reflectivity left in the wake of dying convective cells. It is not precisely clear what the driving causes of this disparity in convective development are, but it is potentially linked to cross-terrain flow and low-level shear, which are known to have a large influence on storm growth and maintenance. We attributed most of the resultant forcing-condition errors from this point on to the simulated change in the convective mode.

Figure 49. Observed NEXRAD radar (*panels A–F*) and WRF CTRL d03 simulated 1 km AGL radar (*panels a–f*) at 1900 UTC, 29 July 2018 (*A*, *a*); 2100 UTC, 29 July 2018 (*B*, *b*); 2300 UTC, 29 July 2018 (*C*, *c*); 0030 UTC, 30 July 2018 (*D*, *d*); 0200 UTC, 30 July 2018 (*E*, *e*); and 0400 UTC, 30 July 2018 (*F*, *f*).

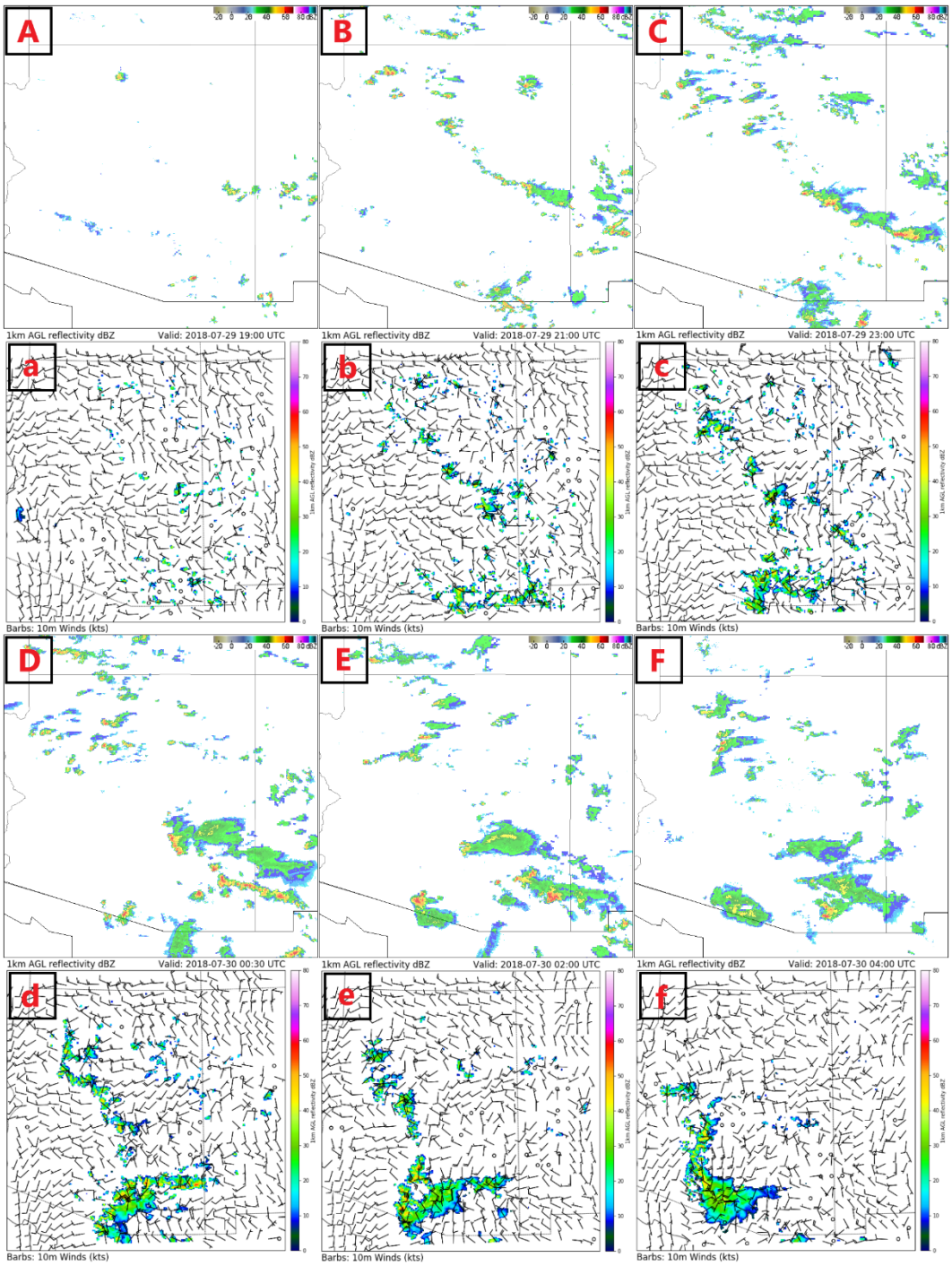

Figure 50 shows the evolution of observed and forecasted wind speeds for the ASOS network and individual stations. Up until 0200 UTC, 30 July, forecasted network average wind speeds closely followed the observations,

only occasionally underforecasting the pre-event winds. The peak winds arrived 1.5 hr late and were 1.4 m s^{-1} faster than observed because of their association with the simulated bow echo feature outflow rather than the passing of gust fronts from splitting QLCSs. Overall, this resulted in a deceptive network average bias of only –0.01 m s^{-1}; however, analysis at individual stations emphasized reasons for concern about the model's ability to predict peak winds at specific locations accurately.

Between 1500 and 2300 UTC, 29 July, the forecasted winds at KSAD just south of the White Mountains were much slower than observed by at least 2 m s^{-1} and by as much as 8 m s^{-1}. A disparity in wind direction also accompanied this period of slower winds. The model forecasted winds from the south and west-southwest when observed winds were consistently west-northwesterly to northwesterly. This small shift in wind speed and direction promoted more upslope flow from southwesterly winds, altering the direction of low-level shear vectors that convection often orients relative to. This causes the simulation to favor the development of north–south convection instead of the "along-slope" flow that confined observed convection to the northwest–southeast ridgeline.

At KTUS (Tucson, Arizona), the forecast followed the observations quite well, with a few exceptions. At 0400 UTC, the model overestimated wind speeds from a pre-event thunderstorm that, in reality, missed Tucson. Also, between 0000 and 0100 UTC, 30 July, observations for this site were missing during what may have been a potential wind speed peak. The most crucial deviation occurred between 0300 and 0700 UTC, 30 July, when the simulation overpredicted peak winds by 4 m s^{-1}. Though well-timed, errors of predicted peak winds stemmed from westerlies produced by the outflow of the erroneous bow echo system as it collapsed. In reality, southwesterly winds at this site shifted to northerly as the gust front continued moving southwest, downslope from the Mogollon Rim. The change in the origin of the peak winds was also apparent at KPHX and KDVT, closer to the reported dust event, where the simulation overforecasted winds by 3 m s^{-1} and 6 m s^{-1}, respectively. Observed wind directions during these peaks were persistently west-southwesterly or south-southwesterly ahead of the northern QLCS (not shown). However, the forecast reflected a rapid shift from west-northwesterly winds to strong southerly winds associated with the erroneous bow echo outflow.

The comparison of our simulated data against RAWS observations (Figure 51) tells a very similar story. As with our previous case studies, the simulation overpredicted the peak network average RAWS wind speed, in this case by 1.5 m s^{-1} when observed wind speeds reached their peak at 2300 UTC, 29 July, and 2.25 m s^{-1} when forecasts reached their peak wind speeds an hour later. However, the simulation captured the pre-event wind speeds fairly well (before 1500 UTC, 29 July), resulting in an average bias of +0.88 m s^{-1}. Like ASOS, the RAWS network average had a secondary peak at 0600 UTC, 30 July, associated with the forecasted bow echo system and strong gust front, neither of which were present in the observations.

Figure 50. Time series of observed (*black*) and modeled (*red*) surface (10 m) wind speed during the 30 July 2018 dust storm for network average of all ASOS stations (*A*), KSAD (*B*), KTUS (*C*), KPHX (*D*), and KDVT (*E*). The *gray line* in the network average shows the number of stations used in the network average. The 1 min observations are supplemented by METARS at individual stations when needed and are denoted by *dots*.

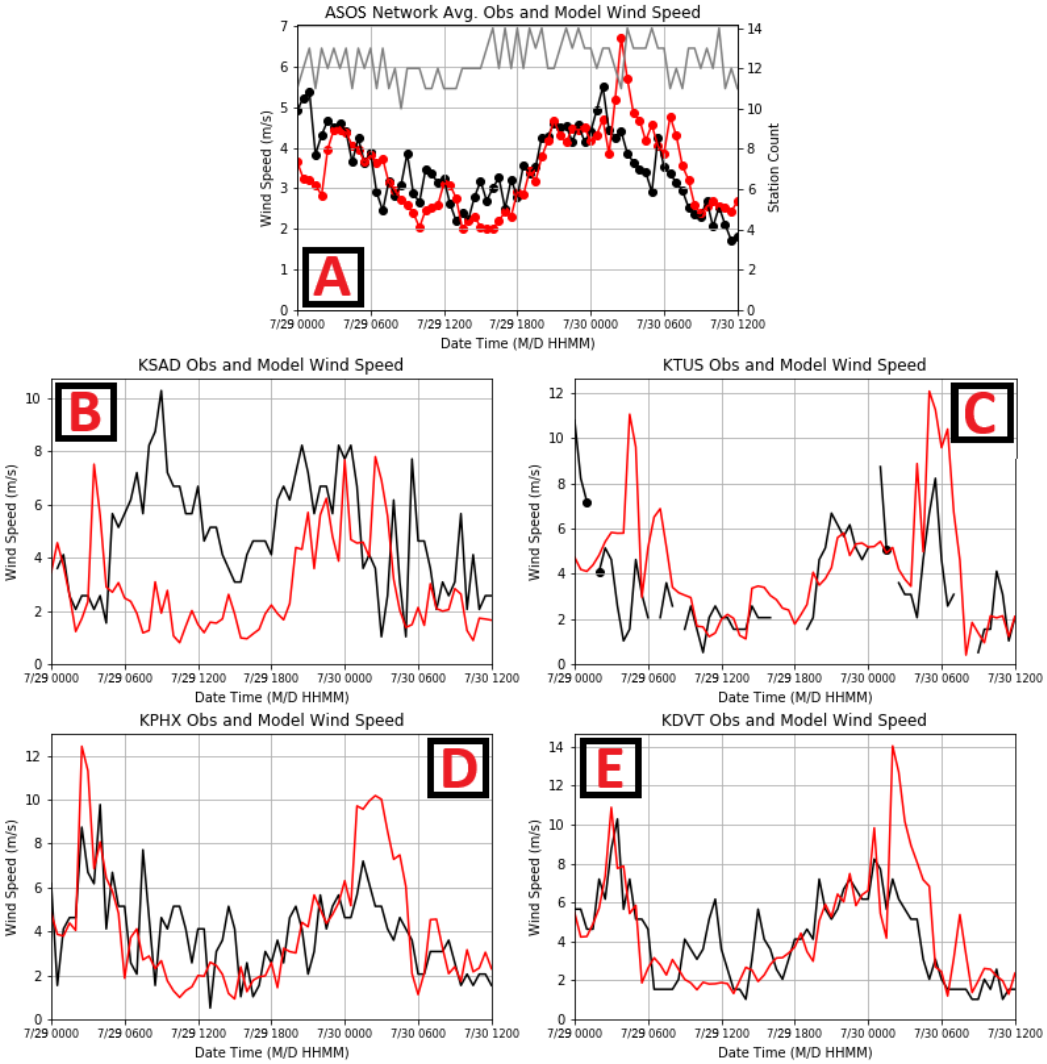

Figure 51. Similar to Fig. 50 except for the average of all RAWS stations (*A*), QHBA3 (*B*), QHRA3 (*C*), GSCA3 (*D*), and QGLA3 (*E*) surface (6.1 m) wind speed. *Dots* are used for individual stations since data is reported only once every hour with no specific reporting time.

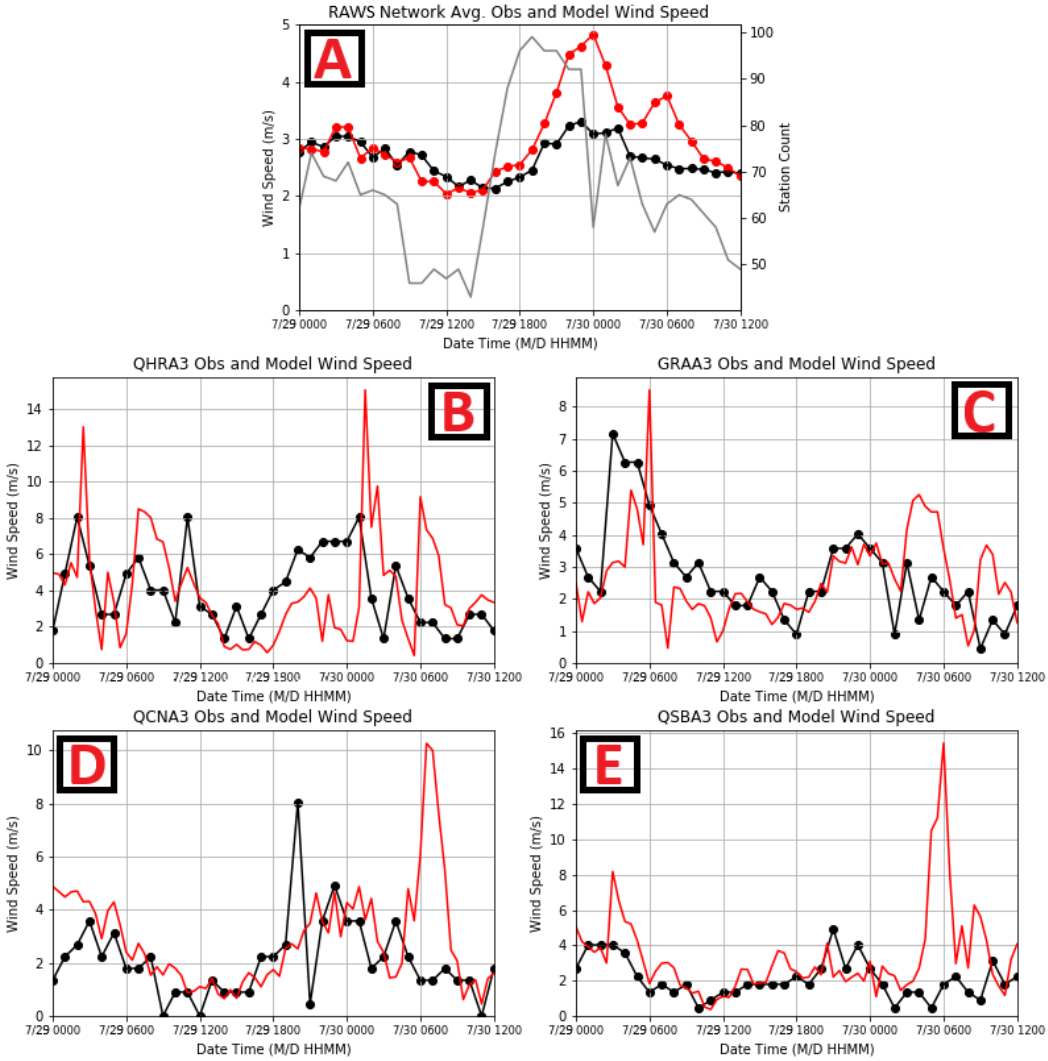

At QHRA3, on the west side of Pinnacle Ridge and 81.5 km west of KSAD, the simulation exhibited overprediction that appears to be systematic at RAWS stations for high wind speeds, most notably at the peak of the event (0100 UTC, 30 July) when forecasted wind speeds exceed observations by 7 m s^{-1}. Of note, the slower wind speeds observed 10 hr before this peak suggest that wind speeds increased more gradually in reality as the system passed. Conversely, our simulation produced a very sudden and sharp increase in wind speeds at this location.

In the southern region of Arizona, simulated winds at QCNA3 and QSBA3 (73 km southeast and 67 km southwest of Tucson, respectively) generally

reproduced observations skillfully. Both of these stations experienced faster wind speeds at 2000 UTC, 29 July, on the edges of passing isolated thunderstorms. These storms, slightly misplaced by the forecast, caused the simulation to underestimate wind speeds at these locations by 3 m s^{-1} and 1 m s^{-1}, respectively. Again, the simulation displayed extreme biases of +8 m s^{-1} at QCNA3 and +13 m s^{-1} at QSBA3, caused by the unrealistic bow echo outflow.

Closer to the actual reported dust event, southeast of Phoenix, GRAA3 exhibited a pattern very similar to KPHX, with forecasts matching observations quite well before 0100 UTC, 30 July. After this point, the simulation produced an unrealistic secondary peak in wind speed associated with the overdeveloped bow echo.

Overall, verification of ASOS and RAWS observations highlights the importance of accurate convective mode prediction, which introduced large biases in what otherwise could have been a skillful forecast.

4 Discussion

Because we designed our study around convectively driven DSWUS dust events, each of the selected events was generally void of large-scale synoptic forcing. Overall, our CTRL configuration skillfully predicted these weak synoptic forcing conditions, effectively reproducing the position and evolution of the upper level (500 hPa) flow patterns, midlatitude pressure systems, lower-level (850 hPa) flow, and atmospheric moisture sources. This outcome, however, was not entirely unexpected due to the overall lack of strong gradients, absence of rapidly changing synoptic conditions, and relatively short simulation length (except for the 1–2 August 2017 case) associated with each of our case study events.

In the few instances where synoptic conditions did not match perfectly, there were consequences for the forecasted convection. For example, in the 1–2 August 2017 case, persistent easterly upper- and lower-level winds affected the simulated convection's orientation and progression. Our 20 August 2014 simulation also suffered due to overestimated large-scale southerly winds and moisture availability, which contributed to a shift in the convection position.

This general skill in predicting background synoptic conditions translated to predominantly well-predicted convective activity in our study. Except for the 20 August 2014 case, the forecasted locations of convective initiation lined up incredibly well with observed convective development, and convection generally occurred within 1 hr of the observed timing. Our CTRL configuration accurately reproduced the convective mode for each of the events. Even in the 20 August 2014 case, where the simulation displaced convection, the model for the most part correctly distinguished between isolated cells, cellular clusters, QLCSs, and MCSs. The major exception to this was the 30 July 2018 case, when the simulated convection in the southern region of Arizona intensified much more than the observed convective cells and shifted from cellular clusters to a bow echo.

All three of the central Arizona case study simulations overdeveloped convection in the southern region of the state. This nuance, however, did not always result in simulated convective mode errors. Although not explicitly investigated for this study, we suspect this phenomenon was the result of poorly resolved complex topography in the southern region. Inadequate

terrain representation may have resulted in weaker surface drag, promoted stronger cross-peak flow, favored more moisture transport from eastern sources (when available), intensified low-level shear, and produced weaker small-scale topographically induced circulations in the simulations. Still, merely increasing the domain-grid resolution is unlikely to resolve the problem as many of the atmospheric physics modules in WRF incorporate assumptions that falter on grid-scales smaller than 1 km. Exploring additional WRF configurations with finer-scale grids and scale-aware physics modules may be necessary to resolve the issue fully.

We found that accurate prediction of convective mode translated to a well-forecasted progression of the convection. While individual convective components may have arrived early or lagged, our simulations did not experience any consistent timing biases. Our simulations predicted passage of convection over geographic landmarks and regions that differed by no more than 2 hr earlier or later than arrival of convection observed by radar. A notable exception to this was the tertiary peak of convection during the 1–2 August 2017 event, when a deviation in the large-scale wind pattern resulted in the forecasted QLCS orientation and propagation being orthogonal to observations.

Surface wind speed verification showed that well-forecasted convective mode and propagation corresponded to accurate reconstructions of surface wind evolution for both domain averages and individual locations. Our simulations were mostly in good agreement with the wind speed diurnal cycle and the buildup and peak of convective winds for both the ASOS and RAWS observations. The main exception was the 20 August 2014 case, where convection displacement resulted in completely missed or considerably delayed peaks in surface wind speed.

In general, the forecasted domain-average peak wind speeds occurred within an hour of the ASOS-observed wind speed peaks. The model most frequently overpredicted peak intensity at ASOS locations by 0.5–1 m s^{-1}, but errors at individual stations varied widely with timing errors of as large as 5 hr and peak intensity biases ranging from +5.5 m s^{-1} to +6 m s^{-1}. However, the majority of ASOS comparisons showed the timing of peaks within 2 hr and peak intensity biases between ±2 m s^{-1}.

Unlike ASOS, verification of the domain-averaged RAWS forecasts suggested our model consistently overpredicted wind speeds at RAWS locations. This overestimation tended to be highest during the peak of each event (typically between 1 and 2 m s^{-1}) and varied between 0 and 1.5 m s^{-1} outside of the convectively active periods. At individual RAWS stations, just like ASOS stations, biases varied widely but did not show the persistent overprediction seen in the average of all RAWS stations.

Previously, we noted that the majority of RAWS station sites were on steep slopes and terrain peaks in remote locations. After closer analysis, we discovered that our selected RAWS locations (chosen based on proximity to the convective event) tended to align with flatter, more open areas. We believe that substantial discrepancies between the actual and model-prescribed elevations at these sites were the culprit behind this RAWS verification paradox. Lower elevations reduced terrain blocking, promoting stronger model winds. We also noted a persistent underestimation of wind speeds at the ASOS station KSAD in the lee of the White Mountains, further suggesting that critical topographic interactions were missing in our simulations.

Issues with land-use characterization may also have affected the individual RAWS station results. Prescribed land-use categories determine each location's aerodynamic surface roughness (i.e., z_0), and areas with higher or lower elevations tend to have markedly different surface features than surrounding areas in the DSWUS. We tested this theory by manually prescribing higher surface-roughness values to locations with stations at actual elevations above 2000 m. This change had some mitigating effects on the RAWS network average bias, reducing it by 12%. Though the roughness alteration did not fully resolve the issue, our findings here and the performance improvements we saw with the alternate NoahMP LSM configuration generally support the notion that roughness characterization played a role.

Lastly, we found a tendency in our simulations for surface wind speeds directly following the event's peak to remain intense. In contrast, observed wind speeds tended to drop rapidly with the passage of convection. This effect prolonged fast winds in our simulations (typically up to 2 hr), though the results varied. This finding is particularly crucial for dust-modeling applications, especially in models like WRF-Chem that assume surface dust sources contain an infinite amount of loose, erodible material.

Our July 2014 alternate configuration tests showed little sensitivity of the resultant convective spatial pattern and mode to changes in the model configuration. Two notable exceptions to this finding were the configurations utilizing the GFS analysis as an initialization dataset and the 12hrInit configuration, which was identical to the CTRL setup but initialized 12 hr earlier. These two configurations produced forecasted atmospheric conditions that differed greatly from the CTRL and other alternative simulations. The 12hrInit and GFS configurations were especially problematic in predicting moisture availability over southern Arizona, resulting in wetter and drier conditions, respectively, and further highlighting the sensitivity of resulting convection in central Arizona to conditions in the southern half of the state.

Individual station analysis at KPHX (ASOS) and GRAA3 (RAWS) showed relative consistency in forecasted wind speeds among the different configurations, with slight variations in the event's peak intensity (spread around the CTRL simulation). The persistent overprediction of wind speed at the RAWS location between all configurations further supports our theory that unresolved topography or local sheltering factors, not model physics, were responsible for the errors.

5 Conclusions and Recommendations

5.1 General conclusions

Dust aerosols pose a potential hazard to public health, agriculture, transportation, and the warfighter on the battlefield by dangerously reducing visibility and air quality. Therefore, accurate predictions of dust emissions and transport, which depend heavily on the fidelity of the underlying atmospheric forcing conditions, are essential for decision makers in a variety of fields. Our study's overall goals were to assess the ability of the WRF model, to recreate meteorological conditions when simulating convective dust storms in the DSWUS, and to better understand underlying model errors in atmospheric conditions that could influence modeled dust lofting and transport.

We approached these goals in a three-part methodology, each addressing one or more of our objectives. We first built an inventory of potential case studies by reviewing existing literature and developing an algorithm to identify severe wind events coinciding with lofted dust. This effort resulted in the identification of 47 unique convective dust events at various geographic locations, durations, forcing conditions, and convective modes. Our second step was to construct and test a WRF CTRL configuration, based mainly on the operational HRRR model, that could reasonably reproduce the convective evolution and relevant atmospheric conditions associated with multiple dust events. Our five simulated case studies showed that our model setup configuration was able to effectively recreate the synoptic conditions, convective initiation, progression of storms, and resulting wind patterns. Given the complexities of simulating small-scale convection, we considered our model configuration capable of skillfully forecasting convectively driven dust storms despite occasional errors in timing or magnitude at individual locations.

We also performed a sensitivity analysis, leveraging a variety of initialization conditions and model physics, to assess how confident our forecasts were given singular changes to our model configuration. Comparing the ensemble of simulations, we showed that convective initiation and mode were largely insensitive to model configuration. The majority of differences were in the intensity and timing of simulated surface winds. Except for the few outliers that greatly overestimated surface wind speed, our al-

ternate configurations offered no consistent benefit or detriment to forecasts at individual locations and exhibited small increases or reductions in event-averaged MAE and bias.

This report collectively establishes the capacity for the WRF model to adequately forecast atmospheric conditions during a variety of DSWUS convective dust-storm types. It also documents the various forms and sources of atmospheric forcing error that could propagate into air quality and visibility models when simulating dust associated with these types of events. Furthermore, case studies in this report (both the ones analyzed in our assessment and dates listed in Appendix B) can serve as the basis for future DSWUS convective weather and dust-modeling efforts.

5.2 Recommendations

Our previously discussed results have produced several recommendations for future research and applications. We showed that while imperfect, our CTRL configuration had considerable skill in forecasting convectively driven dust events in the DSWUS. As such, we recommend our WRF setup as a suitable base configuration for future research involving the simulation of these kinds of convectively forced events. In particular, our CTRL configuration and case studies could serve as the basis for a WRF-Chem-focused effort on convective dust-event simulation improvements.

Alternatively, we advocate utilizing the NoahMP configuration in similar studies to reduce the overestimation of wind speeds while retaining skill. However, we do remain somewhat skeptical for the need to switch LSMs since the cause of the bias was not entirely clear. Further research is necessary to explore whether the discrepancy was due to an issue with the model itself, the static surface characterization datasets, or the observations (especially at RAWS stations).

We also suggest that future efforts incorporate more extensive sensitivity analyses on a larger sample of convective cases in the DSWUS, using our study as a template. These studies could include additional configurations utilizing variable resolutions of the innermost domain, artificially flattened or exaggerated topography, alternate surface-roughness treatments, or double-moment MP schemes (such as WRF Double-Moment 6 [Lim and Hong 2010]). We suspect that sensitivity analyses with respect to domain resolution, topography shape, and surface roughness could resolve issues

with overintensification of convection in southern Arizona and overprediction of surface winds at RAWS stations. Additionally, the inclusion of additional MP scheme variations could reveal further sensitivity of forecasts to microphysical processes.

Regarding case study identification, there are several viable DSWUS convective dust case study options listed in Appendix B that future studies could use. Future efforts could also broaden the potential convective dust-event inventory through correlation of anomalously high wind speeds and particulate matter concentrations using surface observations available within the domain. By simulating additional events, researchers can reinforce and increase confidence in our study findings and explore how our results change for events with different convective structures, intensities, and geographic locations. We also suggest expanding the list to include dust events with larger-scale (synoptic) forcing, longer durations, and other areas of interest (e.g., New Mexico, Texas, and Washington).

Lastly, this study assessed our ability to simulate small-scale and complex convectively driven dust events; but larger, more widespread synoptic dust events are also of concern. We highly suggest future studies focused on synoptic activity replicate our approach and assess the underlying meteorological conditions forcing the dust before making assessments on the performance of algorithms for dust emission and transport.

Collectively, our research has provided a wealth of potential dust-event case studies and established the general fidelity of the WRF model to sufficiently recreate the complex fine-scale convective systems and gust fronts associated with much of the dust lofting and transport in the DSWUS. Further, it identified persistent errors that can lead to downstream effects when predicting dust lofting and that future studies can target to further improve forecasting capabilities in events like these. In particular, the inconsistent timing of convective events is an essential factor to bear in mind for our future studies on modelling actual dust lofting and transport. Knowing this lets us more accurately assess forecasted dust concentrations by considering that an individual storm may pass over dust-source regions up to 2 hr earlier or later than expected and change the time window for comparisons of observations and forecasts. Additionally, persistent biases over specific land-use categories and elevations allows us to be more skeptical and convey the proper uncertainties when predicting dust concentrations from events whose dust is sourced from biomes like the chaparral shrublands.

References

Adams, D. K., and A. C. Comrie. 1997. "The North American Monsoon." *Bulletin of the American Meteorological Society* 78 (10): 2197–2213. https://doi.org/10.1175/1520-0477(1997)078<2197:TNAM>2.0.CO;2.

Al-Hemoud, A., M. Al-Sudairawi, S. Neelamanai, A. Naseeb, and W. Behbehani. 2017. "Socioeconomic Effect of Dust Storms in Kuwait." *Arabian Journal of Geosciences* 10:18. https://doi.org/10.1007/s12517-016-2816-9.

AlKheder, S., and A. AlKandari. 2020. "The Impact of Dust on Kuwait International Airport Operations: A Case Study." *International Journal of Environmental Science and Technology* 17:3467–3474. https://doi.org/10.1007/s13762-020-02710-3.

Benjamin, S. G., S. S. Weygandt, J. W. Brown, M. Hu, C. R. Alexander, T. G. Smirnova, J. B. Olson, et al. 2016. "A North American Hourly Assimilation and Model Forecast Cycle: The Rapid Refresh." *Monthly Weather Review* 144 (4): 1669–1694. https://doi.org/10.1175/MWR-D-15-0242.1.

Bothwell, P. D., J. A. Hart, and R. L. Thompson. 2002. "An Integrated Three-Dimensional Objective Analysis Scheme in Use at the Storm Prediction Center." In *Preprints, 21st Conference on Severe Local Storms*, 12–16 August, San Antonio TX, JP3.1. https://ams.confex.com/ams/SLS_WAF_NWP/techprogram/paper_47482.htm.

Cao, Y., and R. G. Fovell. 2016. "Downslope Windstorms of San Diego County. Part I: A Case Study." *Monthly Weather Review* 144 (2): 529–552. https://doi.org/10.1175/MWR-D-15-0147.1.

Cao, Y., and R. G. Fovell. 2018. "Downslope Windstorms of San Diego County. Part II: Physics Ensemble Analyses and Gust Forecasting." *Weather Forecast* 33 (2): 539–559. https://doi.org/10.1175/WAF-D-17-0177.1.

Chen, F., and J. Dudhia. 2001. "Coupling an Advanced Land Surface-Hydrology Model with the Penn State-NCAR MM5 Modeling System. Part I: Model Implementation and Sensitivity." *Monthly Weather Review* 129 (4): 569–585. https://doi.org/10.1175/1520-0493(2001)129<0569:CAALSH>2.0.CO;2.

Department of the Army. 1993. *Desert Operations*. Field Manual 90-3. Washington, DC: Headquarters, Department of the Army. https://armypubs.army.mil/epubs/DR_pubs/DR_a/pdf/web/fm90_3.pdf.

Department of the Army. 2019. *Intelligence Preparation of the Battlefield*. Army Techniques Publication (ATP) 2-01.3. Washington, DC: Headquarters, Department of the Army. https://armypubs.army.mil/epubs/DR_pubs/DR_a/pdf/web/ARN20395_ATP%202-01x3%20FINAL%20WEB.pdf.

Department of the Army. 2020. *Army Aviation*. Field Manual 3-04. 2020. Washington, DC: Headquarters, Department of the Army. https://armypubs.army.mil/epubs/DR_pubs/DR_a/pdf/web/ARN21797_FM_3-04_FINAL_WEB_wfix.pdf.

Dudhia, J., and W. Wang. 2014. *"WRF Advanced Usage and Best Practices."* Presented at the 16th WRF Annual Workshop, June 2014, Boulder, CO. http://www2.mmm.ucar.edu/wrf/users/workshops/WS2014/ppts/best_prac_wrf.pdf.

Ek, M. B., K. E. Mitchell, Y. Lin, E. Rogers, P. Grunmann, V. Koren, G. Gayno, and J. D. Tarpley. 2003. "Implementation of Noah Land Surface Model Advances in the National Centers for Environmental Prediction Operational Mesoscale Eta Model." *Journal of Geophysical Research: Atmospheres* 108 (D22): 8851. https://doi.org/10.1029/2002JD003296.

Fairall, C. W., E. F. Bradley, J. E. Hare, A. A. Grachev, and J. B. Edson. 2003. "Bulk Parameterization of Air–Sea Fluxes: Updates and Verification for the COARE Algorithm." *Journal of Climate* 16 (4): 571–591. https://doi.org/10.1175/1520-0442(2003)016<0571:BPOASF>2.0.CO;2.

Fovell, R. G., and Y. Cao. 2017. "The Santa Ana Winds of Southern California: Winds, Gusts, and the 2007 Witch Fire." *Wind and Structures* 24 (6): 529–564, https://doi.org/10.12989/was.2017.24.6.529.

Fovell, R. G., and A. Gallagher. 2018. "Winds and Gusts during the Thomas Fire." *Fire* 1 (3): 47. https://doi.org/10.3390/fire1030047.

Han, J., and H. Pan. 2011. "Revision of Convection and Vertical Diffusion Schemes in the NCEP Global Forecast System." Weather Forecasting 26 (4): 520–533. https://doi.org/10.1175/WAF-D-10-05038.1

Hong S.-Y., and J. Lim. 2006. "The WRF Single-Moment 6-Class Microphysics Scheme (WSM6)." *Journal of the Korean Meteorological Society* 42 (2):129–151.

Hong, S.-Y., Y. Noh, and J. Dudhia. 2006. "A New Vertical Diffusion Package with an Explicit Treatment of Entrainment Processes." *Monthly Weather Review* 134 (9): 2318-2341. https://doi.org/10.1175/MWR3199.1.

Huang, M., D. Tong, P. Lee, Y. Tang, I. Stajner, R. B. Pierce, J. McQueen, and J. Wang. 2015. "Toward Enhanced Capability for Detecting and Predicting Dust Events in the Western United States: The Arizona Case Study." *Atmospheric Chemistry and Physics Discussions* 15:12595–12610. https://doi.org/10.5194/acp-15-12595-2015.

Hyde P., A. Mahalov, and J. Li. 2017. "Simulating the Meteorology and PM_{10} Concentrations in Arizona Dust Storms Using the Weather Research and Forecasting Model with Chemistry (Wrf-Chem)." *Journal of the Air & Waste Management Association* 68 (3): 177–195. https://doi.org/10.1080/10962247.2017.1357662.

Janjić, Z. I. 1994. "The Step-Mountain Eta Coordinate Model: Further Developments of the Convection, Viscous Sublayer, and Turbulence Closure Schemes." *Monthly Weather Review* 122 (5): 927–945, https://doi.org/10.1175/1520-0493(1994)122<0927:TSMECM>2.0.CO;2.

Jones, S. 2014. "Simulation of Meteorological Fields for Icing Applications at the Summit of Mount Washington." MS thesis, University of Nebraska. https://digitalcommons.unl.edu/natresdiss/86/.

Lader, G. A. Raman, J. T. Davis, and K. Waters. 2016. *Blowing Dust and Dust Storms: One of Arizona's Most Underrated Weather Hazards*. Technical Memorandum NWS-WR 290. Tucson and Phoenix, AZ: NOAA National Weather Service, Weather Forecast Office. http://www.atmo.arizona.edu/images/news/Aish_Article.pdf.

Lei, H., and J. X. L. Wang. 2014. "Observed Characteristics of Dust Storm Events over the Western United States Using Meteorological, Satellite, and Air Quality Measurements." Atmospheric Chemistry and Physics 14:7847–7857. https://doi.org/10.5194/acp-14-7847-2014.

Lim, K.-S. S., and S.-Y. Hong. 2010. "Development of an Effective Double-Moment Cloud Microphysics Scheme with Prognostic Cloud Condensation Nuclei (CCN) for Weather and Climate Models." *Monthly Weather Review* 138 (5): 1587–1612. https://doi.org/10.1175/2009MWR2968.1.

Lowe, C. H. 1964. "Arizona's Natural Environment: Landscapes and Habitats." Tucson, AZ: University of Arizona Press.

Lyles, M. B. 2018. "Biological, Chemical, and Environmental Hazards of Desert Dust to Military Personnel." In *Environmental Geochemistry: Site Characterization, Data Analysis and Case Histories*, edited by B. De Vivo, H. E. Belkin, and A. Lima, 467–485. Cambridge, MA: Elsevier. https://doi.org/10.1016/B978-0-444-63763-5.00019-7.

Middleton, N. J. 2017. "Desert Dust Hazards: A Global Review." *Aeolian Research* 24: 53–63. https://doi.org/10.1016/j.aeolia.2016.12.001.

Middleton, N., P. Tozer, and B. Tozer. 2019. "Sand and Dust Storms: Underrated Natural Hazards." *Disasters* 43 (2): 390–409. https://doi.org/10.1111/disa.12320.

Nakanishi, M., and H. Niino. 2004. "An Improved Mellor–Yamada Level-3 Model with Condensation Physics: Its Design and Verification." *Boundary-Layer Meteorology* 112:1–31. https://doi.org/10.1023/B:BOUN.0000020164.04146.98.

National Weather Service. 1991. "NOAA Next Generation Radar (NEXRAD) Level 2 Base Data." National Centers for Environmental Information. Accessed 1 June 2019. https://doi.org/10.7289/V5W9574V.

National Weather Service. 2018. "MADIS: Meteorological Assimilation Data Ingest System." NCEP Central Operations. Last modified 25 July 2028. College Park, MD: NOAA National Weather Service. https://madis.ncep.noaa.gov/.

NCAR (National Center for Atmospheric Research). 2019. *WRF Version 4.1*. https://github.com/wrf-model/WRF/releases/tag/v4.1.

NCEI (National Centers for Environmental Information). n.d. "NEXRAD Data Archive, Inventory and Access." NOAA National Centers for Environmental Information. https://www.ncdc.noaa.gov/nexradinv/.

NCEI (National Centers for Environmental Information). n.d. "Weather and Climate Models." NOAA National Centers for Environmental Information. https://www.ncei.noaa.gov/products/weather-climate-models.

Nichol, A. A. 1952. *The Natural Vegetation of Arizona*. Technical Bulletin 127. Tucson, AZ: University of Arizona, Agricultural Experiment Station.

Niu, G.-Y., Z.-L. Yang, K. Mitchell, F. Chen, M. B. Ek, M. Barlage, A. Kumar, et al. 2011. "The Community Noah Land Surface Model with Multiparameterization Options (Noah-MP): 1. Model Description and Evaluation with Local-Scale Measurements." *Journal of Geophysical Research: Atmospheres* 116 (D12): D12109. https://doi.org/10.1029/2010JD015139.

Pase, C. P., and D. E. Brown. 1982. "Interior Chaparral." *Desert Plants* 4 (1–4): 95–99. http://hdl.handle.net/10150/550967.

Skamarock, W. C., J. B. Klemp, J. Dudhia, D. O. Gill, Z. Liu, J. Berner, W. Wang, et al. 2019. *A Description of the Advanced Research WRF Version 4*. NCAR Technical Notes NCAR/TN-556+ STR. http://dx.doi.org/10.5065/1dfh-6p97.

SPC (Storm Prediction Center). 2022a. *Archive National Sector (s4), SPC Hourly Mesoscale Analysis (HTML5 JavaScript Version)*. Norman, OK: NOAA National Centers for Environmental Prediction, Storm Prediction Center. https://www.spc.noaa.gov/exper/ma_archive/.

SPC (Storm Prediction Center). 2022b. "Yesterday's Storm Reports." Storm Prediction Center. Norman, OK: NOAA National Centers for Environmental Prediction, Storm Prediction Center. https://www.spc.noaa.gov/climo/reports/.

Tennekes, H. 1973. "The Logarithmic Wind Profile." *Journal of the Atmospheric Sciences* 30 (2): 234–238. https://doi.org/10.1175/1520-0469(1973)030<0234:TLWP>2.0.CO;2.

Thompson, G., P. R. Field, R. M. Rasmussen, and W. D. Hall. 2008. "Explicit Forecasts of Winter Precipitation Using an Improved Bulk Microphysics Scheme. Part II: Implementation of a New Snow Parameterization." *Monthly Weather Review* 136 (12) :5095–5115. https://doi.org/10.1175/2008MWR2387.1.

Weisman, M. L., C. Davis, W. Wang, K. W. Manning, and J. B. Klemp. 2008. "Experiences with 0–36-h Explicit Convective Forecasts with the WRF-ARW Model." *Weather and Forecasting* 23 (3): 407–437. https://doi.org/10.1175/2007WAF2007005.1.

Wieringa, J. 1980. "Representativeness of Wind Observations at Airports". *Bulletin of the American Meteorological Society* 61 (9): 962–971. https://doi.org/10.1175/1520-0477(1980)061%3C0962:ROWOAA%3E2.0.CO;2.

WMO (World Meteorological Organization). 2018. *Guide to Instruments and Methods of Observation: Volume 1—Measurement of Meteorological Variables*. 2018 ed. Geneva, Switzerland: World Meteorological Organization. https://library.wmo.int/index.php?lvl=notice_display&id=12407#.WDVYPdXyuM8.

Appendix A: SPC Storm Report Database Search Algorithm

Python Script written and run with Python v3.7

```
# Script designed to search the SPC storm report database for
# windstorm reports containing a key phrase within a given
# lat/lon box

# python libraries necessary to run the code
import re
import urllib2

# list of the years to search, the database goes back to mid
# 2002, so we start at 2003 to only get complete years

years=["03","04","05","06","07","08","09","10","11","12","13",
   "14","15","16","17","18"]

# specify which years are leap years as this alters the
# number of days in February to search
leap=["False","True","False","False","False","True","False","F
   alse","False","True","False","False","False","True","False"
   ,"False"]

# populate list of months, number of days in each month (again
# for leap years), and the days to search

months=["01","02","03","04","05","06","07","08","09","10","11"
,"12"]
maxdays=["31","28","31","30","31","30","31","31","30","31","30
","31"]
leapdays=["31","29","31","30","31","30","31","31","30","31","3
0","31"]
daynum=["01","02","03","04","05","06","07","08","09","10","11"
   ,"12","13","14","15","16","17","18","19","20","21","22","23
   ","24","25","26","27","28","29","30","31"]

# specify the type of storm report to search and the keyword,
# in this case severe wind reports with comments that mention
dust
report_type="Wind"
keysearch="DUST"
dust_tags=[]
box_tags=[]

# set the lat/lon bounds for the search
```

```
minlat=30.5
minlon=109
maxlat=37
maxlon=121

# define a function to test if a string is composed only of
numbers
def test_num(v):
   try:
      float(v)
      return True
   except ValueError:
      return False

# begin search loop through years, months, and days
for i in range(len(years)):
   for j in range(len(months)):
      if leap[i]=="True":
         for k in range(int(leapdays[j])):
            datetag=years[i]+months[j]+daynum[k]
            print("Working on ",datetag)
            # uses python to fetch the text from a web address
            response=urllib2.ur-
               lopen("https://www.spc.noaa.gov/climo/reports/"
               +datetag+ "_prt_rpts.html")
            html=response.read()
            # this process begins to remove text generated
            # from converting a html page into a text file,
            # i.e. html code
            phase1="".join(html)
            phase2=re.split("<|>|\n",phase1)
            phase3=[]
            for l in range(len(phase2)):
               phase3.append(phase2[l].strip())
            for l in range(len(phase3)):
               if ("" in phase3)==True:
                  phase3.remove("")
            phase4=[]
            for l in range(len(phase3)):
               if ("/" in phase3[l])==False and ("=" in
         phase3[l])==False:
                  phase4.append(phase3[l])
            for l in range(len(phase4)):
               if ("tr" in phase4)==True:
                  phase4.remove("tr")
            for l in range(len(phase4)):
               if ("td" in phase4)==True:
                  phase4.remove("td")
            for l in range(len(phase4)):
               if ("th" in phase4)==True:
```

```
            phase4.remove("th")
        # begin searching for the section of the storm
        # report we want, i.e. Tornado, Hail, Wind
        phase5=[]
        searchtitle=report_type+" Reports"
        record=0
        for l in range(len(phase4)):
            # turns off the search reaching the header
            # of another section
            if ("Filtered" in phase4[l])==True:
                record=0
            # turns off the search reaching the header
            # of another section
            if ("Reports" in phase4[l])==True and rec-
ord==1:
                record=0
            # turns on the search when a header contains
            # the type of storm reports desired, second
            # logic gate specifies to search the
            # unfiltered storm reports
            if (searchtitle in phase4[l])==True and ("Fil-
                tered" in phase4[l])==False:
                record=1
            if record==1:
                phase5.append(phase4[l])
            # at this point the code should have removed
        all
            # html text and limited the search text to only
            # the section desired
            # the following section removes beginning and
        end
            # parentheses leaving only alphanumerics (comma
            # delimited) to search
            track=0
            for l in range(len(phase5)):
                if track==0 and test_num(phase5[l])==True:
                    track=l
            phase5=phase5[track:]
            track=0
            for l in range(len(phase5)):
            if ("(" in phase5[l])==True and (")" in
                phase5[l])==True:
                if ")"==phase5[l][len(phase5[l])-1] and
                    "("==phase5[l][len(phase5[l])-5]:
                    track=l
            phase5=phase5[:track+1]
            phase6=",".join(phase5)
            phase7=phase6.split(")")
            print("Got phases1-7!")
            print("Working on ",len(phase7)," lines")
```

```
   # begins search of comma delimited alphanumeric
reports
   for l in range(len(phase7)):
      hold=phase7[l].split(",")
      # removes spurious spaces
      if ("" in hold)==True:
         hold.remove("")
      if len(hold)>1:
         # pull the report time
         usetime=hold[0]
      # determine if the report contains unknown
      # information "UNK"
      if ("UNK" in hold)==True:
         track=0
         # reports are formatted such that the
         # latitude is the first numeric point,
         # proceeded by the state and followed
         # by the longitude
         # lat/lon are reported without decimal
         # points to the hundredths so division
         # by 100 is necessary
         for m in range(len(hold)):
            if test_num(hold[m])==True:
               track=track+1
            if track==2:
               uselat=float(hold[m])/float(100)
               state=hold[m-1]
            if track==3:
               uselon=float(hold[m])/float(100)
      if ("UNK" in hold)==False:
         track=0
         for m in range(len(hold)):
            if test_num(hold[m])==True:
               track=track+1
            if track==3:
               uselat=float(hold[m])/float(100)
               state=hold[m-1]
            if track==4:
               uselon=float(hold[m])/float(100)
      # does the report occur within the specified
      # bounds?
   if uselat<=maxlat and uselat>=minlat and
      uselon<=maxlon and uselon>=minlon:
      print("Report in box!!!")
      # this list contains all reports of
      # the chosen type without considering
      # keyword searches
      box_tags.append(
         datetag+"_"+usetime+"_"+state+"_"+str(
         uselat)+"_"+str(uselon))
```

```
            for m in range(len(hold)):
               if (keysearch in hold[m])==True:
                  print("Keyword in report!!!")
                  # this list contains only
                  # reports of the chosen type that con-
            tain the
                  # keyword search
                  dust_tags.append(
                     datetag+"_"+usetime+"_"+state+"_"+
                     str(uselat)+"_"+str(uselon))
# the process is iterated separately for leap years as
it
# changes the number of days to search in a year
if leap[i]=="False":
   for k in range(int(maxdays[j])):
      datetag=years[i]+months[j]+daynum[k]
      print("Working on ",datetag)
      response=urllib2.urlopen(
         "https://www.spc.noaa.gov/climo/reports/"
         +datetag+ "_prt_rpts.html")
      html=response.read()
      phase1="".join(html)
      phase2=re.split("<|>|\n",phase1)
      phase3=[]
      for l in range(len(phase2)):
         phase3.append(phase2[l].strip())
      for l in range(len(phase3)):
         if ("" in phase3)==True:
            phase3.remove("")
      phase4=[]
      for l in range(len(phase3)):
         if ("/" in phase3[l])==False and ("=" in
            phase3[l])==False:
            phase4.append(phase3[l])
      for l in range(len(phase4)):
         if ("tr" in phase4)==True:
            phase4.remove("tr")
      for l in range(len(phase4)):
         if ("td" in phase4)==True:
            phase4.remove("td")
      for l in range(len(phase4)):
         if ("th" in phase4)==True:
         phase4.remove("th")
      phase5=[]
      searchtitle=report_type+" Reports"
      record=0
      for l in range(len(phase4)):
         if ("Filtered" in phase4[l])==True:
            record=0
```

```
   if ("Reports" in phase4[l])==True and rec-
      ord==1:
      record=0
   if (searchtitle in phase4[l])==True and ("Fil-
      tered" in phase4[l])==False:
      record=1
   if record==1:
      phase5.append(phase4[l])
track=0
for l in range(len(phase5)):
   if track==0 and test_num(phase5[l])==True:
      track=l
phase5=phase5[track:]
track=0
for l in range(len(phase5)):
if ("(" in phase5[l])==True and (")" in
      phase5[l])==True:
   if ")"==phase5[l][len(phase5[l])-1] and
      "("==phase5[l][len(phase5[l])-5]:
      track=l
phase5=phase5[:track+1]
phase6=",".join(phase5)
phase7=phase6.split(")")
print("Got phases1-7!")
print("Working on ",len(phase7)," lines")
for l in range(len(phase7)):
   hold=phase7[l].split(",")
   if ("" in hold)==True:
      hold.remove("")
   if len(hold)>1:
      usetime=hold[0]
   if ("UNK" in hold)==True:
      track=0
      for m in range(len(hold)):
      if test_num(hold[m])==True:
         track=track+1
      if track==2:
         uselat=float(hold[m])/float(100)
         state=hold[m-1]
      if track==3:
         uselon=float(hold[m])/float(100)
   if ("UNK" in hold)==False:
      track=0
      for m in range(len(hold)):
      if test_num(hold[m])==True:
         track=track+1
      if track==3:
         uselat=float(hold[m])/float(100)
         state=hold[m-1]
      if track==4:
```

```
            uselon=float(hold[m])/float(100)
      if uselat<=maxlat and uselat>=minlat and
         uselon<=maxlon and uselon>=minlon:
            print("Report in box!!!")
            box_tags.append(datetag+ "_" +usetime+ "_"
               +state+ "_" +str(uselat)+ "_"
               +str(uselon))
            for m in range(len(hold)):
            if (keysearch in hold[m])==True:
               print("Keyword in report!!!")
               dust_tags.append(
                  datetag+"_"+usetime+"_"+state+"_"+str(
                  uselat)+"_"+str(uselon))
```

Appendix B: Full Inventory of Case Studies

Case Study Date	Source
Simulated Case Studies (Final Five)	*(5 cases)*
4 July 2014	Hyde et al. (2017)
21 August 2014	SPC (2022b)
28 June 2015	Hyde et al. (2017)
1–2 August 2017	SPC (2022b)
30 July 2018	SPC (2022b)
Potential Case Studies Within Timeframe	*(19 cases)*
9 May 2012	Lei and Wang (2014)
26 June 2012	Lei and Wang (2014)
27 June 2012	Lei and Wang (2014)
21 July 2012	Hyde et al. (2017); Lei and Wang (2014); SPC (2022b)
23 July 2012	Lei and Wang (2014)
30 July 2012	Lei and Wang (2014)
13 August 2012	SPC (2022b)
4 September 2012	SPC (2022b)
6 September 2012	Lei and Wang (2014)
30 June 2013	Hyde et al. (2017)
2 July 2013	SPC (2022b)
15 July 2013	SPC (2022b)
27 August 2013	SPC (2022b)
8 July 2014	Hyde et al. (2017)
11 August 2015	SPC (2022b)
1 July 2016	SPC (2022b)
27 August 2017	SPC (2022b)
5 September 2017	SPC (2022b)
8 July 2018	SPC (2022b)
Potential Case Studies Outside Timeframe	*(23 cases)*
3 August 2003	Lei and Wang (2014)
30 July 2005	SPC (2022b)
12 April 2006	Lei and Wang (2014)
16 May 2006	Lei and Wang (2014)
6 June 2006	Lei and Wang (2014)
24 June 2006	SPC (2022b)
2 July 2006	SPC (2022b)
28 April 2007	Lei and Wang (2014)
17 July 2007	Lei and Wang (2014)

Case Study Date	Source
19 July 2007	SPC (2022b)
23 December 2007	Lei and Wang (2014)
7 August 2008	SPC (2022b)
25 August 2008	SPC (2022b)
3 April 2009	Lei and Wang (2014)
17 July 2009	Hyde et al. (2017); SPC (2022b)
23 August 2009	SPC (2022b)
4 October 2010	SPC (2022b)
5 July 2011	Hyde et al. (2017); Lei and Wang (2014); SPC (2022b)
7 July 2011	Lei and Wang (2014)
31 July 2011	Lei and Wang (2014)
18 August 2011	Lei and Wang (2014)
26 August 2011	Lei and Wang (2014)

Abbreviations

AGL	Above Ground Level
ASOS	Automated Surface Observation System
CONUS	Conterminous United States
CTRL	Control
CU	Cumulus
dBZ	Decibels Relative to Z
DoD	Department of Defense
DSWUS	Desert Southwest United States
GFS	Global Forecasting System
HRRR	High Resolution Rapid Refresh
LSM	Land Surface Model
MADIS	Meteorological Assimilation Data Ingest System
MAE	Mean Absolute Error
MCS	Mesoscale Convective System
METAR	Meteorological Aerodrome Report
MM5	Mesoscale Model 5
MP	Microphysics
MST	Mountain Standard Time
MYJ	Mellor-Yamada-Janjić
MYNN	Mellor-Yamada-Nakanishi-Niino
NAM	North American Model
NCEI	National Center for Environmental Information

NCEP	National Centers for Environmental Prediction
NewSAS	New Simplified Arakawa-Schubert
NEXRAD	Next Generation Weather Radar
NoahMP	Noah Multiparameterization
PBL	Planetary Boundary Layer
PSD	Particle-Size Distribution
PWAT	Precipitable Water
QLCS	Quasi-Linear Convective System
RAP	Rapid Refresh Model
RAWS	Remote Access Weather Stations
RRTMG	Rapid Radiative Transfer Model for Global Climate Models
SL	Surface Layer
SPC	Storm Prediction Center
SPCHMA	Storm Prediction Center Hourly Mesoscale Analysis
TKE	Turbulent Kinetic Energy
WMO	World Meteorological Organization
WRF	Weather Research and Forecasting
WRF-Chem	WRF with Chemistry
WSM6	WRF Single-Moment 6-Class
YSU	Yonsei University

REPORT DOCUMENTATION PAGE

Form Approved
OMB No. 0704-0188

Public reporting burden for this collection of information is estimated to average 1 hour per response, including the time for reviewing instructions, searching existing data sources, gathering and maintaining the data needed, and completing and reviewing this collection of information. Send comments regarding this burden estimate or any other aspect of this collection of information, including suggestions for reducing this burden to Department of Defense, Washington Headquarters Services, Directorate for Information Operations and Reports (0704-0188), 1215 Jefferson Davis Highway, Suite 1204, Arlington, VA 22202-4302. Respondents should be aware that notwithstanding any other provision of law, no person shall be subject to any penalty for failing to comply with a collection of information if it does not display a currently valid OMB control number. PLEASE DO NOT RETURN YOUR FORM TO THE ABOVE ADDRESS.

1. REPORT DATE (DD-MM-YYYY)	2. REPORT TYPE	3. DATES COVERED (From - To)
August 2022	Final Report	FY19–FY20

4. TITLE AND SUBTITLE
Simulating Environmental Conditions for Southwest United States Convective Dust Storms Using the Weather Research and Forecasting Model v4.1

5a. CONTRACT NUMBER

5b. GRANT NUMBER

5c. PROGRAM ELEMENT
0603734A

6. AUTHOR(S)
Alex R. Gallagher, Sandra L. LeGrand, Taylor S. Hodgdon, and Theodore W. Letcher

5d. PROJECT NUMBER
T15

5e. TASK NUMBER

5f. WORK UNIT NUMBER

7. PERFORMING ORGANIZATION NAME(S) AND ADDRESS(ES)

US Army Engineer Research and Development Center (ERDC)
Cold Regions Research and Engineering Laboratory (CRREL)
72 Lyme Road
Hanover, NH 03755-1290

US Army Engineer Research and Development Center (ERDC)
Geospatial Research Laboratory (GRL)
7701 Telegraph Road
Alexandria, VA 22315-3864

8. PERFORMING ORGANIZATION REPORT NUMBER
ERDC TR-22-11

9. SPONSORING / MONITORING AGENCY NAME(S) AND ADDRESS(ES)
Headquarters, US Army Corps of Engineers
Washington, DC 20314-1000

10. SPONSOR/MONITOR'S ACRONYM(S)
USACE

11. SPONSOR/MONITOR'S REPORT NUMBER(S)

12. DISTRIBUTION / AVAILABILITY STATEMENT
Approved for public release; distribution is unlimited.

13. SUPPLEMENTARY NOTES
Extreme Terrain Research, "Forecasting EO/IR Extinction Characteristics for Active and Passive Optical Systems"

14. ABSTRACT
Dust aerosols can pose a significant detriment to public health, transportation, and tactical operations through reductions in air quality and visibility. Thus, accurate model forecasts of dust emission and transport are essential to decision makers. While a large number of studies have advanced the understanding and predictability of dust storms, the majority of existing literature considers dust production and forcing conditions of the underlying meteorology independently of each other. Our study works towards filling this research gap by inventorying dust-event case studies forced by convective activity in the Desert Southwest United States, simulating select representative case studies using several configurations of the Weather Research and Forecasting (WRF) model, testing the sensitivity of forecasts to essential model parameters, and assessing overall forecast skill using variables essential to dust production and transport.

We found our control configuration captured the initiation, evolution, and storm structure of a variety of convective features admirably well. Peak wind speeds were well represented, but we found that simulated events arrived up to 2 hours earlier or later than observed. Our results show that convective storms are highly sensitive to initialization time and initial conditions that can preemptively dry the atmosphere and suppress the growth of convective storms.

15. SUBJECT TERMS
Air quality, Climate, Computer simulation, Dust, Dust storms, Geospatial data, Southwestern States, Weather

16. SECURITY CLASSIFICATION OF:			17. LIMITATION OF ABSTRACT	18. NUMBER OF PAGES	19a. NAME OF RESPONSIBLE PERSON
a. REPORT	b. ABSTRACT	c. THIS PAGE			19b. TELEPHONE NUMBER (include area code)
Unclassified	Unclassified	Unclassified	SAR	132	